

Asia Communications and Photonics Conference (ACP) 2012

Postdeadline Submissions

ISBN: 978-1-55752-961-9

Friday, 9 November 2012

The Garden Hotel

Guangzhou, China

Orchid**15:30-17:45****AF4A • Postdeadline Session I**

Presiders: Kin S. Chiang, *City Univ. of Hong Kong, Hong Kong*; Guang-Hua Duan, *Alcatel Lucent Bell Labs and Thales Research & Technology, France*; Stefan Andersson-Engels, *Lund Univ., Sweden*

AF4A.1 • 15:30**Third-harmonic emission in fiber continuum generation**

analogous to atomic absorption, Haohua Tu¹, Stephen Boppart^{1, 1} *Univ of Illinois at Urbana-Champaign, USA.* Observed “static” third-harmonic emission lines emerging from widely variable fiber continuum generation can be considered as a classical but nonlinear analogue of atomic absorption lines present in a continuum irradiation spectrum.

AF4A.2 • 15:45

Long period fiber gratings in 9-vinylnanthracene-containing core of photosensitive polymer optical fiber, Qiao Wang¹, Tongxin Wang², Weiwei Qiu¹, Yanhua Luo³, Qijin Zhang², Bing Zhu¹; ¹ *Department of Electronic Engineering and Information Science, Univ. of Science and Technology of China, China;* ² *Department of Polymer Science and Engineering, Univ. of Science and Technology of, Hefei, China;* ³ *School of Electrical Engineering, Univ. of New South Wales, Australia.* Long period fiber gratings (LPGs) with a period of 836 μm has been fabricated in POF with high photosensitive core containing 9-vinylnanthracene using point-by-point method. The LPGs has 51 periods inscribed totally and the -1²8 dB loss peak at 1534 nm has been observed.

AF4A.3 • 16:00

Heterogeneously integrated III-V/Si multi-wavelength laser based on a ring resonator array multiplexer, Shahram Keyvaninia^{1, 2}, Steven Verstuyft^{1, 2}, Francois Lelarge³, Guang-Hua Duan³, Sonia Messaoudene⁴, Jean Marc Fedeli⁴, Tjibbe De Vries⁵, Barry Smalbrugge⁵, Jeroen Bolk⁵, Meint Smit⁵, Dries Van Thourhout^{1, 2}, Gunther Roelkens^{1, 2}; ¹ *Photonics Research Group – Ghent Univ./imec, Belgium;* ² *Center for Nano- and Biophotonics (NB-Photonics), Belgium;* ³ *III-V lab, III-V Lab, a joint lab of 'Alcatel-Lucent Bell Labs France', 'Thales Research and Technology' and 'CEA Leti', France;* ⁴ *CEA- LETI, France;* ⁵ *Photonic integration group, Eindhoven Univ. of Technology, Netherlands.* A 4-channel multi-wavelength laser integrated on a silicon waveguide circuit is realized. Waveguide-coupled output powers of 2mW and a side mode suppression ratio of more than 45dB for all channels is realized.

AF4A.4 • 16:15**Unidirectional Emission AlGaNAs Microlasers with 3dB**

Bandwidth of 13 GHz, Yong-Zhen Huang¹, Xiao-Meng Lv¹, Heng LOng¹, Ling-xiu Zou¹, Qi-Feng Yao¹, JinLong Xiao¹, Yun Du¹; ¹ *State Key Lab on Integrated Optoelectronics, Institute of Semiconductors of CAS, China.* Unidirectional emission circular AlGaNAs microlasers connected with an output waveguide are fabricated. Small signal modulation with 3dB bandwidth of 13 GHz is realized at 290 K with an injection current of 20 mA.

AF4A.5 • 16:30**Low Cost Wide Waveguide Gap Polarization Mode**

Converter, Lingjie Wang^{1, 2}, Yanli Zhao¹, Yuanzhong Xu¹, Tianhong Zhou², Weihua Liu¹, Zheng Chen², Wen Liu¹; ¹ *HUST, Wuhan, China;* ² *Accelink, Wuhan, China.* A new type of low cost polarization mode converter on basis of the segmented waveguide taper (SWT) has been proposed, which can reduce the excess loss drastically from 5dB to less than ¹5dB.

AF4A.6 • 16:45

Theoretical Investigation on the Continuous Evolution of the Electron-Gas Dimensionality: from Bulk Materials to Quantum Dots, Xiaomin Ren^{1, 1} *State Key Laboratory of Information Photonics and Optical Communications, China.* The intrinsic energy-dispersion at each energy level of electrons in a semiconductor material is assumed and then the electron-gas dimensionality could manifest a continuous evolution from 3 to 0. This leads to a new physical picture and may impact on relevant technologies.

AF4A.7 • 17:00

Cortical Response During Motor Task in Epileptic Patients with Movement Disorders: A Multimodality fNIRS-EEG, fMRI-EEG and TMS Clinical Study, Alessandro Torricelli¹, Davide Contini¹, Matteo Caffini¹, Lucia Zucchelli¹, Rinaldo Cubeddu¹, Lorenzo Spinelli², Erika Molteni³, Anna Maria Bianchi³, Giuseppe Baselli³, Sergio Cerutti³, Elisa Visani⁴, Isabella Giloli⁴, Davide Rossi Sebastian⁴, Elena Schiaff⁴, Ferruccio Panzica⁴, Silvana Franceschetti⁴; ¹ *Physics, Politecnico di Milano, Italy;* ² *Istituto di Fotonica e Nanotecnologie, CNR, Italy;* ³ *Bioengineering, Politecnico di Milano, Italy;* ⁴ *Unità Operativa Neurofisiopatologia ed Epilettologia diagnostica, Fondazione IRCCS Istituto Neurologico Carlo Besta, Italy.* Cortical response during motor tasks was assessed by a multimodality fNIRS-EEG, fMRI-EEG and TMS clinical study on adult volunteers and epileptic patients with movement disorders.

AF4A.8 • 17:15

Resonance spatial tracking through imaging for multiplex sensing applications, Kristelle Bougot-Robin¹, Weijia Wen^{1, 1} HKUST, Hong Kong. Bioarray imaging techniques based on resonant waveguide gratings involve costly instrumentation for profile shift measurement. Alternative for robust and sensitive sensing is to integrate the profile dimension inside the chip and measure using simple pictures.

AF4A.9 • 17:30

Coherent Anti-Stokes Emission from Gold Nanorods and Its Potential for Imaging, Li Jiang¹, Iwan W. Schie², Jun Qian¹, Thomas Huser^{2, 1} Centre for Optical & Electromagnetic Research, Zhejiang Univ., China; ² NSF center for Biophotonics Science and Technology, Univ. of California, Davis, USA. Coherent anti-Stokes scattering (CAS) emitted from gold nanorods (GNRS) was studied. We proved the intensity's quadratic dependence on particle density and $\cos^2(\theta)$ dependence on beams' polarization, and the potential of CAS for nanoscale imaging.

Begonia

15:30-17:15

AF4C • Postdeadline Session II

Presiders: Ernesto Ciaramella, Scuola Superiore Sant'Anna, Italy; Lena Wosinska, Royal Inst. of Technology KTH, Sweden,

AF4C.1 • 15:30

50-GHz-spaced, 8x499-Gb/s WDM Transmission over 720-km SSMF using per-channel 4¹⁶-GBd PDM-64QAM, Wei-Ren Peng^{1, 1} KDDI R&D Labs Inc., Japan. We demonstrate the world's first single-carrier-based, 400-Gb/s-class and 50-GHz-spaced WDM system using 4¹⁶-GBd PDM-64QAM per channel. Eight channels are successfully transmitted over 720-km SSMF with hybrid Raman and EDF amplification.

AF4C.2 • 15:45

Real-time Transoceanic Transmission of 1-Tb/s Nyquist Superchannel at 2.86-b/s/Hz Spectral Efficiency, Yue-Kai Huang¹, Eduardo Mateo², Masaki Sato³, Dayou Qian¹, Fatih Yaman¹, Takanori Inoue², Yoshihisa Inada², Shaoliang Zhang¹, Yoshiaki Aono³, Tsutomu Tajima³, Takaaki Ogata², Yasuhiro Aoki^{2, 1} NEC Laboratories America, Inc., USA; ² Submarine Network Division, NEC Corporation, Japan; ³ Converged Network Division, NEC Corporation, Japan. Real-time 1-Tb/s superchannel transmission over 5,400-km using 100-GbE based subcarriers was achieved with an optical bandwidth of 350-GHz. The distance was further extended to 7,200-km by using digital Nyquist-shaped subcarriers with 1-dB margin.

AF4C.3 • 16:00

168×103 Gb/s 25-GHz-Spaced C-band Transmission over 2240 km SSMF with Improved Nonlinearity Using DFT-S OFDM-8PSK Modulation, Qi Yang^{1, 1} State Key Laboratory of Optical Comm., China. With nonlinearity improvement using DFT-S OFDM-8PSK modulation, we have successfully demonstrated a transmission of 168×103 Gb/s C-band optical PDM-OFDM signals over 2240 km SSMF with 25 GHz channel spacing.

AF4C.4 • 16:15

Experimental assessment of an OFDMA-based statistical PON with flexible bandwidth allocation and sign-labels, Iván Cano¹, Angel Peralta¹, Xavier Escayola¹, Victor Polo¹, María C. Santos¹, Josep Prat^{1, 1} Universitat Politècnica de Catalunya, Spain. A statistical OFDM-PON was experimentally tested with flexible bandwidth allocation for proper detection of ONUs with differential link loss. Sign-labels were also added to boost the system sensitivity by 3dB.

AF4C.5 • 16:30

First Demonstration of Cross Stratum Resilience for Data Center Services in OpenFlow-based Flexi-Grid Optical Networks, Hui Yang¹, Jie Zhang¹, Yongli Zhao¹, Shangguo Huang¹, Yuefeng Ji¹, Jianrui Han², Yi Lin², Yong Lee^{2, 1} Beijing Univ. of Posts and Telecomm., China; ² Huawei Technologies Co., Ltd, China. We demonstrate for the first time cross stratum resilience for data center services in OpenFlow-based Flexi-Grid optical networks. The results from a large scale trial are first verified on our testbed with 200 OpenFlow-enabled nodes.

AF4C.6 • 16:45

Shared Backup Path Protection (SBPP) in Elastic Optical Transport Networks, Gangxiang Shen¹, Yue Wei¹, Qi Yang^{2, 1} Soochow Univ., Suzhou, China; ² State Key Laboratory of Optical Communication Technologies and Networks, China. We consider the share backup path protection (SBPP) and 1+1 protection techniques for CO-OFDM-based elastic optical networks. We develop mixed integer linear programming (MILP) models to minimize required protection capacity and used link spectrum in the network.

ACP Postdeadline Sessions
Friday, 9 November
15:30-17:45

Marigold

AF4D • Postdeadline Session III

15:30-17:30

Presiders: Nelson Tansu, *Lehigh Univ., USA*; Iam-Choon Khoo; *Pennsylvania State Univ., USA*

AF4D.1 • 15:30

Thin-Film Absorbers based on Gold Nanoparticles decorated Silicon Nanowires on thin Gold film, Fugen Chen¹, Liu Yang¹, Sailing He^{1, 2}; ¹Centre for Optical and Electromagnetic Research, Zhejiang Univ., China. We proposed a thin-film absorber based on gold nanoparticles decorated silicon nanowires on thin gold film, with which broadband and enhanced absorption was experimentally demonstrated compared with others without gold nanoparticles or gold film.

AF4D.2 • 15:45

A Broadband, Omnidirectional Absorber Based on a Slot Waveguide Grating on a Metallic Substrate, Feng Zhang^{1, 2}, Liu Yang^{1, 2}, Yi Jin^{1, 2}, Sailing He^{1, 2}; ¹Centre for Optical and Electromagnetic Research, State Key Laboratory of Modern Optical Instrumentations, Zhejiang Univ., Hangzhou, China; ²Zhejiang Provincial Key Laboratory for Sensing Technologies, Zhejiang Univ., Hangzhou, China. We proposed a broadband, omnidirectional absorber based on a slot waveguide grating on a metallic substrate. Average absorption of ~90% was achieved with bandwidth of 1100 nm over a wide angle range (0 - 80°).

AF4D.3 • 16:00

Multiband electromagnetic absorbers based on a metal/dielectric multilayer stack, Wenyan Wang¹, Yanxia Cui^{1, 2}, Jun Xu³, Yinyue Lin¹, Ximin Tian¹, Yuying Hao¹, Sailing He², Nicholas X. Fang³; ¹College of Physics and Optoelectronics, Taiyuan Univ. of Technology, China; ²Centre for Optical and Electromagnetic Research, Zhejiang Univ., Hangzhou, China; ³Department of Mechanical Engineering, Massachusetts Institute of Technology, USA. Based on a planar structure comprising of a metal/dielectric multilayer stack and a thick metal substrate layer, we have obtained an omnidirectional, polarization-insensitive and multiband thin absorber in the visible regime.

AF4D.4 • 16:15

Thin film a-Si Solar Cells combining with nanodome antireflection structure and silver back reflector, Xiu Wu¹, Yumin Liu¹, Zhongyuan Yu¹, Zhihui Chen¹, Chenjie Wu¹; ¹IPOC, BUPT, China. We use FEM to analyze performance of the solar cell combining with nanodome antireflection structure and silver back reflector. Optimization is carried out and an optimal structure with short circuit current in 21.9016mA/cm² is obtained.

AF4D.5 • 16:30

Detailed Study of Different CuInSe2 Nanocrystal Shapes and Their Effect on the Photocurrent Response of Dye-Sensitized Solar Cells, Ramy Nashed^{1, 2}, Ahmed Aziz², Ahmed Shehata², Ahmed Abdel-Salam², Mona Mohamed³; ¹Renewable Energy Laboratory, American Univ. in Cairo, Egypt; ²Characterization Lab, Nanotech Egypt for Photo-Electronics, Egypt; ³National Institute of Laser Enhanced Science , Cairo Univ., Egypt. The effect of CuInSe2 (CIS) nanocrystal shape, incorporated with the electrolyte solution, was investigated. CIS nanoflowers give the best performance when both conversion efficiency and photocurrent response are taken into account.

AF4D.6 • 16:45

Investigation on the exciplex and electropolymer based on 2-(4-trifluoromethyl-2-hydroxyphenyl)benzothiazole] zinc as donor or acceptor, Jingcheng Song^{1, 2}, Wenyan Wang^{1, 2}, Yan Zhengfu^{1, 2}, Yuying Hao^{1, 2}, Yanxia Cui^{1, 2}, Ji Ting^{1, 2}; ¹College of Physics and Optoelectronics, Taiyuan Univ. of Technology, China; ²Key Lab of Advanced Transducers and Intelligent Control System, Ministry of Education, Taiyuan Univ. of Technology, China. The electropolymer or exciplex between 2-(4-trifluoromethyl-2-hydroxyphenyl)benzothiazole] zinc [Zn(4-TfmBTZ)2] and several charge transport materials is investigated. This investigation is significant for utilizing Zn(4-TfmBTZ)2 in monochromatic or white organic light-emitting diode (OLED) design.

AF4D.7 • 17:00

Quasicrystal metamaterials: a route to optical isotropy, Sergey Kruk¹, Christian Helgert^{1, 2}, Manuel Decker¹, Isabelle Staude¹, Christoph Etrich², Christoph Menzel², Carsten Rockstuhl², Chennupati Jagadish¹, Thomas Pertsch², Dragomir N. Neshev¹, Yuri Kivshar¹; ¹Australian National Univ., Canberra, Australia; ²Friedrich-Schiller-Universität Jena, Germany. We introduce a novel class of metamaterials with quasicrystalline meta-atom arrangements and study their properties in comparison with periodic and disordered metamaterials. We show that quasicrystalline metamaterials exhibit isotropic optical properties while preserving pronounced resonances.

AF4D.8 • 17:15

Gold nanoparticles embedded in flexible materials: new frontiers in Plasmonics, Roberto Caputo¹, Ugo Cataldi^{1, 2}, Alastair Cunningham², Luciano De Sio¹, Thomas Buergi², Cesare Umeton^{1, 2}; ¹Physics, Università della Calabria, Rende, Italy. ²Département de Chimie Physique, Université de Genève, Switzerland. Fabrication of samples showing plasmonic properties is fundamental for the realization of devices that can exhibit peculiar electromagnetic properties. Here we illustrate results of experiments performed on systems with Au nanoparticles embedded in flexible substrates.

Postdeadline Session I

Friday, 9 November

15:30 - 17:45

Orchid Room

Postdeadline Submissions from
Subcommittees 1, 2, and 5

Third-harmonic emission in fiber continuum generation analogous to atomic absorption

Haohua Tu, Youbo Zhao, Yuan Liu, and Stephen A. Boppart

Biophotonics Imaging Laboratory, Beckman Institute for Advanced Science and Technology,

University of Illinois at Urbana-Champaign, Urbana, IL 61801, USA

Corresponding author: htu@illinois.edu, Tel: (217) 300-6710, Fax: (217) 333-5833

Abstract: Observed “static” third-harmonic emission lines emerging from widely variable fiber continuum generation can be considered as a classical but nonlinear analogue of atomic absorption lines present in a continuum irradiation spectrum.

OCIS codes: 190.4160, 060.4370, 060.7140

1. Introduction

The continuum generation in photonic crystal fibers has surprisingly connected many areas of physics through analogies. In particular, the spectral broadening of the continuum along the fiber, according to classical kinetic gas theory, has been interpreted as the irreversible evolution of narrowband pump field toward broadband thermodynamic equilibrium [1]. It is thus rather intriguing that sharp emission lines of third-harmonic generation (THG) [2] spectrally narrower than the pump were simultaneously generated with the continuum [3]. Here we introduce a new analogy to reconcile this inconsistency, arguing that these lines behave like the “static” absorption lines of atoms excited by a preexistent continuum source (static view [3]), rather than the dynamic phase-matched bands of four-wave mixing or dispersive-wave generation known to initiate the continuum generation (dynamic view [4]). In other words, the THG is a consequence of the continuum generation, not a nonlinear wavelength conversion that initiates the continuum generation.

Both views have found experimental support, although the dynamic view is more expected from the viewpoint of phase-matched nonlinear optical processes. That is, the THG is just like fiber four-wave mixing and Cherenkov radiation, and should vary with stimulation (excitation) conditions, such as pump wavelength, pulse width, and coupling power. We intend to critically test the two in widely variable fiber continuum generation, induced by a tunable fs pump laser. The static view predicts that THG will emerge at a resonant (“static”) optical frequency $3\omega_f$ intrinsic to the fiber whenever the continuum extends across its fundamental ω_f , if the $3\omega_f-\omega_f$ pair satisfies the regular phase-matching condition dictated by the mode dispersion profiles of the fiber [3]. The dynamic view, however, asserts that the THG depends on the pump frequency ω_p and coupling power, which dynamically modifies the signal from $3\omega_p$ through Kerr effect [4] (i.e., anharmonic signal generation). It should be noted that the dynamic view cannot be reduced to the static view by simply neglecting the Kerr-effect, because $\omega_f \neq \omega_p$ (see below).

2. Experiments

In our experiments, multimode photonic crystal fibers (NKT Photonics, Denmark) are employed, with each having the same cross-sectional image (Fig. 1, inset A), but with different core sizes. A tunable Ti:sapphire laser (690-1020 nm, ~100 fs, 80 MHz) is used to pump these fibers for widely variable continuum generation. An aspheric lens enables 40-70% coupling of the laser to fiber fundamental mode, with variable coupling power by varying the incident laser power. The fiber output is collimated by an off-axis parabolic aluminum mirror, and then refocused by another similar mirror onto the entrance fiber of an ultraviolet spectrometer (spectral window: 250-385 nm, resolution: 0.07 nm) to detect the THG, or that of a near-infrared (NIR) optical spectrum analyzer (set spectral window: 750-1155 nm) to locate its fundamental in the continuum.

3. Results and Discussions

Simultaneously observed fiber output spectra in the two windows at a variety of conditions (fiber type/length, pump wavelength, and coupling power) are compared in Fig. 1a-g. At low coupling power with minimum continuum generation, a THG line of 302.6 nm is generated in the fiber NL-2.0-735 when the pump is tuned to its fundamental of 302.6×3 nm (Fig. 1c). However, if the pump is detuned to 975 nm, no corresponding THG emission of 325 nm is observed. Rather, another line of 302.6 nm emerges when the blue-edge of the continuum (dispersive wave) extends across 302.6×3 nm (Fig. 1b), with a threshold-like dependence of emission intensity on the coupling power. The line stays at 302.6 ± 0.1 nm at higher coupling powers when the continuum extends beyond 302.6×3 nm (not shown). Similarly, if the pump is detuned to 805 nm, a third line of 302.6 nm emerges when the red-edge of the continuum (soliton) extends across 302.6×3 nm (Fig. 1a), with similar threshold behavior and wavelength stability. The three lines reveal nearly identical symmetric spectra (Fig. 1, inset B), indicating the THG nature of the 302.6 nm lines in

the two continuum cases, even though the signal $3\omega_f$ can be generated far away from $3\omega_p$ with a large anharmonic blue-shift Ω (green arrow, Fig. 1b).

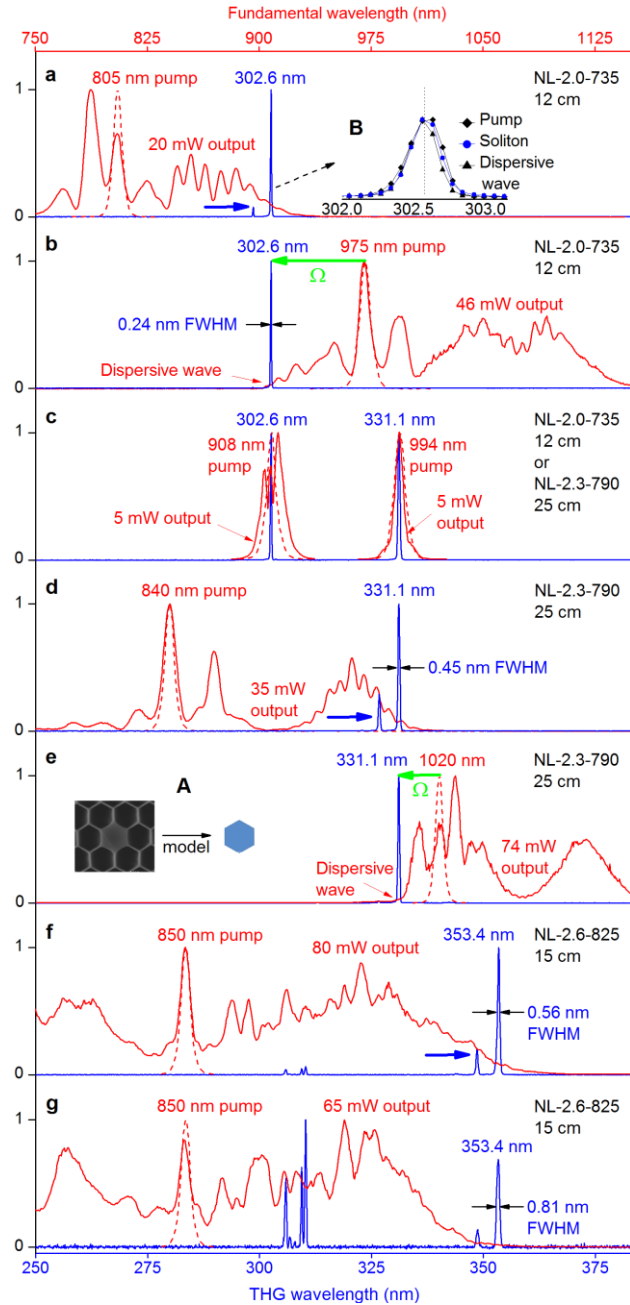


Fig. 1. Comparison of simultaneously observed fiber output spectra in the ultraviolet window (blue curves, bottom scale) and the NIR window (red curves, top scale) at various conditions of pump spectrum (broken red curves, top scale), fiber type/length, and coupling power. Inset A: common cross-sectional image of the fibers and simplified fiber cross-section for modeling. Inset B: comparison of THG spectra stimulated by pump itself, soliton, and dispersive wave for fiber NL-2.0-735.

The dynamic view of this convergence would require a delicate combination of the pump wavelength and power (Kerr-effect) to target the 302.6 nm [4-6], which is in contradiction with the observed wavelength stability against the coupling power. In contrast, the static view of this phenomenon simply attributes the emergence of the 302.6 nm ($3\omega_f$) THG lines to the presence of their fundamentals 302.6 \times 3 nm (ω_f) in the continuum, regardless of the pump wavelength and coupling power. We have confirmed the $3\omega_f-\omega_f$ coincidence (static view) in a wide range of

continuum generation. Note that this conclusion is also valid for the 331.1 nm and 353.4 nm THG lines that dominate the ultraviolet spectra of the fibers NL-2.3-790 and NL-2.6-825, respectively (Fig. 1d-1g), and for the weak THG lines (blue arrows, Fig. 1a, 1d, 1f) that accompany the dominant THG lines. Thus, the anharmonic signal is an illusion of the continuum generation, and is indeed harmonic if the fundamental is accurately located. Without the widely variable continuum generation, the prior study supporting the static view [3] was unable to accurately locate the fundamental within the generated continuum, and to shift the dynamic view toward the static one.

The dynamic view of the observed anharmonic blue-shifts (green arrows, Fig. 1b, 1e) necessitates a large Kerr-effect (coupling power effect) on the signal wavelength [4-6]. This is tested for the 331.1 nm line under direct pump stimulation (Fig. 1c), where the strongest THG is observed, and therefore the largest Kerr-effect is expected. At low coupling powers, the intensity of this line follows an expected third-order dependence on the coupling power. At the highest coupling power, which is limited by fiber optical damage, this line attains an average power of 0.15 mW, or a THG conversion efficiency of 0.2%. In a dynamic range of signal intensity over 3 orders of magnitude, the central wavelength and symmetric spectrum of the signal remain “static”. No indication of the Kerr-effect is found, even though the pump undergoes dramatic continuum transformation.

The observed signal spectrum is not only independent of the pump wavelength and coupling power, but also independent of pump polarization, indicating little influence from fiber birefringence. This complete deprival of pump dependence is the hallmark of the static view. The static view of THG can be further appreciated by the use of a simple analogy. The emergence of sharp fiber THG lines from the excitation ultrafast continuum (Fig. 1a-g, except Fig. 1c) is analogous to that of atomic absorption lines from a thermal irradiation continuum, in the sense that the line positions are independent of the spectral shapes of the incident continua. The emission (positive) signal of the former is a resonant response of the fiber to a narrowband component of the ultrafast continuum, just like the absorption (negative) signal of the latter is a resonant response of the atoms to that of the thermal irradiation continuum (Table 1).

Table 1. Continuum-excited fiber THG and atomic absorption.

Analogue	Fiber THG	Atomic absorption
Stationary state	fiber mode field	atomic wave function
Discrete variable	β - propagation constant for moment state	ν - frequency for energy state
Conjugate variable	L - fiber length	T - time
Resonance	phase-matching: $\Delta\beta = \beta(3\omega_1) - \beta(\omega_1) = 0$	Bohr condition: $\Delta\nu = \nu_2 - \nu_1 - \nu_{\text{photon}} = 0$
Nature of spectral line signal	positive, classical, nonlinear	negative, quantum mechanical, linear
Background	ultrafast continuum	thermal irradiation continuum
Transition probability	\propto mode overlap, $\propto L^2 \text{sinc}^2(\Delta kL/2)$ [4]	\propto transition dipole, $\propto T^2 \text{sinc}^2(\Delta\nu T/2)$

4. Conclusions

The demonstrated analogy warrants the classification of all phase-matched processes in fiber into two groups, depending on whether their phase-matching conditions are “dynamic” or “static” against external stimulation conditions. One group, represented by four-wave mixing, Cherenkov radiation, and stimulated Raman (or Brillouin) scattering, has a dynamic phase-matching condition, and therefore can initiate fiber continuum generation. The other group, represented by THG and second-harmonic generation, has a static phase-matching condition intrinsic to the fiber, much like the static resonant condition of atomic absorption intrinsic to the atoms (i.e., the analogy). Thus, this process cannot initiate fiber continuum generation, and can therefore be only stimulated as a result of it. The prevalent theory of fiber THG [4] does not differentiate these two groups, so that a complicated (but unnecessary) framework of “new physics” was developed to explain the observed anharmonic signal generation (Fig. 1) [5, 6].

5. References

- [1] Benoît Barviau, Bertrand Kibler, Alexandre Kudlinski, Arnaud Mussot, Guy Millot, and Antonio Picozzi, "Experimental signature of optical wave thermalization through supercontinuum generation in photonic crystal fiber," Opt. Express 17, 7392-7406 (2009).
- [2] J. M. Gabriagues, "Third-harmonic and three-wave sum-frequency light generation in an elliptical-core optical fiber," Opt. Lett. 8, 183 (1983).
- [3] L. Tartara, I. Cristiani, V. Degiorgio, F. Carbone, D. Faccio, M. Romagnoli, and W. Belardi, "Phase-matched nonlinear interactions in a holey fiber induced by infrared super-continuum generation," Opt. Commun. 215, 191-197 (2003).
- [4] G. P. Agrawal, Nonlinear Fiber Optics (Academic Press, 2007), Ch. 12, Ch. 10.
- [5] A. M. Zheltikov, "Third-harmonic generation with no signal at 3ω ," Phys. Rev. A 72, 043812 (2005).
- [6] E. E. Serebryannikov, A. B. Fedotov, A. M. Zheltikov, A. A. Ivanov, M. V. Alfimov, V. I. Beloglazov, N. B. Skibina, D. V. Skryabin, A. V. Yulin, and J. C. Knight, "Third-harmonic generation by Raman-shifted solitons in a photonic-crystal fiber," J. Opt. Soc. Am. B 23, 1975 (2006).

Long period fiber gratings in 9-vinylnanthracene-containing core of photosensitive polymer optical fiber

Qiao Wang¹, Tongxin Wang², Weiwei Qiu¹, Yanhua Luo³, Qijin Zhang², Bing Zhu^{1,*}

¹Department of Electronic Engineering and Information Science,

University of Science and Technology of China, Hefei, Anhui 230026, China

²CAS Key Laboratory of Soft Matter Chemistry, Department of Polymer Science and Engineering,

University of Science and Technology of China, Hefei, Anhui 230026, China

³School of Electrical Engineering, University of New South Wales, Sydney 2052, New South Wales, Australia

**zbing@ustc.edu.cn; phone +86 551-3601319-808; fax +86 551-3601319-803*

Abstract: Long period fiber gratings (LPGs) with a period of 836 μm has been fabricated in POF with high photosensitive core containing 9-vinylnanthracene using point-by-point method. The LPGs has 51 periods inscribed totally and the -12.8 dB loss peak at 1534 nm has been observed.

OCIS codes: 050.2770, 060.2370

Recently polymer optical fiber gratings become quite attractive in communication and sensing systems [1] since the first POF Bragg fiber grating made in 1999 [2]. POF has many advantages over its silica counterpart, such as its flexibility, biocompatibility et al. As POF has larger thermo-optic, thermal expansion, and electro-optic coefficients than silica fiber POF grating are more sensitive to many physical parameters. It has been reported that the temperature sensitivity of Bragg fiber gratings written in POF can reach 10 times larger than that of silica fiber [3]. Also FBGs written in POF are more sensitive than FBGs in silica fiber [4]. Besides of POF Bragg gratings, POF long period gratings have attracted much interest as well. Zhang Qijin et al have fabricated birefringent LPGs both in azobenzene-doped polymer optical fibers [5] and in azobenzene-containing copolymer optical fibers [6]. They have also fabricated a LPG with a -3 dB resonant peak in poly(methyl methacrylate-co-methyl vinyl ketone-co-benzyl methacrylate)-core POF by use of a mercury lamp [7]. In 2009 D. Saez-Rodriguez et al. have reported LPGs photoinscribed in microstructured POF by UV radiation and investigated the response of the LPG to the refractive index of the surrounding medium [8]. In our work, the photosensitive POF has been fabricated with 9-VA as the photosensitive species in the fiber core. Then the LPGs with a period of 836 μm has been fabricated in this kind photosensitive POF.

The POF preform was prepared with Teflon technique [9]. The POF core consists of MMA-co-BA-co-9-VA and the cladding consists of MMA-co-BA. The refractive index of POF core was measured to be 1.4810 (1550 nm) and the index difference between the core and cladding was measured by 0.003. Due to the photo-crosslinking in the 9-VA-containing core, the POF core is sensitive to the 340-400 nm UV light. In the meanwhile, the POF cladding shows insensitivity at the same wavelength range. Two films which have the same composites to the POF core and the POF cladding respectively are also fabricated. The refractive index change of the core film can reach 8×10^{-4} (1550 nm) under 365 nm irradiation after 10 min, whereas the cladding film shows no refractive index change at the same irradiation condition. Then the preform was drawn into POF. The prepared POF has a 195 μm POF diameter and 11 μm core diameter.

To design the LPG with a resonant peak near 1550 nm, a period of 836 um has been chosen according to the resonant condition for LPG coupling written as [10]

$$\lambda_{res} = (n_{co}^{eff} - n_{cl,m}^{eff})\Lambda \quad (1)$$

Where n_{co}^{eff} and $n_{cl,m}^{eff}$ are the effective indices of the fundamental core mode and the m th cladding mode respectively. Λ is the LPGs period and λ_{res} is the resonant wavelength. We introduce the parameters of the photosensitive POF mentioned above and the refractive index change of 8×10^{-4} measured in the film into the simulation of LPG with a rectangular index modulation. To obtain a maximum peak loss near 1550 nm, 31 points have been chosen for the simulation. The transmission spectrum of LPGs is simulated according to the coupled-mode theory [11] as showed in Fig. 1. The simulated spectrum shows two main resonant peaks at 1504 nm and 1552 nm respectively. These two resonant peaks are produced by the coupling of fundamental core mode and 3th (5th) cladding mode of LPGs.

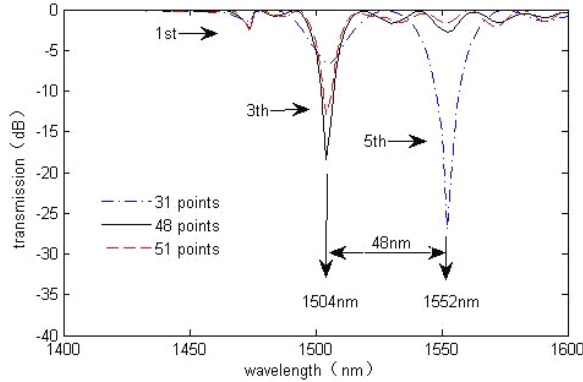


Figure 1. The simulation curve of LPG(period:836 um;31 points inscribed)

The experimental setup for fabricating LPGs using an point-by-point technique [12] was showed in Fig. 2. The UV beam from a pulsed 355 nm laser (CNI MPL-355 nm) with 10 mW output power was incident on a mirror (Zolix OML25.4-355-6.35) and then went through a slit which is 420 μm wide. A quartz biconvex lens with 40 mm focal length followed to make an image of the slit. By adjusting the distance between the slit and the lens, an image with the same size to its object could be obtained. The mirror, slit, and lens were all mounted on a translation stage (Zolix KSA050-13-X) which has 2.5 μm resolution. The translation stage stayed at each point for 2 min and then traveled 836 μm within 0.5 seconds. A pattern for a total length of 43 mm was achieved. Fig. 3 showed the LPG we fabricated under microscope. The region irradiated by UV beam became dark due to no fluorescence.

To monitor grating growth, the light from an ASE source (Amonics ASE-CL-20-B) with an operating wavelength range of 1528-1608 nm was coupled to POF through a SMF patchcord. The optical spectrum was measured by OSA (YOKOGAWA AQ6370C) with 0.5 nm resolution which was connected to the end of POF by a multimode optical fiber.

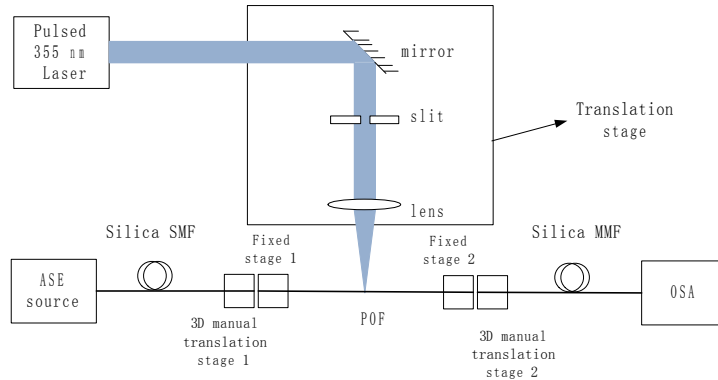


Fig. 2. Schematic of POFs writing system by point-by-point technique

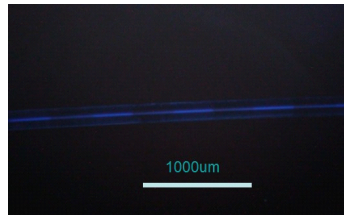


Fig. 3. Photograph of produced long period grating in POF under fluorescence microscope

In the writing process, two transmission loss peaks at about 1534 nm and 1582 nm increase gradually as showed in Fig. 4. The transmission loss of the peak (1534 nm) reaches -12.8 dB when 48 points have been written. Afterwards the loss peak decreases and it recovers to -8.2 dB when 51 points have been written. The recovery is due to over couple between the core mode and the corresponding cladding mode. The peak wavelength is varying during the writing process which should stay the same according to the coupled-mode theory is probably due to the temperature change.

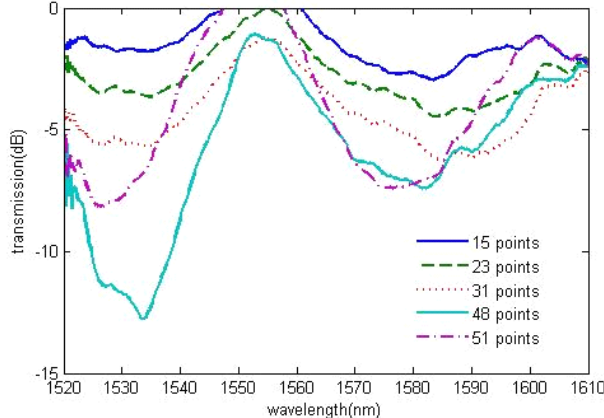


Fig. 4. Transmission spectra of the POF (a period of 836 um) at different points

To compare the experimentally obtained transmission spectra showed as Fig. 4 and the simulated spectrum showed as Fig. 3, it can be found that the two resonant peaks intervals of experimental spectrum (48 points) and simulation spectrum are the same ~48 nm. Both the loss of the 3th peak of experimental spectrum and that of simulation spectrum decrease when 51 points have been written. The difference between the experimentally obtained resonant peaks and the simulated resonant peaks is mainly owing to measurement precision of the core and cladding refractive indices. And the difference of peak loss is contributed to the difference between the refractive index change in polymer film and in POF.

In conclusion, the 836 um LPGs with high photosensitive core containing 9-VA have been successfully fabricated. Two main resonant peaks are observed and a -12.8 dB peak loss at 1534 nm has been achieved. The simulation of the transmission spectrum agrees well with the experimentally observed data. The LPGs in POF may have a great potential in various sensing devices.

References

- [1] H. Dobb, K. Carroll, D. Webb, K. Kalli, M. Komodromos, C. Themistos, G. Peng, A. Argyros, M. Large, and M. van Eijkelenborg, "Grating based devices in polymer optical fibre," in 2006), 618901.
- [2] G. Peng, Z. Xiong, and P. Chu, "Photosensitivity and gratings in dye-doped polymer optical fibers," Optical Fiber Technology 5, 242-251 (1999).
- [3] H. Liu, H. Liu, G. Peng, and P. Chu, "Strain and temperature sensor using a combination of polymer and silica fibre Bragg gratings," Optics Communications 219, 139-142 (2003).
- [4] H. Liu, H. Liu, and G. Peng, "Different types of polymer fiber Bragg gratings (FBGs) and their strain/thermal properties," Optical Memory and Neural Networks Information Optics 12, 147 (2003).
- [5] X. Xingsheng, M. Hai, and Z. Qijin, "Properties of polarized laser-induced birefringent gratings in azobenzene-doped poly (methyl methacrylate) optical fibers," Optics Communications 204, 137-143 (2002).
- [6] Y. Luo, Z. Li, R. Zheng, R. Chen, Q. Yan, Q. Zhang, G. Peng, G. Zou, H. Ming, and B. Zhu, "Birefringent azopolymer long period fiber gratings induced by 532 nm polarized laser," Optics Communications 282, 2348-2353 (2009).
- [7] Z. Li, H. Tam, L. Xu, and Q. Zhang, "Fabrication of long-period gratings in poly (methyl methacrylate-co-methyl vinyl ketone-co-benzyl methacrylate)-core polymer optical fiber by use of a mercury lamp," Optics letters 30, 1117-1119 (2005).
- [8] D. Sáez-Rodríguez, J. L. C. Munoz, I. Johnson, D. J. Webb, M. C. J. Large, and A. Argyros, "Long period fibre gratings photoinscribed in a microstructured polymer optical fibre by UV radiation," in 2009), 73570L.
- [9] G. D. Peng, P. Chu, Z. Xiong, T. W. Whitbread, and R. P. Chaplin, "Dye-doped step-index polymer optical fiber for broadband optical amplification," Lightwave Technology, Journal of 14, 2215-2223 (1996).
- [10] T. W. MacDougall, S. Pilevar, C. W. Haggans, and M. A. Jackson, "Generalized expression for the growth of long period gratings," Photonics Technology Letters, IEEE 10, 1449-1451 (1998).
- [11] T. Erdogan, "Cladding-mode resonances in short-and long-period fiber grating filters," JOSA A 14, 1760-1773 (1997).
- [12] S. Vasilev and O. Medvedkov, "Long-period refractive index fiber gratings: properties, applications, and fabrication techniques," in 2000), 212-223.

Heterogeneously integrated III-V/Si multi-wavelength laser based on a ring resonator array multiplexer

S. Keyvaninia^(1,2), S. Verstuyft^(1,2), F. Lelarge⁽³⁾, G.-H. Duan⁽³⁾, S. Messaoudene⁽⁴⁾, J.M. Fedeli⁽⁴⁾, T. De Vries⁽⁵⁾, B. Smalbrugge⁽⁵⁾, J. Bolk⁽⁵⁾, M. Smit⁽⁵⁾, D. Van Thourhout^(1,2), G. Roelkens^(1,2,5)

(1) Photonics Research Group – Ghent University/imec, Sint-Pietersnieuwstraat 41, B-9000 Ghent, Belgium

(2) Center for Nano- and Biophotonics (NB-Photonics), Ghent, Belgium

(3) III-V lab, III-V Lab, a joint lab of 'Alcatel-Lucent Bell Labs France', 'Thales Research and Technology' and 'CEA Leti', Campus Polytechnique, 1, Avenue A. Fresnel, 91767 Palaiseau cedex, France

(4) CEA- LETI, Minatec 17 Rue des Martyrs Grenoble France

(5) Photonic integration group, Eindhoven University of Technology, Den Dolech 2, Eindhoven, The Netherlands

Author e-mail address: shahram.keyvaninia@intec.ugent.be

Abstract: A 4-channel multi-wavelength laser integrated on a silicon waveguide circuit is realized. Waveguide-coupled output powers of 2mW and a side mode suppression ratio of more than 45dB for all channels is realized.

OCIS codes: (250.0250) Integrated optics; (250.5300) Photonic integrated circuits; (250.5960) Semiconductor lasers.

1. Introduction

Silicon-On-Insulator (SOI) waveguide circuits are widely studied because of the large refractive index contrast that is available on this platform, which allows realizing ultra-compact devices. The interest in this technology stems also from the expectation that the maturity and low-cost of CMOS-technology can be applied for advanced photonic products [1]. Since silicon lacks efficient light emission and amplification, the integration of III-V semiconductors on top of silicon waveguide circuits is required to achieve complex integrated circuits. Several approaches can be followed to realize this integration. Heterogeneous integration through die-to-wafer bonding and direct hetero-epitaxy allow for dense and wafer-scale integration of the III-V opto-electronic components on the silicon photonic platform. Since the quality of hetero-epitaxially grown layers is inferior to III-V epitaxy grown on its native substrate, the heterogeneous integration of III-V semiconductors on silicon using a wafer bonding technique is currently the most relevant solution for the fabrication of laser sources on silicon. In order to densely integrate the III-V semiconductor with the silicon waveguide circuits, mainly molecular wafer bonding and DVS-BCB adhesive bonding techniques are used and are actively reported in state-of-the-art hybrid amplifiers [2-3] and lasers [4-6]. In these approaches, unstructured InP-based dies are bonded, epitaxial layers down, on an SOI waveguide circuit wafer, after which the InP growth substrate is removed and the III-V epitaxial film is processed. In this paper we show that using a DVS-BCB adhesive bonding process compact heterogeneously integrated III-V/silicon multi-wavelength lasers can be realized, which are key optical components for wavelength division multiplexed optical networks and optical interconnects.

2. Device design

In order to realize a III-V/silicon multi-wavelength laser an intracavity wavelength (de)multiplexer is required, which can be implemented in different ways. Classically an arrayed waveguide grating (AWG) is implemented [7]. In this paper we implement a ring-resonator based (de)multiplexer, as shown in Figure 1(a). This offers some distinct advantages over an AWG: the ring resonator resonance wavelengths, defining the emission wavelengths of the different laser channels can be individually thermally tuned to provide an arbitrary and versatile channel spacing. Secondly, the ring resonator structure is more compact than AWGs, definitely when a small channel spacing is required. This wavelength (de)multiplexer is implemented in silicon photonics, using a 220 nm thick silicon guiding layer on a 2 μm buried oxide layer. The III-V thin film optical amplifier is implemented as a 3 μm wide mesa etched through to the n-type InP contact layer. In this particular device implementation the amplifier section was 500 μm long. The III-V layer stack consists of a p-InGaAs contact layer, a p-InP cladding layer (1.5 μm thick), six InGaAsP quantum wells (6 nm) surrounded by two InGaAsP separate confinement heterostructure layers (100 nm thick, bandgap wavelength 1.17 μm) and a 200 nm thick n-type InP layer. The optical coupling between the III-V amplifier waveguide and the silicon waveguide circuit is realized using an adiabatic spot size converter by tapering down the III-V waveguide width to below 500 nm and also implementing a taper in the silicon waveguide layer. In order to provide efficient optical coupling, the silicon taper is implemented in a 400 nm thick silicon rib waveguide structure

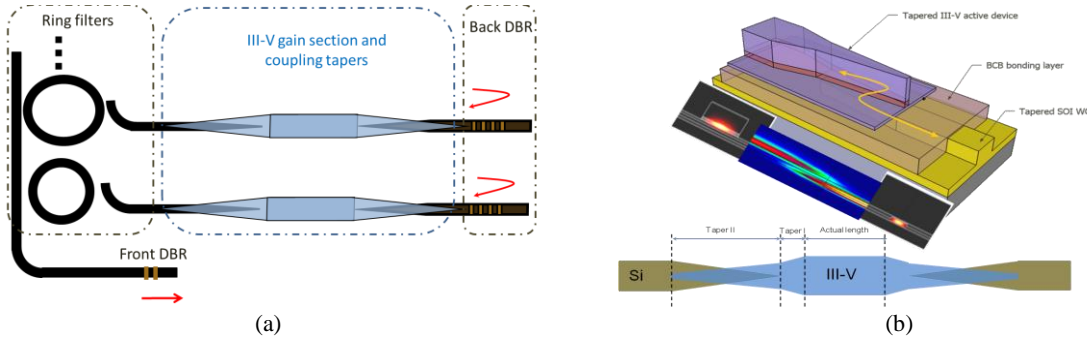


Figure 1: (a) Device layout of the realized III-V/silicon multi-wavelength laser; (b) sketch of the adiabatic spot-size converter used for optical coupling between the III-V amplifier waveguide and silicon waveguide layer.

(etched 180 nm), which is then in its turn efficiently coupled to the 220 nm device layer using a short adiabatic taper structure. The III-V/silicon taper structure, shown in Figure 1(b) consists of two sections: first, the III-V mesa is tapered from 3 μm to 900 nm over a length of 45 μm after which the III-V mesa is gradually tapered from 900 nm to 500 nm over a length of 150 μm . The silicon waveguide underneath tapers from 300 nm to 1 μm over 150 μm . The DVS-BCB bonding layer thickness, determining the separation between the silicon waveguide layer and the III-V layer is 110 nm in this implementation. The silicon (de)multiplexer circuit consists of 4 ring resonators coupled to the same bus waveguide. The free spectral range of the ring resonators is 15.5 nm and the loaded quality factor of the resonators is larger than 3000, providing sufficient suppression of longitudinal laser cavity modes adjacent to the lasing longitudinal mode (longitudinal mode spacing of 250 pm in this device implementation). The reflectors are implemented as distributed Bragg reflectors etched on the surface on the silicon waveguide layer, using a 290 nm grating period, 70 nm etch depth and 50% duty cycle. The high reflectivity mirror consists of 40 grating periods (resulting in a reflectivity > 90% and a 3dB bandwidth of 100 nm), while the partially reflecting mirror consists of 8 periods, resulting in 45 % maximum reflection and a 3dB bandwidth of 140 nm. For the interfacing to optical fiber, diffractive grating couplers structures are used, using the same 70 nm etch depth in the 220 nm device layer, but using a second order grating design (grating period 625 nm, 10 degree fiber angle).

3. Device fabrication

The fabrication process starts with the processing of the SOI wafer incorporating a 400 nm thick silicon waveguide layer in a CMOS pilot line. The first etch step comprises the definition of the 400 nm rib waveguides by etching 180 nm deep in the silicon waveguide layer. This at the same time also creates the 220 nm device layer for the implementation of the passive silicon circuitry. Next, the first order Bragg reflectors and second order fiber grating couplers are defined using a 70 nm etch step, while in a last step the 220 nm strip waveguide structures are defined. 193 nm deep UV lithography is used on 200mm SOI wafers to define these waveguide structures. An SiO₂ cladding layer is deposited and the wafer is planarized using chemical mechanical polishing (CMP). Next, the III-V epitaxial layer structure grown on its InP substrate is bonded upside down onto the silicon device layer, using a 110 nm thick DVS-BCB bonding layer. The details of this bonding process can be found in [8]. After bonding, the InP substrate is removed by wet chemical etching until an InGaAs etch stop layer is reached. This results in a III-V epitaxial layer stack attached to the silicon waveguide circuit, which can then be processed, lithographically aligned to the underlying SOI waveguide circuit. A Ti/Pt/Au stripe, acting as a p-side contact and also as a hard mask for the mesa etching was defined with a lift-off process using 320 nm UV contact lithography. Selectively wet etching was used to etch through the InGaAs layer, the InP p-doped layer and the MQW. Due to selected correct crystal orientation, a negative sidewall slope can be achieved in the anisotropic etching of InP. GeAu/Ni was used for the n-contacts. The active waveguide is encapsulated with DVS-BCB and extra Ti/Au contacts layers were added for the contact pads. Figure 2(a) shows a microscope image of the fabricated device, before p-type metallization. The III-V amplifier waveguides and the ring resonator (de)multiplexer array can clearly be identified. The footprint of the multi-wavelength laser structure is 1100 μm by 300 μm . Figure 2(b) shows a scanning electron microscope picture of the III-V taper tip fabricated using wet chemical etching as explained above.

4. Device characterization

The fabricated multi-wavelength laser is characterized on a temperature controlled stage at 20°C. The output power in the silicon waveguide versus drive current of the optical amplifiers is shown in figure 3(a), showing a threshold current of 31 mA, 31 mA, 33 mA and 39 mA for the four respective channels. The slope efficiency in the different

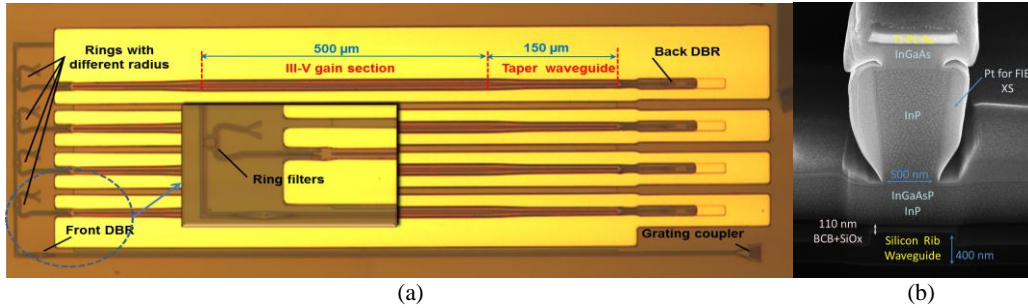


Figure 2: (a) microscope image of the fabricated multi-wavelength laser indicating the various subcomponents ; (b) scanning electron microscope image of the III-V adiabatic taper tips.

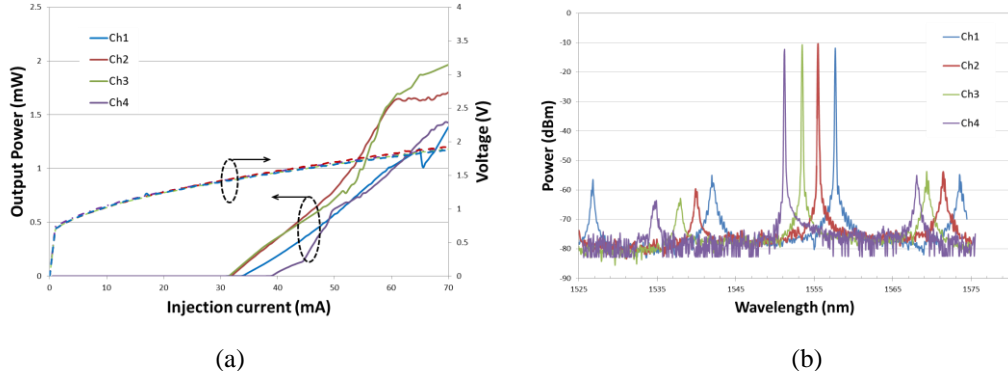


Figure 3: (a) waveguide-coupled optical output power versus amplifier drive current for the four different channels; (b) superimposed spectra of the four laser channels

channels varies between 30 mW/A and 37.5 mW/A. A waveguide-coupled output power between 1 and 2 mW is obtained. These levels of optical output power and electrical power consumption are compatible with practical applications. Figure 3(b) shows the lasing spectra of the four channels superimposed. A side mode suppression ratio better than 45 dB is obtained on all four channels.

5. Conclusion

In this paper we demonstrate the use of III-V on silicon heterogeneous integration to realize a multi-wavelength laser source with mW-level optical output powers and good spectral characteristics. Since the output light is coupled to a silicon waveguide, a next step is to externally modulate the multi-wavelength continuous wave signal using low power consumption silicon ring resonator modulators [9]. This way low power consumption wavelength division multiplexed transmitters can be envisioned based on this III-V on silicon waveguide platform. Recently, we demonstrated the co-integration of III-V-on-silicon lasers with silicon high-speed electro-optic modulators [10].

6. References

- [1] S. Selvaraja, W. Bogaerts, P. Dumon, D. Van Thourhout, R. Baets, "Sub-nanometer linewidth uniformity in silicon nano-photonic waveguide devices using CMOS fabrication technology , " IEEE Journal on Selected Topics in Quantum Electronics, 16(1), p.316 - 324 (2010)
- [2] H. Park, A. W. Fang, O. Cohen, R. Jones, M. J. Paniccia, and J. E. Bowers, "An electrically pumped AlGaInAs-Silicon Evanescent Amplifier," IEEE Photon. Technol. Lett. 19, 230-232 (2007).
- [3] S. Keyvaninia, G. Roelkens, et al., "A highly efficient electrically pumped optical amplifier integrated on a SOI waveguide circuit," in Proc. IEEE Group IV Photonics Conf., San Diego, United States, Sep. (2012)
- [4] M. Lamponi, S. Keyvaninia, et al., "Low-Threshold Heterogeneously Integrated InP/SOI Lasers With a Double Adiabatic Taper Coupler," IEEE Photon. Technol. Lett. 24, 76-78 (2012).
- [5] A. W. Fang, H. Park, O. Cohen, R. Jones, M. J. Paniccia, and J. E. Bowers, "Electrically pumped hybrid AlGaInAs-silicon evanescent laser," Opt. Express 14, 9203-9210 (2006).
- [6] G. Roelkens et al., "III-V/silicon photonics for on-chip and inter-chip optical interconnects," Laser Photonics Rev. 4(6) p. 751 – 779 (2010).
- [7] G. Kurczveil, M. Heck, J. Peters, J. Garcia, D. Spencer, and J. Bowers, "An integrated hybrid silicon multi-wavelength AWG laser," IEEE Selected Topics in Quantum Electronics 17(6), p. 1521-1526 (2011).
- [8] S. Keyvaninia et al. , "Multiple die-to-wafer adhesive bonding for heterogeneous integration," ECIO, p.186 (2012)
- [9] Q. Xu et al., "micrometer-scale silicon electro-optic modulator," Nature 435, p. 325 (2005).
- [10] G. Duan et al., 10Gb/s integrated tunable hybrid III-V/Si laser and silicon MZ modulator, 38th European Conference and Exhibition on Optical Communication (ECOC 2012), Netherlands, p.paper Tu.4.E.2 (2012)

Acknowledgements - This work was carried out in the framework of the EU FP7 integrated project HELIOS.

Unidirectional Emission AlGaInAs Microlasers with 3dB Bandwidth of 13 GHz

Yong-Zhen Huang, Xiao-Meng Lv, Heng Long, Ling-Xiu Zou, Qi-Feng Yao, Jin-Long Xiao, and Yun Du

*State Key Laboratory on Integrated Optoelectronics, Institute of Semiconductors,
Chinese Academy of Sciences, PO Box 912, Beijing 100083, China
E-mail: yzhuang@semi.ac.cn*

Abstract: Unidirectional emission circular AlGaInAs microlasers connected with an output waveguide are fabricated. Small signal modulation with 3dB bandwidth of 13 GHz is realized at 290 K with an injection current of 20 mA.

OCIS codes: (250.5960) Semiconductor lasers; (140.3948) Microcavity devices

1. Introduction

Semiconductor whispering-gallery mode microlasers have attracted a great attention for applications as light sources in photonic integrated circuits and optical interconnections. Recently, we proposed and fabricated unidirectional emission circular microlasers by directly connecting an output waveguide to the circular resonator [1,2]. In addition to unidirectional emission, high speed direct modulation is an important factor for the practical application of semiconductor microlasers, especially as a low cost light source. However, the reported experimental modulation rates are smaller than 10 Gb/s for microcircular and microring lasers [3,4]. Based on the conventional rate equation model, we expected that high cavity Q factor and low internal absorption loss are important for microlasers to realize high speed modulation and high-quality eye diagrams [5]. But an excessively high passive cavity Q factor can result in a degenerated eye diagram due to the prolonged turn-off delay.

Microcircular resonator connected with an output waveguide is a suitable choice for controlling the cavity Q factor to realize high modulation bandwidth, because the mode Q factor is related to the width of the output waveguide. In this talk, we report the fabrication and characteristics of AlGaInAs/InP circular microlasers, which are laterally confined by a BCB cladding layer, by planar technique processes. Small signal modulation and large signal responses are demonstrated for the microlasers experimentally. Small signal modulation with 3dB bandwidth of 13 GHz is realized for a circular microlaser with a radius of 10 μm and an output waveguide of 2 μm width at 290 K. In addition, large signal responses are presented at a bit rate of 12.5Gbit/s.

2. Fabrication for microlasers

An AlGaInAs/InP laser wafer with six compressively strained quantum wells is used for fabricating circular microcylasers confined by a BCB layer. The thicknesses of the quantum wells and barrier layers are about 5.5 nm and 9 nm, which are sandwiched between two 100 nm AlGaInAs cladding layers. The upper layers are p-InP and InGaAs contacting layers with a total thickness of 1.8 μm . An 800-nm SiO₂ is firstly deposited by plasma enhanced chemical vapor deposition (PECVD) on the laser wafer, and the patterns of microresonators with an output waveguide are transferred onto the SiO₂ layer using standard photolithography and inductively coupled-plasma (ICP) etching techniques. Then the patterned SiO₂ is used as hard masks for etching AlGaInAs/InP by ICP technique with an etching depth of about 5 μm . After removing the reactants and smoothing the side walls by a wet chemical process, the residual SiO₂ hard masks are removed using HF solution, and a 200-nm silicon nitride (SiN_x) layer is deposited by PECVD on the wafer to get better adherence to BCB and protect the resonators from the later RIE etching process. Afterwards, the DVS-BCB Cyclotene 3022-46 is coated twice to create a planar surface, and the hard cured BCB film is etched by RIE etching technique to expose the top of the microresonators. Then, a 450-nm SiO₂ layer is deposited on the whole wafer, and the contact window is opened by ICP etching for current injection on the top of each resonator. Subsequently, Ti/Pt/Au p-electrode is deposited to form a 90- μm -diameter pad after a lift-off process. Finally, the laser wafer is mechanically lapped down to about 120 μm , and an Au-Ge-Ni metallization layer is used as n-type electrode.

Fig. 1 shows the scanning electron microscope (SEM) image of a fabricated circular microlaser after cleaving the output waveguide for measuring output power and lasing spectrum. The current injection region is on the center of the resonator, with a circular ring with the width of about 4 μm still covered by the isolated SiO₂ layer on the top of the resonator. The 2 μm wide output waveguide is connected to the upper side of the circular resonator, and a golden wire is welded on the lower right as shown in Fig. 1.

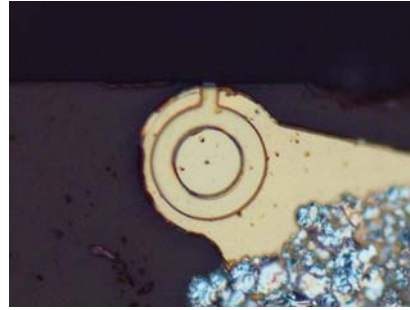


Fig. 1. SEM image of a circular microlaser after cleaving over the output waveguide. The center circle pattern is the current injection region. A welded golden wire is located at the lower right part.

3. Static behaviors of microlasers

The output power and laser spectra are measured for the circular microlaser by placing it on a thermoelectric cooler (TEC) in air. The output powers measured by a butt-coupling 5mm-diameter photodetector are plotted as function of continuous-wave (CW) injection current at the temperature of 290, 294, and 298K in Fig. 2(a) for a circular microlaser with a radius of 10 μm and a 2 μm wide output waveguide. The measured output powers at 30 mA are 39, 37 and 34 μW at 290, 294, and 298K, respectively. The threshold current is about 4mA corresponding to the kink of the output power versus the injection current. The laser spectrum measured at the injection current of 5 mA is plotted in Fig. 2(b), which shows single transverse mode operation with the longitudinal mode interval of 11 nm.

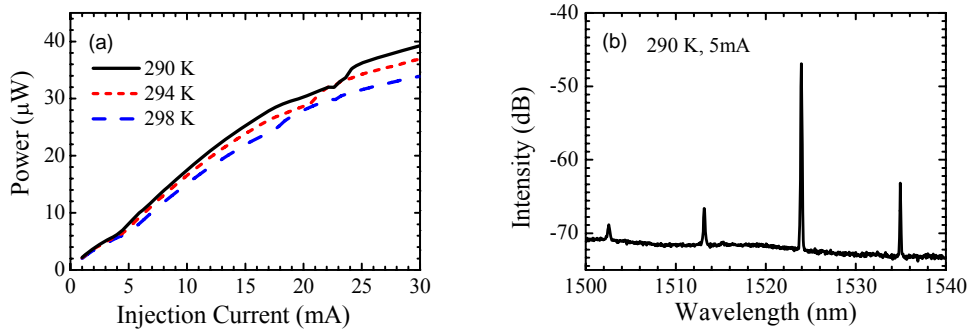


Fig. 2. (a) Output power measured by a butt-coupling photodetector versus CW injection current at the temperature of 290, 294 and 298 K, and (b) laser spectrum at the CW injection current of 5 mA and the temperature of 290 K, for a circular microlaser with a radius of 10 μm and a 2 μm wide output waveguide.

4. Dynamic characteristics of microlasers

The circular microlaser chips are bonded p-side up on an AlN submount with a thin-film 40 Ω resistance in series to match the impedance to 50 Ω for dynamic testing, and then the microlasers are mounted on the TEC to control the device temperature. In the measurement, the bias current is combined with the modulation signal using a high frequency bias-T and fed to the microlaser through a radio frequency probe. The output light from the microlaser was collected into a tapered single mode fiber and amplified by about 30 dB using an erbium-doped fiber amplifier (EDFA), then the amplified output was spectrally filtered using a tunable band-pass filter, and only the main lasing mode was monitored by an ac-coupled high speed photodetector with response bandwidth of 12 GHz.

The small signal modulation responses measured using a 20GHz bandwidth network analyzer are shown in Fig. 3(a) for the circular microlaser at 290 K, which has the 3dB-bandwidth increased from 9.9 to 13.0 GHz as the CW injection current increases from 10 to 20 mA. Furthermore, the large-signal modulation was measured by using a 12.5-Gbit/s pulse-pattern generator and a 20-GHz digital sampling oscilloscope. The large-signal direct modulation with the electric driving signal and the corresponding optical signal as shown in Fig. 3(b) are obtained by driving the microlaser with non-return-zero (NRZ) signals patterned at 12.5 Gbit/s under biasing current of 17 mA and modulation voltage of 2 V.

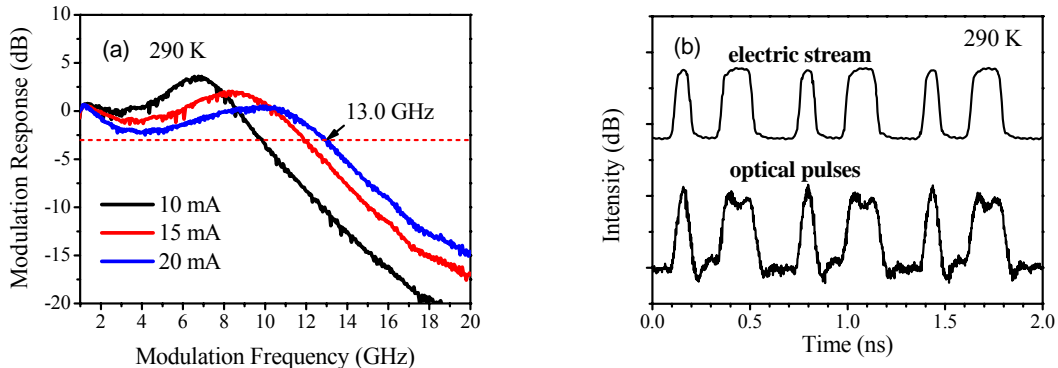


Fig. 3. (a) Small-signal frequency response at the CW injection current of 10, 15 and 20 mA, and (b) large signal modulation at 12.5 Gbit/s for the circular microlaser with the radius of 10 μm and a 2 μm wide output waveguide.

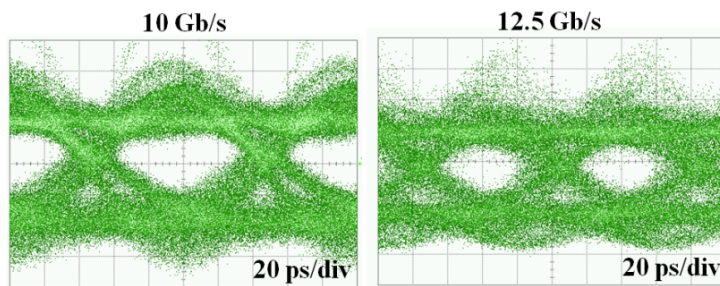


Fig. 4. Eye diagrams at 10 and 12.5 Gbit/s modulation for a 15- μm -radius microlaser laser with the 3dB bandwidth of 8.4 GHz.

However, we cannot obtain good eye-pattern from the above microlaser because the low output power coupled into a single mode fiber. For a microlaser with a radius of 15 μm , we have larger output power coupled into a single mode fiber and obtain the eye-diagrams of large signal modulation at 10 and 12.5 Gbit/s as shown in Fig. 4, which has the maximum 3dB bandwidth of 8.5 GHz at 40mA because of the higher parasitic capacitance.

5. Conclusion

In conclusion, unidirectional emission circular microlasers are fabricated, and high speed modulation with 3dB bandwidth of 13 GHz and large signal modulation at 12.5 Gbit/s are realized. Better performances of large signal modulation can be obtained for the microlasers with higher output coupling efficiency to single mode fiber. Based on the experimental results, we expect that 20Gbit/s large signal modulation can be reached from unidirectional circular microlasers with better coupling waveguide structure.

Acknowledgement

This work was supported by the National Nature Science Foundation of China under Grants 60838003, 61021003, 61106048, 61061160502 and 61006042, and the High Technology Project of China under Grant 2012AA012202.

References

- [1] Y. D. Yang, S. J. Wang, and Y. Z. Huang, "Investigation of mode coupling in a microdisk resonator for realizing directional emission," *Opt. Express* **17**, 23010-23015(2009).
- [2] X. M. Lv, L. X. Zou, J. D. Lin, Y. Z. Huang, Y. D. Yang, Q. F. Yao, J. L. Xiao, and Y. Du, "Unidirectional-emission single-mode AlGaInAs-InP microcylinder lasers", *IEEE Photon. Technol. Lett.* **24**, 963-965 (2012)
- [3] L. Liu, G. Roelkens, J. Van Campenhout, J. Brouckaert, D. Van Thourhout, and R. Baets, "III-V/silicon-on-insulator nanophotonic cavities for optical network-on-chip," *J. Nanosci. and Nanotechnol.* **10**, 1461-1472(2010).
- [4] A. Kapsalis, D. Syvridis, U. Troppenz, M. Hamacher, and H. Heidrich, "7Gb/s direct modulation of vertically coupled microring lasers," *2008 Conference on Optical Fiber Communication/National Fiber Optic Engineers Conference*, Vols **I-8**, 2917-2919(2008).
- [5] X. M. Lv, L. X. Zou, Y. Z. Huang, Y. D. Yang, J. L. Xiao, Q. F. Yao, and J. D. Lin, "Influence of mode *Q* factor and absorption loss on dynamical characteristics for semiconductor microcavity lasers by rate equation analysis", *IEEE J. Quantum Electron.* **47**, 1519-1525 (2011)

Low Cost Wide Waveguide Gap Polarization Mode Converter

Lingjie Wang^{1,2}, Yanli Zhao¹, Tianhong Zhou², Zheng Chen², Yuanzhong Xu¹, and Weidong Ma²

¹*Wuhan National Laboratory for Optoelectronics, School of Optoelectronics Science and Engineering, Huazhong University of Science and Technology, Wuhan 430074, China.*

²*Accelink Technologies Co., Ltd., Wuhan 430205, China
e-mail address: lingjie.wang@accelink.com*

Abstract: A new type of low cost polarization mode converter on basis of the segmented waveguide taper (SWT) has been proposed, which can reduce the excess loss drastically from 5dB to less than 1.5dB.

OCIS codes: (130.0130) Integrated optics; (230.0230) Optical devices; (130.3120) Integrated optics devices.

1. Introduction

The polarization dependency is a big problem in the low cost and high integrated optical network components. Several approaches have already been reported which achieved polarization insensitive operation [1-3]. Of these approaches, the TE/TM polarization mode converter is the most practical choice. In the polarization mode converter, a gap was diced and a half waveplate was inserted in the center of the gap. The use of the half waveplate can transform the polarization state between the TE and TM mode, and the light can propagate with the average refractive index when the half waveplate is positioned in the center of waveguide, therefore leading to polarization insensitivity. However, one problem coming with this technique is the large excess loss resulting from the insertion of the half waveplate, and a loss as large as 5 dB was reported for the converter when a 92 μm -thick quartz half waveplate was inserted into a 100 μm -wide waveguide gap [1].

There are two ways to reduce the excess loss, such as decreasing the waveguide gap width and enlarging the mode size of the waveguide gap. NTT developed a polarization mode converter with waveguide gap width as narrow as 18 μm . In the center of the narrow waveguide gap, a 14.5 μm -thick polyimide half waveplate was inserted into it to reduce the excess loss, and a polarization insensitive multiplexer was successfully made with a low excess loss of 0.26dB [3]. However, polyimide half waveplate has many disadvantages compared to quartz half waveplate, such as low mechanical robustness, unstable physical-chemical nature, and relatively high cost. On the other hand, some approaches to enlarge the mode size in the waveguide have also been reported in the literature. It is revealed that the lateral tapering is rather simple, but depth tapering typically requires a considerable effort. Much attention has been given to this subject, and several analyses have also been given [4-6]. However, most of these techniques require additional fabrication steps, which complicate the integration of the taper into the chip, and may degrade device performance and result in a low yield.

This paper presents a newly developed low loss polarization mode converter with a 92 μm -thick quartz half waveplate. The measurements showed that this polarization mode converter reduced the excess loss from 5 dB as reported in [1] to a low value less than 1.5dB. Considering the obviously wide waveguide gap and thick low cost quartz half waveplate adopted in this work, a comparison with the polarization mode converter using the polyimide half waveplate reveals that our newly developed polarization mode converter on basis of the SWT mode adapter is a very promising candidate for low cost, high reliable silica-based PLC device.

2. Polarization mode converter design

The new structure we proposed in this work called SWT mode adapter, which is used in the new wide waveguide gap polarization mode converter, as shown in Fig.1. The newly developed polarization mode converter is composed of an input taper section called SWTI, a PSW (periodically segmented waveguide) section and an output taper section called SWTO. SWTO is symmetrical to the SWTI. According to the equivalent waveguide theorem [7], this structure can be analyzed as a continuous waveguide with refractive index gradually changing along the longitudinal direction. As a result the mode size will change both in width and depth. The mode size depends on the combination of the duty cycle (DC) and the waveguide width. The SWTI acts as the PSW taper, which is beneficial to enlarge the mode size both in width and in depth direction. Once reached the desired duty cycle, the mode size can be stabilized due to a PSW. The inclusion of the PSW section is to maintain the large mode size with uniform DC, the wide waveguide gap was diced in this section too. The SWTO is used to decrease the mode size to match with the output continuous waveguide.

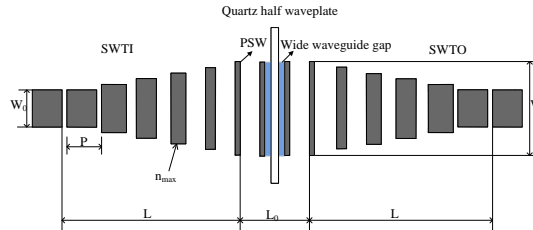


Fig.1 Schematic view of the proposed wide waveguide gap polarization mode converter with SWT mode adapter.

The parameters we can choose when designing the SWT mode adapter include the length L of the SWTI and SWTO, the segmentation period P , the width W and DC of the PSW section. In the case of the SWTI, it is varying from DC=1 (continuous waveguide) to a smaller DC with a constant period P , also the taper increases from W_0 to W gradually so that the mode size can be maximized in the PSW section. DC varies linearly with propagation distance. For SWTI section, the effective index decreases with the decrease of DC but increases with the gradual increase of the waveguide width. The mode size also enlarges with the gradual increase of the waveguide width. When finding an appropriate DC and W , the effective index is the optimal, and the mode size becomes the largest in the PSW section. The optimized effective index keeps a constant due to a fixed DC and W to ensure the maximal mode size. The wide waveguide gap is located in the PSW section, and the maximal mode size will lead to the smallest excess loss. The DC of the SWTO is varying from a constant DC to 1 with a constant period P , also the width becomes narrower gradually so that the mode size will match with the continuous waveguide mode. The excess loss of this polarization mode converter is comprised of segmented loss and wide waveguide gap induced loss. Segmented loss can be minimized by choosing a proper L , L_0 , P , W and DC. Wide waveguide gap induced excess loss can be minimized by maximizing mode size of the PSW section.

3. Simulation Results

The initial waveguide structure was optimized for small losses and to be single-mode operation at $1.55 \mu\text{m}$ wavelength. The SiO_2 waveguide is $6 \mu\text{m}$ thick, $6 \mu\text{m}$ wide and has a $\Delta=0.75\%$ index contrast, where Δ is the relative index difference between the core and cladding. Simulations were carried out by using 3-D FD-BPM [7] with OlympIOs integrated optical software at a wavelength of $1.55 \mu\text{m}$, the propagation step size (Δz) was $0.1 \mu\text{m}$, all the simulations were carried out with the transverse electric (TE) mode.

The excess loss of the polarization mode converter is composed of the transmission loss of the SWT mode adapter, the radiation loss in the waveguide gap, the absorption loss in the quartz half waveplate, and the Fresnel reflection loss at the waveplate surfaces. From [8] it is known that absorption loss in the half waveplate and Fresnel reflection loss at the waveplate surfaces is very low, therefore the excess loss mainly includes the contribution from the transmission loss and radiation loss. For the polarization mode converter on basis of the SWT mode adapter, $L=600 \mu\text{m}$, $W=8.8 \mu\text{m}$, $DC=0.55$, $P=11 \mu\text{m}$ are the optimal parameters, and the excess loss is as low as 0.9 dB .

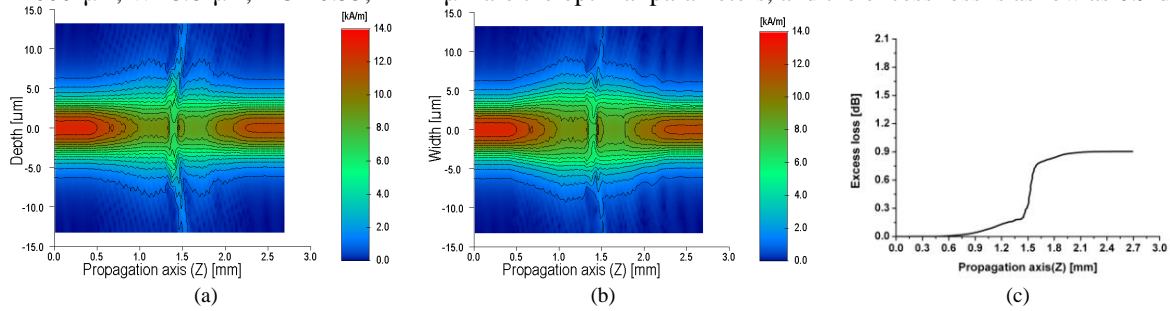


Fig.3 (a) Intensity and contour propagating field of the depth direction. (b) Intensity and contour propagating field of the width direction. (c) Excess loss of the polarization mode converter with SWT mode adapter.

The simulation results from the BPM for a polarization mode converter on basis of the SWT mode adapter are shown in Fig.3. As can be seen from Fig.3 (a) and (b), along the propagation direction, mode size is the smallest and intensity is the strongest at first, and then the mode size enlarges and intensity becomes weaker through the mode adapter. The mode size achieves the largest at the wide waveguide gap section to reduce energy from radiating out, and result in less excess loss. It is believed that the larger mode size it gets, the smaller excess loss will be produced through the wide waveguide gap with half waveplate. After the half waveplate, the mode size

becomes smaller, and the intensity becomes stronger. At the end of the polarization mode converter on basis of the SWT mode adapter, the overlap is 81% of the beginning, and excess loss is 0.9 dB as shown in Fig.3(c).

4. Experiment Results

The SWT mode adapter structures are deposited by plasma enhanced chemical vapor deposition (PECVD) onto thermally oxidized silicon wafers. Waveguides are formed by reactive ion etching. To analyze carefully the SWT mode adapter in combination of simulation with experiment, we fabricated 30 samples of polarization mode converter each on basis of the SWT mode adapter in one chip using the same parameters. The SWT mode adapter is in the middle of each polarization mode converter chip, a 100 μm -wide waveguide gap is diced in the middle of it, and a 92 μm -thick quartz half waveplate was inserted into the waveguide gap filled with an index-matching liquid. The principal axis of the half waveplate is automatically set at 45° to the waveguide plane when the half waveplate was inserted into the gap. The half waveplate was finally fixed in the gap with an adhesive. The choosing process of this adhesive is very important for it determine the reliability of the converter.

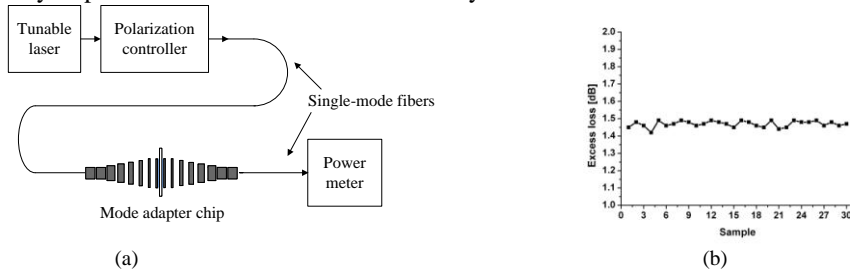


Fig.4 (a) Experimental setup. (b) Average excess loss of 30 polarization mode converter samples on basis of the SWT mode adapter

To measure the excess loss of each polarization mode converter, we couple two fiber arrays directly into the two ends of the chip. After being coupled into a fiber, the signal is measured with a power meter. Fig.4 (a) schematically shows the measurement setup system used. The measurement results of the 30 samples are shown in Fig.4 (b). The average excess loss is less than 1.5dB with the input wavelength from 1.52 μm to 1.57 μm and this result does not include the 0.3dB coupling loss between fiber array and the sample. It is found that the average excess loss of experimental results is about 0.6dB larger than the simulations. The main source of the discrepancy may come from the uneven of side walls and the partial etched surface of the SWT mode adapter. The surface roughness of the SWT mode adapter, refractive index difference of the index-matching liquid and waveguide will also affect the discrepancy. However, the improvement of the excess loss is larger than 3.5 dB compared to the experimental results from the traditional continuous waveguide.

5. Conclusion

We have proposed and demonstrated a novel polarization mode converter on basis of the SWT mode adapter to decrease the excess loss caused by the traditional polarization mode converter with wide waveguide gap and the quartz half waveplate. The excess loss of this polarization mode converter can be minimized by using an optimal L, W, DC and P. The simulation and measurement results indicate that the excess loss of this polarization mode converter can be reduced to less than 1.5dB. Our results suggest that polarization mode converter on basis of the proposed SWT mode adapter is a good choice for optical integration.

6. References

- [1] H.Takahashi, Y.Hibino, and I.Nishi, "Polarization-insensitive arrayed-waveguide grating wavelength multiplexer on silicon," Opt. Lett. 17, 499-501 (1992).
- [2] Y.Nasu, M.Oguma, T.Hashimoto, H.Takahashi, Y.Inoue, H.Kawakami and E.Yoshida, "Asymmetric half-wave plate configuration of PLC mach-zehnder interferometer for polarization insensitive DQPSK demodulator," J.Lightwave Technol. 27, 5348-5355(2009).
- [3] Y.Inoue, Y.Ohnmori, M.Kawachi, S.Ando, T.Sawada, and H.Takahashi, "Polarization mode converter with polyimide half waveguide in silica-based planar lightwave circuits," IEEE Photon.Technol.Lett. 6, 626-628(1994).
- [4] G.Wenger, L.Stoll, B.Weiss, M.Schienle, R.Müller-Nawrath, S.Eichinger, J.Müller, B.Acklin, and G.Müller, "Design and fabrication of monolithic optical spot size transformers(MOST's) for highly efficient fiber-chip coupling," J.Lightwave Technol. 12,1782-1790(1994).
- [5] O.Mitomi, K.Kasaya, H.Miyazawa, "Design of a single-mode tapered waveguide for low-loss chip-to-fiber coupling," IEEE J.Quantum Electron. 30, 1787-1793 (1994).
- [6] R.Zengerle, B.Jacobs, W.Weiershausen, K.Faltin, and A.Kunz, "Efficient spot-size transformation using spatially separated tapered InP/InGaAsP twin waveguides," J.Lightwave Technol. 14,448-453 (1996).
- [7] F.Fogli, G.Bellanca, P.Bassi, I.Madden, and W.Johnstone, "High efficient full-vectorial 3-D BPM modeling of fiber to planar waveguide couplers," J.Lightwave Technol. 17, 136-143 (1999).
- [8] Y.Inoue, H.Takahashi, S.Ando, T.Sawada, A.Himeno and M.Kawachi, "Elimination of Polarization Sensitivity in Silica-Based Waveguide Division Multiplexer Using a Polyimide Half Waveplate," J.Lightwave Technol. 15, 1947-1957(1997).

Theoretical Investigation on the Continuous Evolution of the Electron-Gas Dimensionality: from Bulk Materials to Quantum Dots

Xiaomin Ren*

*State Key Laboratory of Information Photonics and Optical Communications (Beijing University of Posts and Telecommunications), and Zh. I. Alferov Russian-Chinese Joint laboratory of Information Optoelectronics and Nanoheterostructures Beijing 100876, People's Republic of China
Email: xmren@bupt.edu.cn Tel: +86 10 62282044 Fax: +86 10 62285008*

Abstract: The intrinsic energy-dispersion at each energy level of electrons in a semiconductor material is assumed and then the electron-gas dimensionality could manifest a continuous evolution from 3 to 0. This leads to a new physical picture and may impact on relevant technologies.

Key words: electron-gas dimensionality; energy level dispersion; wave vector dispersion; quantum wells, wires and dots; density of states

1. Introduction

It has made the author puzzled for many years that, for a semiconductor material, it seems no accurate critical point exists for the evolution between a lower and a higher electron-gas dimensionality. The current theory of electron-gas dimensionality looks somewhat casual and quite limited in scope. It is known that every dimensionality from 3, 2, 1 to 0 has its ideal expression of the density of states. These elegant expressions differ from each other so dramatically that one cannot imagine how the SUDDEN transitions between them could happen with a GUADUAL changing of the material size. I have been wondering what physical processes truly happen at the half-way during these evolutions and how can we formulate the density of states in each of these half-way cases. In addition, it is surely unsatisfactory to explain the formation of energy bands in such a way: the adjacent levels are so near and can be treated APPROXIMATELY as a continuous band. This explanation works as merely a mathematical trick other than an intrinsic physical settlement.

In this paper, a quite successful step has been made to solve this problem by introducing a new concept: intrinsic energy level dispersion (originating from wave vector dispersion). It is believed that, in general, any electron energy level could not be an ideal line with zero-linewidth. Instead, all the energy levels are slightly but unexceptionally dispersive. It is this kind of dispersion that make different energy levels merging together and TRULY (not APPROXIMATELY) form a continuous energy band. Based on this assumption, a quite different story of electron-gas dimensionality can be told as follows.

2. The expression of the wave-vector dispersion

The energy level dispersion (ELD) introduced above is regarded as an “intrinsic” one. It would not originate from thermo-effect. This assumption is quite logical because it is believed that the dimensionality evolution should happen even at the temperature of 0 K. The position of the level defined by current theory can be regarded as the peak of a certain energy distribution. The linewidth of the distribution must be very narrow but, the most importantly, NOT ZERO! All these descriptions are also suitable to wave vector dispersion (WVD) because it is assumed that ELD is determined by WVD. Now, let us begin with the expression of WVD. Considering a simple case that the WVD happens just in one direction (for instance, in the k_z direction), then the WVD function can be initially conceived as follows:

$$F_D(k_z, n) = \begin{cases} A_2 e^{-\left(\frac{k_z - k_{zn}}{D_{A2}}\right)}, & k_{zn} \leq k_z < \infty \\ A_1 \left(e^{\frac{k_z}{D_{A1}}} - 1 \right), & 0 \leq k_z \leq k_{zn} \\ A_1 \left(e^{\frac{-k_z}{D_{A1}}} - 1 \right), & -k_{zn} \leq k_z \leq 0 \\ A_2 e^{\frac{k_z + k_{zn}}{D_{A2}}}, & -\infty < k_z \leq -k_{zn} \end{cases} \quad A_2 = A_1 \left(e^{\frac{k_{zn}}{D_{A1}}} - 1 \right) \quad (1)$$

This function has been plotted in Fig. 1 and Fig. 5 while a similar function regarding the k_y direction plotted in Fig. 3. This type of expression may not be the most proper one to describe the real fact. However, it is definitely helpful for us to make the first step to have this assumed phenomenon being modeled.

3. The density of states for the dimensionality between 3 and 2

First of all, the density of states for the 2-dimensional electron-gas is modified by introducing the WVD function (see Fig. 1). We may take the conduction band as the example and suppose the bottom of the conduction band is at Γ ($\vec{k}=0$). In the \vec{k} space, the two symmetrical planes specified by a discrete value of k_{zn} and $-k_{zn}$ were recognized in previous theoretical investigations as a “zero thickness” layers. However, now, the dispersion happens and the planes become broadened ones in the form defined in equation (1). So a \vec{k} space volume corresponding to the k_{zn} and $-k_{zn}$ planes in an interval of dk becomes a weighted integration with the WVD function as the weighting factor and can be calculated as follows:

$$d\Omega_D^* = dk \int_0^{2\pi} \int_{-\infty}^{\infty} F_D(k \cos \varphi, n) k^2 \sin \varphi d\theta d\varphi = 4\pi A_l k dk [K_n - D_{A2} e^{\frac{k_{zn}}{D_{A1}}} \cdot e^{-\left(\frac{k-k_{zn}}{D_{A2}}\right)}] \quad (2)$$

$$\text{where } K_n = (D_{A1} + D_{A2})(e^{\frac{k_{zn}}{D_{A1}}} - 1) - k_{zn} \quad (3)$$

It is known that

$$E = E_c + \frac{\hbar^2 k^2}{2m_n^*}, \quad dE = \frac{\hbar^2}{m_n^*} k dk, \quad E_{cn} = E_c + \frac{\hbar^2 k_{zn}^2}{2m_n^*} \quad (4)$$

where, m_n^* is the effective mass of an electron.

So, the corresponding density of states can be derived as follows:

$$\rho_c(E, k_{zn}) = \frac{\pi}{V} \left[\frac{L_x L_y}{(2\pi)^2} \right] \frac{d\Omega_D^*}{dE} = \left(\frac{m_n^*}{\pi \hbar^2 L_z} \right) \cdot 2A_l \left[K_n - D_{A2} e^{\frac{\sqrt{2m_n^*(E_{cn}-E_c)}}{\hbar D_{A1}}} \cdot e^{-\left(\frac{\sqrt{2m_n^*(\sqrt{E-E_c}-\sqrt{E_{cn}-E_c})}}{\hbar D_{A2}}\right)} \right] \quad (5)$$

Taking all the discrete values of k_{zn} and $-k_{zn}$ with ($n=1,2,3,\dots$) into account and the density of states with the electron-gas dimensionality between 3 and 2 can be derived as follows:

$$\rho_{c,2-3D}(E) = \sum_{n=1}^{\infty} \rho_c(E, k_{zn}) u(E - E_{cn}), \quad u(x) = \begin{cases} 1 & x \geq 0 \\ 0 & x < 0 \end{cases} \quad (6)$$

Such a density of states has been illustrated in Fig. 2 (see the solid line).

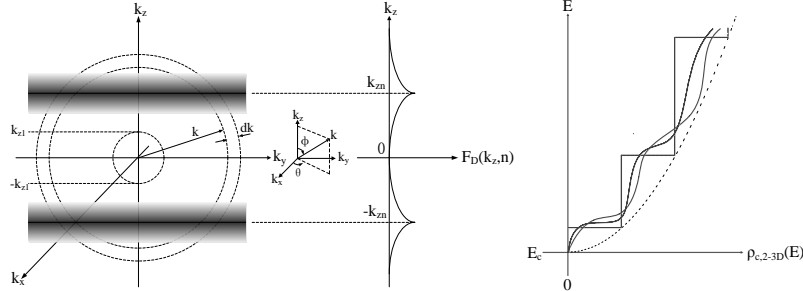


Fig.1

Fig.2

The dotted line in Fig. 2 is an illustration of $\rho_{c,2-3D}(E)$ when a Lorentzian-type expression of the WVD function is used. The similar illustrations of $\rho_{c,1-2D}(E)$ and $\rho_{c,0-1D}(E)$ with such a Lorentzian-type WVD are also shown with the dotted lines in Fig. 4 and Fig. 6.

4. The density of states for the dimensionality between 2 and 1

Secondly, as shown in Fig. 3, the density of states of 1-dimensional electron-gas is modified by introducing a similar WVD function. In the \vec{k} space, the two symmetrical wires specified by the discrete values of k_{ym} and $-k_{ym}$ within the k_{zn} plane were recognized as “zero diameter” ones previously. Here, they are also treated as dispersive

ones. So a \vec{k} space area corresponding to the k_{ym} and $-k_{ym}$ wires in an interval of dk becomes another weighted integration as follows:

$$dS_D^* = dk \int_0^{2\pi} F_D(k_y, m) k d\theta = k dk X(k), \quad X(k) = 4B_1[(e^{\frac{k_{ym}}{D_{B1}} - 1} \int_0^{\theta_I} e^{-\frac{k \cos \theta}{D_{B2}}} d\theta) + \int_{\theta_I}^{\frac{\pi}{2}} e^{\frac{k \cos \theta}{D_{B1}}} d\theta - (\frac{\pi}{2} - \theta_I)] \quad (7)$$

Similarly, the corresponding state densities $\rho_c(E, k_{ym})$ and $\rho_{c,1-2D}(E)$ can be derived as follows:

$$\rho_c(E, k_{ym}) = \frac{2}{V} \left[\frac{L_z}{2\pi} \right] \frac{dS_D^*}{dE} = \frac{m_n^*}{L_x L_y \pi \hbar^2} X(k), \quad \rho_{c,1-2D}(E) = \sum_{m=1}^{\infty} \rho_c(E, k_{ym}) u(E - E_{cm}) \quad (8)$$

The latter has been illustrated in Fig. 4 (see the solid line). And, in Eq. (8), $k = \frac{\sqrt{2m_n^*(E-E_c)}}{\hbar}$, $k_{ym} = \frac{\sqrt{2m_n^*(E_{cm}-E_c)}}{\hbar}$.

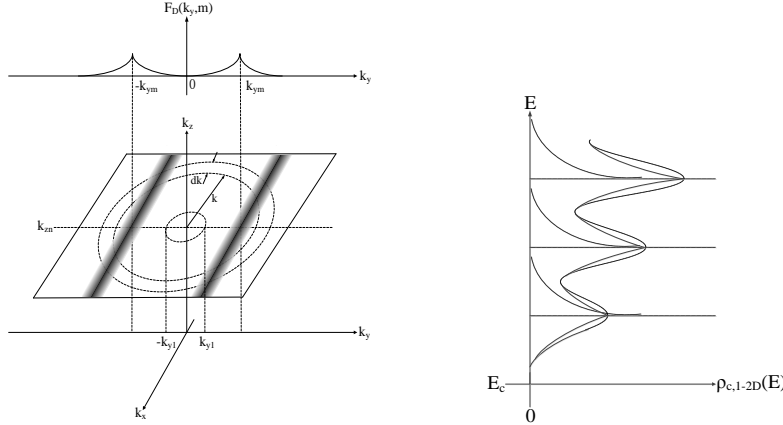


Fig.3

Fig.4

5. The density of states for the dimensionality between 1 and 0

Finally, as shown in Fig. 5, the density of states with the dimensionality of electron-gas between 1 and 0 is derived in a similar way. It is quite simple in comparison with the previous two cases. The derived result is as follows:

$$dl_D^* = 2F_D(k_z, l) dk \quad (9)$$

$$\rho_c(E, k_{zl}) = \frac{2}{V} \delta(E - E_{cl}) \frac{dl_D^*}{dE} = \frac{\sqrt{2m_n^*}}{L_x L_y L_z \hbar \sqrt{E - E_{cl}}} \delta(E - E_{cl}) \bullet 2F_D(k_z, l), \quad \rho_{c,0-1D}(E) = \sum_{l=1}^{\infty} \rho_c(E, k_{zl}) u(E - E_{cl}) \quad (10)$$

The illustration of $\rho_{c,0-1D}(E)$ is shown in Fig. 6 (see the solid line).

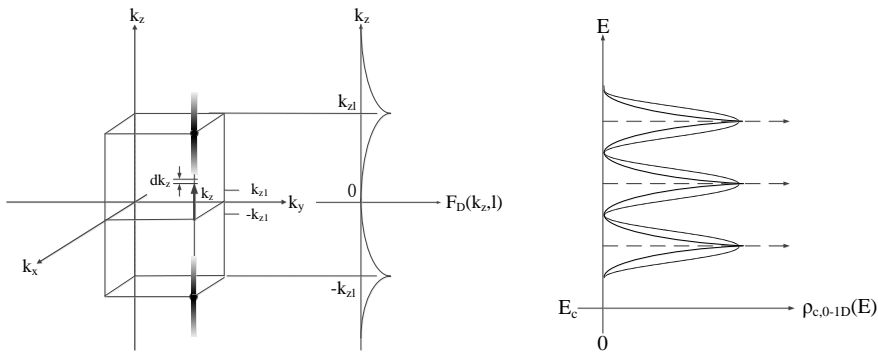


Fig.5

Fig.6

6. Definitions for the description of the continuous dimensionality

The critical values of L_x , L_y and L_z for the dimensionality evolution can be determined and 0D, 1D, 2D and 3D regions can be defined as follows:

$$\int_{E_c}^{\infty} \rho_{c,0\sim 1D}(E, L_z) \rho_{c,mn}(E, L_z) dE = \int_{E_c}^{\infty} \rho_{c,0\sim 1D}(E, L_z) \rho_{c,mn}(E, L_z) dE \Rightarrow L_{z,1D} \quad (11)$$

$$\int_{E_c}^{\infty} \rho_{c,1\sim 2D}(E, L_y) \rho_{c,mn}(E, L_y) dE = \int_{E_c}^{\infty} \rho_{c,1\sim 2D}(E, L_y) \rho_{c,n}(E, L_y) dE \Rightarrow L_{y,2D} \quad (12)$$

$$\int_{E_c}^{\infty} \rho_{c,2\sim 3D}(E, L_x) \rho_{c,n}(E, L_x) dE = \int_{E_c}^{\infty} \rho_{c,2\sim 3D}(E, L_x) \rho_c(E, L_x) dE \Rightarrow L_{x,3D} \quad (13)$$

$$\begin{cases} 0D: (0 \leq L_z, L_y, L_x < L_{z,1D}) \\ 1D: (L_{z,1D} \leq L_z < \infty, 0 \leq L_y, L_x < L_{y,2D}) \\ 2D: (L_{z,1D} \leq L_z < \infty, L_{y,2D} \leq L_y < \infty, 0 \leq L_x < L_{x,3D}) \\ 3D: (L_{z,1D} \leq L_z < \infty, L_{y,2D} \leq L_y < \infty, L_{x,3D} \leq L_x < \infty) \end{cases} \quad (14)$$

The values denoting the continuous dimensionality in 0D, 1D, and 2D regions can be defined respectively as follows:

$$D_{0\sim 1}^{\#}(L_z) = \frac{\int_{E_c}^{\infty} \rho_{c,0\sim 1D}(E, L_z) \rho_{c,mn}(E, L_z) dE - \int_{E_c}^{\infty} \rho_{c,0\sim 1D}(E, L_z=0) \rho_{c,mn}(E, L_z=0) dE}{\int_{E_c}^{\infty} \rho_{c,0\sim 1D}(E, L_{z,1D}) \rho_{c,mn}(E, L_{z,1D}) dE - \int_{E_c}^{\infty} \rho_{c,0\sim 1D}(E, L_z=0) \rho_{c,mn}(E, L_z=0) dE} \quad (0D \text{ region}) \quad (15)$$

$$D_{1\sim 2}^{\#}(L_y) = 1 + \frac{\int_{E_c}^{\infty} \rho_{c,1\sim 2D}(E, L_y) \rho_{c,n}(E, L_y) dE - \int_{E_c}^{\infty} \rho_{c,1\sim 2D}(E, L_y=0) \rho_{c,n}(E, L_y=0) dE}{\int_{E_c}^{\infty} \rho_{c,1\sim 2D}(E, L_{y,2D}) \rho_{c,n}(E, L_{y,2D}) dE - \int_{E_c}^{\infty} \rho_{c,1\sim 2D}(E, L_y=0) \rho_{c,n}(E, L_y=0) dE} \quad (1D \text{ region}) \quad (16)$$

$$D_{2\sim 3}^{\#}(L_x) = 2 + \frac{\int_{E_c}^{\infty} \rho_{c,2\sim 3D}(E, L_x) \rho_c(E, L_x) dE - \int_{E_c}^{\infty} \rho_{c,2\sim 3D}(E, L_x=0) \rho_c(E, L_x=0) dE}{\int_{E_c}^{\infty} \rho_{c,2\sim 3D}(E, L_{x,3D}) \rho_c(E, L_{x,3D}) dE - \int_{E_c}^{\infty} \rho_{c,2\sim 3D}(E, L_x=0) \rho_c(E, L_x=0) dE} \quad (2D \text{ region}) \quad (17)$$

7. Conclusion

In this paper, a new concept of the intrinsic energy dispersion (or wave vector dispersion) has been proposed. This concept leads to a new physical picture of continuous electron-gas dimensionality from 3 to 0 (fractional dimensionalities could exist). The evolution of the dimensionality has been interpreted quite reasonably (the author now believe that the Lorentzian WVD function should be a better choice). Some new possibilities for conceiving novel electronic and optoelectronic devices could be expected. Especially, it would have provided an important basis for the understanding and furthermore the utilization of hetero-dimensional structures.

8. Acknowledgement:

I would like to express my deep gratitude to Prof. Zh. I. Alferov for his enlightening words. I am very grateful to my colleagues for their support and to my students, JIA Zhigang, LUO Yang, HU Fuquan, Fan Xinye, LIU Xiaolong and LI Liang, for their help to prepare the print ready figures, make proper format editing of the text and make a quick submission. This work was supported by the National Basic Research Program of China (No. 2010CB327601), the National Natural Science Foundation of China (No. 61020106007, 61108048), International Science & Technology Cooperation Program of China (No.2011DFR11010) and the 111 Project (No. B07005).

9. References

- [1] Zhores I. Alferov, The double heterostructure: concept and its applications in physics, electronics and technology, Nobel Lecture, December 8, 2000

Cortical Response During Motor Task in Epileptic Patients with Movement Disorders: A Multimodality fNIRS-EEG, fMRI-EEG and TMS Clinical Study

Alessandro Torricelli¹, Davide Contini¹, Matteo Caffini¹, Lucia Zucchelli¹, Rinaldo Cubeddu¹,
 Lorenzo Spinelli², Erika Molteni³, Anna Maria Bianchi³, Giuseppe Baselli³, Sergio Cerutti³
 Elisa Visani⁴, Isabella Gilioli⁴, Davide Rossi Sebastian⁴, Elena Schiaffi⁴, Ferruccio Panzica⁴, Silvana
 Franceschetti⁴

¹Dipartimento di Fisica, Politecnico di Milano, piazza Leonardo da Vinci 32, I-20133 Milan, Italy

²Istituto di Fotonica e Nanotecnologie, CNR, piazza Leonardo da Vinci 32, I-20133 Milan, Italy

³Dipartimento di Bioingegneria, Politecnico di Milano, via Golgi 39, I-20133 Milan, Italy

⁴Unità Operativa Neurofisiopatologia ed Epilettologia diagnostica, Centro per l'Epilessia, Fondazione IRCCS Istituto Neurologico Carlo Besta,
 via Celoria 11, I-20133 Milan, Italy
 lorenzo.spinelli@fisi.polimi.it

Abstract: Cortical response during motor tasks was assessed by a multimodality fNIRS-EEG, fMRI-EEG and TMS clinical study on adult volunteers and epileptic patients with movement disorders.

OCIS codes: (170.2655) Functional monitoring and imaging; (170.5280) Photon migration; (170.6920) Time-resolved imaging; (170.3890)

1. Introduction

Human brain mapping by multimodality approaches has been proposed as an integrated methodology towards a deeper understanding of cortical response. The proper combination of different functional imaging modalities in fact would allow improving the description of spatial and temporal distribution of neural activations following specific stimuli [1-2]. Integration of functional magnetic resonance imaging (fMRI) or functional near infrared spectroscopy (fNIRS) with electroencephalography (EEG) has the potentiality to monitor neuronal and vascular response. Recent studies have also combined fMRI with fNIRS aiming not only at the validation of fNIRS per se, as a brain mapping technique, but also at contributing to elucidate the blood-oxygen-level-dependent (BOLD) effect in fMRI [3-5]. Recently, also transcranial magnetic stimulation (TMS) has been used to study in particular the motor system and higher brain functions in healthy and diseased states (e.g. multiple sclerosis, motor neuron disease, stroke, epilepsy, and movement disorders) [2].

In this work we present a multimodality approach based on fNIRS-EEG, fMRI-EEG and TMS on adult volunteers and epileptic patients with movement disorders during motor task. The work is performed within the European project nEUROPt [6] aiming at assessing the potentiality of time domain fNIRS for noninvasive imaging of brain function and disease by pulsed light.

2. Materials and methods

2.1 Motor task

Fourteen healthy volunteers (9 male: age range 24 - 65y, mean age 40 ± 12 y; 5 female, age range: 24 - 35y, mean age 27 ± 4 y), all right handed, with no history of neurological disease, and 11 patients (8 male: age range 27 - 50y, mean age 39 ± 9 y; 3 female: age range 22 - 65y, mean age 44 ± 30 y) all right handed with Unverricht-Lundborg disease genetically assessed, were enrolled in the experiment. The experiment was approved by the Ethic Committee of Fondazione IRCCS Istituto Neurologico C. Besta. The motor task consisted in hand grip (i.e. clutching a soft ball) at 2Hz rate, guided by a metronome. After an initial 40s resting period, 10 trials were executed by alternating 20s task and 20s rest, then a recovery of 50s ended the exercise. Three different paradigms were successively executed: right hand vs. rest, left hand vs. rest, left hand vs. right hand. Instructions about which task to perform were given visually by presenting a picture on a screen. A fixation cross was always present in the center of the screen. The total duration of the protocol is about 24 minutes (8 minutes/paradigm).

2.2 Time domain fNIRS

The multichannel dual wavelength medical device for time domain fNIRS developed at the Department of Physics, Politecnico di Milano was used [7]. A total of 15 detection bundles and 8 light sources were positioned over the left and right hemisphere centered on C3 and C4. Sequential illumination of pairs of light sources in the left and right

hemisphere every 0.25s allowed for the acquisition of 30 channels with an overall acquisition time of 1s. Oxygenated hemoglobin [oxy-Hb] and deoxygenated hemoglobin [deoxy-Hb] changes in the cortical region were estimated by the method described in [8] based on the use of late time-gate to enhance the contribution of signal from the deeper cortical region and to reject the contribution from superficial layers (i.e. scalp, skull). General linear models (GLM) were applied to single subjects and to the whole group by using the NIRS-SPM software [9]. Time series of [oxy-Hb] and [deoxy-Hb] for any given channel were modeled as a linear combination of regressors (known functions) plus an error term. Hypotheses on predictor variables could be tested constructing the F statistic. Within the analysis protocol, a good trade-off between statistical reliability and temporal resolution was found by analyzing data with constant regressors. The task was modeled as a series of consecutive boxcars that represented an equal number of activation periods, chosen accordingly to the different activities performed during the experiment.

2.3 fMRI

MR images were acquired with a 1.5T MR scanner (Magnetom Avanto, Siemens, Erlanger, Germany). The fMRI data were analyzed using the SPM8 software (Neuroimaging Wellcome Dept., Institute of Neurology, London, UK). Pre-processing included motion and slice-timing correction, normalization into the Montreal Neurological Institute (MNI) space and smoothing. The first level analysis was performed by GLM, entering as regressor the box-car function of the block task convolved with the canonical hemodynamic response function. In addition to individual subject analysis, a fixed-effect (second level) analysis was performed to calculate the group activation map.

2.4 EEG

EEG data were recorded simultaneously with time domain fNIRS and with fMRI. For the EEG-fMRI recordings, an MR compatible device (SD MRI 32, Micromed, Treviso, Italy) and a cap providing electrodes positioned according to the international 10-20 system were used. The removal of scanning artifacts was performed using the software provided with the EEG system. For the EEG-NIRS recordings, a standard 19 electrodes configuration was used. EMG from flexor muscles and ECG signal were also acquired. EEG pre-processing consisted in filtering (1-120 Hz, notch filter), artefacts rejection with Independent Component Analysis, and montage reformatting using the surface Laplacian operator. To investigate the functional activation of cortical areas involved in the movement execution, we used Event-Related Desynchronization/Synchronization (ERD/ERS) analysis. For each subject and for the group, we evaluated the time course and scalp topography of the ERD/ERS.

2.5 TMS

TMS-based mapping of primary motor cortex of the hand associated to real-time frameless neuronavigation system was performed. Muscle evoked potentials were obtained by superficial electrodes placed on the muscle Opponens Pollicis contralateral to the site of stimulation. The intensity of stimulation was 125% of the intensity of the resting motor threshold obtained in the position C3 (left hemisphere) or C4 (right hemisphere). Stimulation of 35 points (placed around motor cortex) based on international 10-10 system was performed with an “eight-shaped” coil. As post-analysis the following procedures were performed: averaging of 4-6 stimuli for each point of stimulation, digitalization of the spatial coordinates of each point of stimulation with a frameless neuronavigation system, and calculation of center of gravity of the motor maps for each hemisphere. The center of gravity of the motor outputs of each subject estimated by TMS was used as the most accurate estimation of the location of the represented muscle in the motor cortex.

3. Results and discussion

As general outcome we found that results of individual and group analyses on volunteers agree with literature. Functional activation was detected by fNIRS as an increase in [oxy-Hb] and a corresponding non symmetrical decrease in [deoxy-Hb] in the contralateral hemisphere in channels closely located to C3 (or C4). fMRI maps revealed activation in the primary motor area contralateral to the movement and in the supplementary motor area. EEG measurements revealed α -ERD and β -ERD in central areas during movement execution (more evident in contralateral area), β -ERS in contralateral area immediately after the movement offset. Results are confirmed in group analysis. All centers of gravity lie around C3 and C4 positions, but differences in center of gravity location was observed among subjects. In most of the cases maps obtained by TMS show good correlation with fMRI, EEG and NIRS data.

In Fig. 1(left panel) the outcomes of the multimodality approach for volunteers (group analysis) performing the motor task “right vs. rest” are compared: [oxy-Hb] and [deoxy-Hb] time courses, static maps of α movement-related desynchronization from EEG, fMRI activation map, static representation of activated area/s fNIRS maps with GLM, and maximal response (hot-spot) and center of gravity and maps by TMS. In Fig. 1(right panel) the outcomes of the multimodality approach for patients (group analysis) are shown. The elicited fNIRS response in patients is generally more limited than in volunteers, both in terms of spatial extension and of intensity of hemodynamic changes.

Concerning location of the activation, fNIRS results are however consistent with fMRI and TMS responses. Overall the fMRI and TMS activation maps show no significant difference with volunteers. The ERD/ERS analysis confirmed the described absence or reduction of post movement synchronization in β band [10].

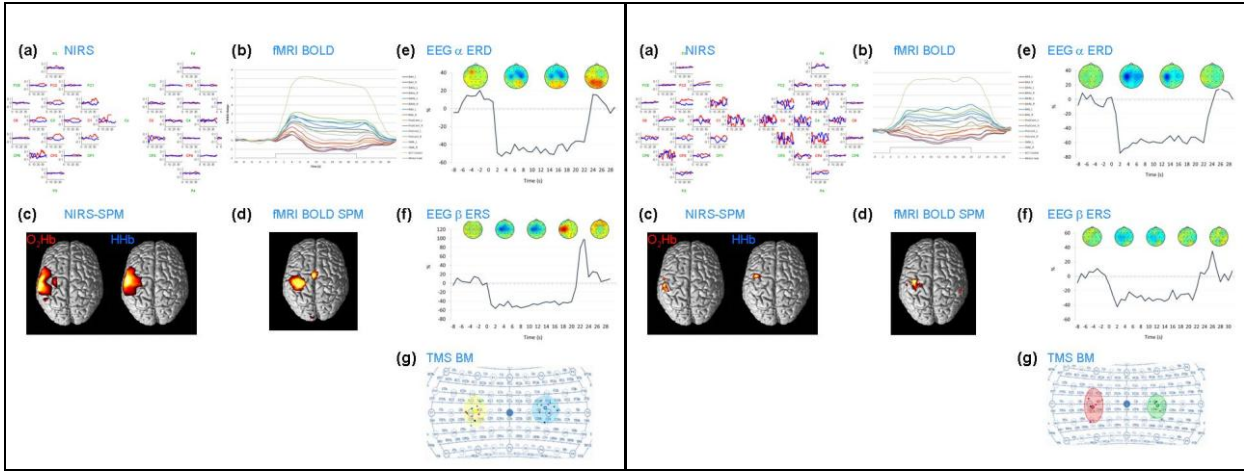


Fig.1. Second level (group) analysis on volunteers (left panel) and patients (right panel) (motor task right vs. rest). In each panel: (a) [oxy-Hb] (red), and [deoxy-Hb] (blue) time courses; (b) fMRI BOLD time courses; (c) [oxy-Hb] and [deoxy-Hb] activation maps obtained by NIRS SPM ($p < 0.05$); (d) fMRI BOLD activation map ($p < 0.001$ un-corrected); (e) α -ERD maps and time courses; (f) β -ERS maps and time courses; (g) TMS center of gravity projected on International 10/20 System.

4. Conclusions

We verified that different neuroimaging techniques can be easily applied and co-applied. All topographic results in volunteers (e.g. TMS center of gravity, maximum of fNIRS deflection and maximum of EEG-ERD) were related to and within the area of fMRI activation, assumed as gold standard. Results on patients suggest that the fNIRS response is limited than in volunteers. The use of the NIRS-SPM tool is helpful for the comparison of fNIRS and fMRI response. Work is in progress to develop and optimize data fusion strategies (e.g. fNIRS/fMRI GLM with EEG as regressors), and data comparison between the time courses of BOLD-fMRI, time domain fNIRS and ERD-EEG. We acknowledge the support from the EC's 7 Framework Programme (FP7/2007-2013) under grant n. 201076 (nEUROPt).

5. References

1. C. Büchel, and K. Friston, "Interactions among neuronal systems assessed with functional neuroimaging," *Rev Neurol* **157**:807-15 (2001).
2. A. Inuggi, M. Filippi, R. Chieffo, F. Agosta, M.A. Rocca, J.J. González-Rosa, M. Cursi, G. Comi, and L. Leocani, "Motor area localization using fMRI-constrained cortical current density reconstruction of movement-related cortical potentials, a comparison with fMRI and TMS mapping," *Brain research* **1308**:68-78 (2010).
3. J. Steinbrink, A. Villringer, F. Kempf, D. Haux, S. Boden, and H. Obrig, "Illuminating the BOLD signal: combined fMRI-fNIRS studies," *Magn Reson Imag* **24**:495-505 (2006).
4. T.J. Huppert, R.D. Hoge, S.G. Diamond, M.A. Franceschini, and D.A. Boas, "A temporal comparison of BOLD, ASL and NIRS hemodynamic response to motor stimuli in adult humans," *Neuroimage* **29**:368-382 (2006).
5. X. Cui, S. Bray, D.M. Bryant, G. H. Glover, A.L. Reiss, "A quantitative comparison of NIRS and fMRI across multiple cognitive tasks," *Neuroimage*, **54**:2808-21 (2011).
6. <http://www.neuropt.eu>.
7. D. Contini, A. Torricelli, A. Pifferi, L. Spinelli, F. Paglia, and R. Cubeddu, "Multi-channel time-resolved system for functional near infrared spectroscopy," *Opt Expr* **14**, 5418-5432 (2006).
8. D. Contini, A. Torricelli, A. Pifferi, L. Spinelli, and R. Cubeddu, "Novel method for depth-resolved brain functional imaging by time-domain NIRS," *Proc. SPIE* **6629**, 662908 (2007).
9. J.C. Ye, S. Tak, K.E. Jang, J.W. Jung, J.D. Jang, "NIRS-SPM: Statistical parametric mapping for near-infrared spectroscopy," *NeuroImage* **44**:428-447 (2009).
10. E. Visani, P. Agazzi, L. Canafoglia, F. Panzica, C. Ciano, V. Scaioli, G. Avanzini, S. Franceschetti, "Movement-related desynchronization-synchronization (ERD/ERS) in patients with Unverricht-Lundborg disease," *NeuroImage* **33**:161-168 (2006).

Resonance spatial tracking through imaging for multiplex sensing applications

K. Bougot-Robin, W.J. Wen*

Institute for Advanced Study, Hong Kong University of Science and Technology, Clear Water Bay, Kowloon, Hong Kong

Department of Physics, Hong Kong University of Science and Technology, Clear Water Bay, Kowloon, Hong Kong

*phwen@ust.hk

Abstract: Bioarray imaging techniques based on resonant waveguide gratings involve costly instrumentation for profile shift measurement. Alternative for robust and sensitive sensing is to integrate the profile dimension inside the chip and measure using simple pictures.

OCIS codes: (280.1415) Biological sensing and sensors; (310.2785) Guided wave applications;

1. Introduction

Dielectric resonant waveguide gratings allow label-free sensing based on change in resonance response induced by effective refractive index change. Applications are bulk refractive index sensing or biological sensing of species immobilized on a chip surface. Change of resonance condition might be measured through the shift of the resonant response, for instance from spectral measurement [1,2] or angular scan [3], or through the change of diffraction efficiency measured in fixed spectro-angular optical configuration [4]. While the shift in resonance response is more robust measurement as it is based on an intensity sequence instead of one point, it however relies on costly instrumentation. For spectral based measurement, sensing in a 2D array format is ensured either using a spectrometer [1] or tunable light source [2]. Angular sequences are measured by highly precise angular scan [3]. To combine simple instrumentation [4] and robust measurement based on near-resonance intensity sequence, we recently proposed a scheme based on spatial intensity sequence [5]. Instead of varying parameter through instrumentation, our scheme is based on a specially designed “Peak-Tracking Chip”. The structure of the waveguide structure is varied slowly on the chip and a resonant profile can then be measured from spatial information on a monochromatic picture.

Resonant response depends on layer thicknesses, etching depth, filling factor, layers refractive index and period. In this paper, we illustrate the case of filling factor variation. This choice allows both a choice compatible with 2D array sensing (change of pattern easier to control for a $N \times P$ disposition of identical sensing area) and a sensitivity, down to $\Delta n \sim 10^{-5}$ RIU [1,2]. In Fig. 1(A), we illustrate the spatial shift obtained for an increase in refractive index of the sensed medium of $\Delta n = 10^{-2}$. The set-up for spatial profile measurement is presented in Fig. 1(B). We call “tracks” the sensing area on the chip. The waveguide structure is varied along the long dimension of the track. It is made with a low refractive index transparent substrate (here borosilicate glass), covered by high-index guiding layer, here silicon nitride with $n \sim 2$, with thickness 0.28Λ , where Λ is the period of the grating. To ensure close from normal incidence imaging we choose a period of $\Lambda = 450$ nm. The chip is illuminated through the substrate so the incident direction of impinging wave on the grating is not changed by the sensed medium.

Due to the small dimensions of the lines and grooves, the pattern is fabricated by electron beam lithography. For fabrication issues, the pattern can be varied only discretely. From our electron-beam lithography system, the groove width can be varied by steps of 4 nm, corresponding to a filling factor variation $\Delta f = 0.0089$. The discrete structures of the tracks are called « micropads », as illustrated in Fig. 1(C). Fig. 1(D) gives details of a micropad of filling factor $f_m = d_m / \Lambda_m$, where m is the index of the micropad. For a filling factor span (0.3-0.7), it corresponds to a number of $M = 43$ units, which allows to span a refractive index range (1.3-1.5) with our present structure. In Fig. 1(E), we give the scheme of a chip with 3×2 tracks on its surface. To better fix ideas we give in Fig. 1(E) a monochromatic picture of a chip sensing media of different refractive index in parallel is given in Fig. 1 (E). Refractive index of the sensed medium is varied from 1.333 to 1.475 from left to right and up to down. A spatial shift of the micropad of maximum diffraction efficiency towards higher filling factor is observed as index increases. More details on experiments will be given later.

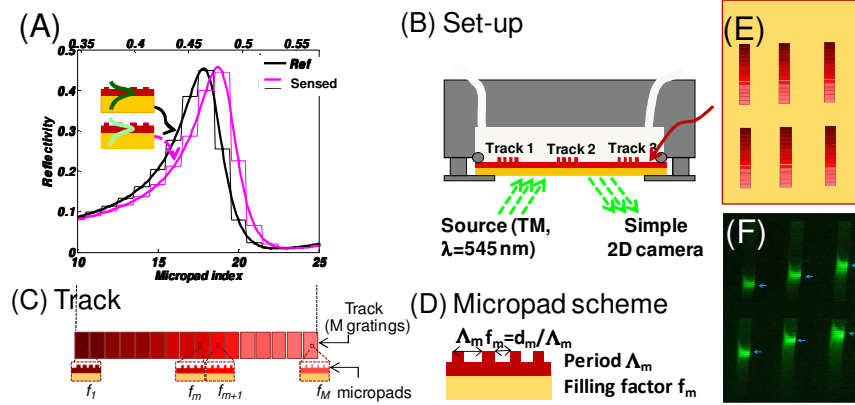


Fig. 1 : (A) Calculated spatial profile of 2 tracks, one serving as reference and the other one as sensor (B) Imaging set-up to make picture in monochromatic illumination condition (C) Scheme of a track composed of micropads with slowly varying filling factor to scan around the resonance (D) Micropad with filling factor f_m and period Λ_m . (E) Scheme of a chip of 3×2 tracks (F) Experimental picture of that chip with different refractive index corresponding to different position of the maximum of the resonance.

2. Refractive index sensing

We here present refractive index sensing both for large refractive index span from 1.333 to 1.475 by step $\Delta n=0.028$, and then for low refractive index span from 1.333 to 1.337 by step $\Delta n=10^{-3}$. We use a chip array of 2×1 tracks, where one serves as reference (for instance to correct from mechanical instabilities contributions) while on the other track, media with varying refractive index are circulated. To insure maximum stability as well as avoid thermo-optic effect, the media are circulated by using syringe pump with a flow rate of $150 \mu\text{L}/\text{min}$. We also allow the sample to reach the chamber with enough subsequent time for stabilization. Pictures are taken under an incidence $\lambda=545 \text{ nm}$, angle $\theta=18^\circ$, and in TM polarization.

To obtain solutions of different refractive index, we use water/glycerol solution with different composition. For large refractive index span, proportion of 100:0, 80:20, 60:40, 40:60, 20:80, 0:100 are chosen, thus corresponding to index varying from 1.333 to 1.475 by step of 0.028. Pictures of the tracks for different media are reported in Fig. 2(A) in grey level intensity scale together with one of the reference track picture. To determine maximum position, we use correlation analysis, which demonstrates the best accuracy for fitting with low sampling and Fano assymetric lineshapes consideration [6]. In Fig. 2(B) we give the profiles of micropads intensity for each of the tracks. Intensity values are obtained by averaging 30×20 pixels of the center of each micropad. In Fig. 2 (C), we report peak position for each of the sensed track.

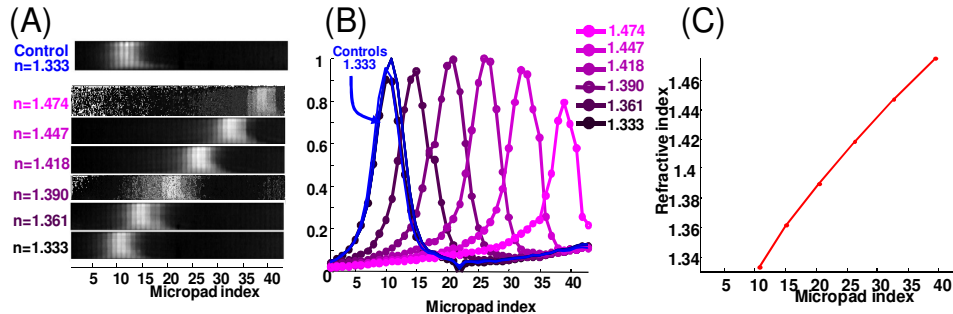


Fig. 2: (A) Track images of a control track and a track used for sensing media with refractive index between $n=1.333$ and $n=1.475$, by step of $\Delta n=0.028$ in grey level intensity scale (B) Reflectivity profiles for each of the tracks. (C) Peak position determined using correlation analysis between the reference picture and the control picture. The curve is slightly curved, in agreement with theory

For better characterization of the sensitivity, we now present results for low refractive index variation $\Delta n=10^{-3}$, with refractive index between $n=1.333$ and $n=1.337$. Pictures taken under an incident wavelength $\lambda=545 \text{ nm}$ (after slight adjustment of incident angle in comparison to previous experiment) are given in Fig. 3(A), and corresponding profiles in Fig. 3(B). The peak shift is determined by using correlation analysis. The local trend is linear and we report the maximum position as well as linear fit in Fig. 3(C). The difference between the fit and the experimental value is reported in the inset. The error in peak position correspond to a refractive index $\Delta n=2 \times 10^{-5}$. This

demonstrates good sensitivity of our technique and opens directions towards numerous applications, including bioarray imaging.

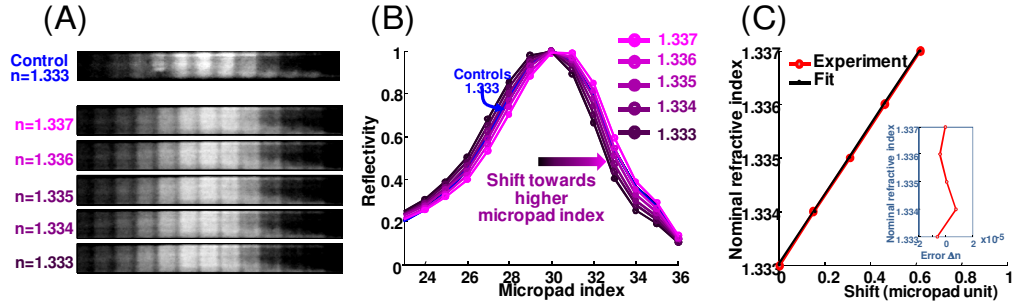


Fig. 3: (A) Track images of a control track and a track used for sensing media with refractive index between $n=1.333$ and $n=1.337$ by step $\Delta n=10^{-3}$ (B) Reflectivity level for each of the tracks. While it was not trivial to see the shift when looking at the pictures in (B), we see that profiles shift towards higher refractive index micropads as index increases (C) Peak position determined using correlation analysis. The error is reported in the inset. It is determined by first fitting the experimental data by a linear shape, and then reporting the difference between the experimental value and this fitted curve

3. Biological sensing

From refractive index experiments, we already demonstrated sensitivity of the order of $\Delta n \sim 2 \times 10^{-5}$ RIU. Induced spatial shift would be roughly the same than for a biological layer of 20 pg/mm^2 on the chip surface in aqueous solution. Therefore, our technique sensitivity is compatible with real-time hybridisation experiments.

In our previous work, we demonstrated biological application by using a single probe and different concentration of analytes. To sense different analytes in parallel, different probes might be immobilised on different tracks and we may use separate chambers to immobilise the probes as we successfully did for biological compatibility and quantitativity of the technique demonstration [5]. Taking into account tracks and picture dimensions, few tens of tracks might be measured at the same time, thus allowing good parallelism for many applications. The capability of our technique to measure real-time hybridisation was also realized experimentally.

4. Conclusion

We presented here a technique combining advantages of RWGs based sensing to simple imaging instrumentation. For robustness and sequence based measurement, we integrate the profile dimension inside the chip. Both multiplex and sensitivity aspects have been considered, demonstrating here a new method for self-reference refractive index sensing or bioarray imaging. Further aspects might be implemented with “on chip” and low sample amount advantages (temperature control, electric field application for liquid crystal dispersion studies). Spatial variability of tracks might be exploited further for instance for multispectral sensing. Our first demonstration was realised in visible, but other domain of wavelength may also be of interest. Moreover, as additional advantages in comparison to plasmon based, multipolarisation studies are also possible.

Acknowledgment

The electron beam lithography project supported by University Grants SEG_HKUST10. The project is supported by RGC grant 604710 and RPC11SC01. We are grateful to S. Li, Y. Zhang and H. Benisty for fruitful discussions.

References

- [1] K. Bougot-Robin, J.L. Reverchon, M. Fromant, L. Mugherli, P. Plateau, and H. Benisty, "2D label-free imaging of resonant grating biochips in ultraviolet," *Opt. Express* 18, 11472-11482 (2010).
- [2] A.M. Ferrie, Q. Wu, and Y. Fang "Resonant waveguide grating imager for live cell sensing" *Appl. Phys. Lett.* 97, 223704 (2010).
- [3] P. Y. Li, B. Lin, J. Gerstenmaier, and B. T. Cunningham "A new method for label-free imaging of biomolecular interactions," *Sens. Act. Chem.* 99, 6-13 (2004).
- [4] S. George, I.D. Block, S.I. Jones, P.C. Mathias, V. Chaudhery, H.Y. Wu, P.Vuttipittayamongkol, L. Vodkin, and B.T. Cunningham, "Label-free prehybridization DNA microarray imaging using photonic crystals for quantitative spot quality analysis," *Anal. Chem.* 82, 8551-8557 (2010).
- [5] K. Bougot-Robin, S. Li, Y. Zhang , I.M. Hsing, H. Benisty, W. Wen "Peak tracking chip" for label-free optical detection of bio-molecular interaction and bulk sensing," *Analyst*, 137 (20), 4785- 4794 (2012)
- [6] K. Bougot-Robin, W. Wen, H. Benisty, "Resonant waveguide sensing made robust by on-chip peak tracking through image correlation" *Opt. Exp. Biomed.* (2012).

Coherent Anti-Stokes Emission from Gold Nanorods and Its Potential for Imaging

Li Jiang^{1,2}, Iwan W. Schie¹, Jun Qian², and Thomas Huser^{1,2,*}

¹NSF center for Biophotonics Science and Technology, University of California, Davis, Sacramento, CA 95817, USA

²Centre for Optical and Electromagnetic Research, Zhejiang University, Hangzhou 310058, China

*Corresponding author: trhuser@ucdavis.edu

Abstract: Coherent anti-Stokes scattering (CAS) emitted from gold nanorods (GNRS) was studied. We proved the intensity's quadratic dependence on particle density and $\cos^6(\theta)$ dependence on beams' polarization, and the potential of CAS for nanoscale imaging.

OCIS codes: (160.4236) Nanomaterials; (180. 4315) Nonlinear microscopy; (190.4380) Nonlinear Optics, four-wave mixing

1. Preparation of immobilizing Gold nanorods on a silicon wafer

Gold nanorods used in our experiment were synthesized according to seed-mediated growth method proposed by Nikoobakht et al. at 2003 [1]. The immobilization process is shown in Fig 1 (a). Silicon wafers were firstly cleaned with acetone, ethanol and DI water. Then they were cleaned by immersion in piranha solution at 80 degree for 1h. After cooling to room temperature, they were rinsed repeatedly with DI water and then sonicated three times in fresh ethanol [2]. Then the cleaned wafers were air dried and stored in a beaker at 60 degree overnight before being immersed in an APTMS ethanol solution with volume ratio of 1:10 for 5 hours. Then the glass sample was rinsed with DI water, sonicated three times in ethanol, and dried at 120 degree for 3 hours [3]. Finally the silanized silicon wafers were subsequently immersed in the colloidal gold nanorods for several hours.

2. The relationship of CAS intensity and particle density

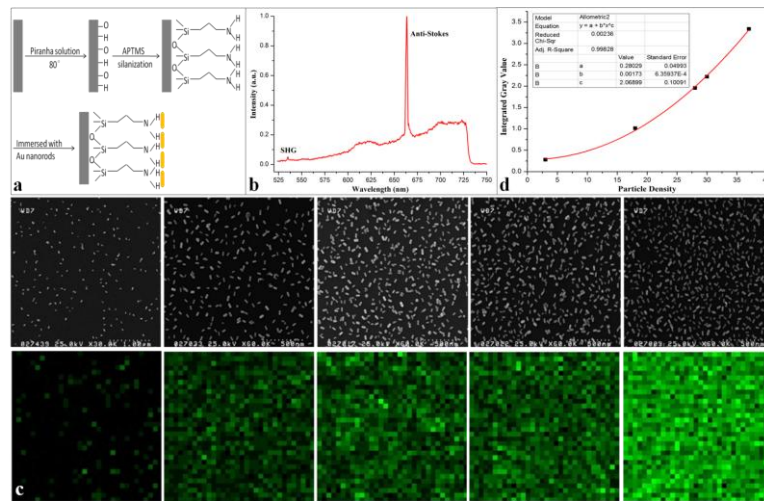


Fig. 1. (a) Illustration of the process of gold nanorods immobilization on silicon wafers, (b) nonlinear emission from gold nanorods excited by ps laser beams, (c) SEM images of five samples with different particle densities and the relative CAS images, (d) the quadratic relationship between CAS intensity and particle density.

Gold nanorods were uniformly immobilized on a silicon wafer by taking the procedure illustrated in Fig 1 (a). Then the sample was illuminated by the “pump” and “Stokes” beams simultaneously, with the average power of 8mW and 4mW respectively. The resulting emission was collected by spectrometer and showed in Fig 1 (b). To

investigate the relationship between the intensity of CAS signal and the density of gold nanorods, we prepared samples with different densities by tuning immobilization time with gold nanorods solution. Relative SEM images are showed in the upper part of Fig 1 (c).

All the samples were illuminated by both beams and the anti-Stokes signal at 663 nm was chosen as a standard scanning band to acquire CAS images with a dimension of $5\mu\text{m} \times 5\mu\text{m}$, which are showed in the lower part of Fig 1 (c). For each sample, the gray values of all the pixels were adding up by software ImageJ. The integrated gray value represented CAS intensity of that sample. The data was collected and plotted in Fig 1 (d), indicating that CAS signal is proportional to the square of particles' concentration/ density.

3. Polarization dependence

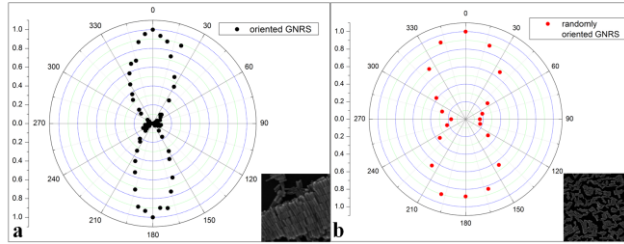


Fig. 2. Intensity (of CAS signals)-polarization patterns of (a) regularly oriented GNRS aggregations and (b) randomly oriented GNRS acquired by tuning beams' polarizations using a half-wave plate.

The polarization feature of CAS signal was also studied. In this experiment, gold nanorods solution was simply dropped on the silicon wafer and dried naturally. The structures of regularly packed gold nanorods aggregations (inset of Fig 2 (a)) and randomly oriented gold nanorods (inset of Fig 2 (b)) could be found on the edge of the dried spot and in the vicinity respectively. A half-wave plate was introduced to tune the polarization. It is distinct from Fig 2 (a) that for regularly oriented gold nanorods aggregations, the strongest CAS signal was observed when polarizations of both beams were parallel with the long axis of gold nanorods. This result confirms that the nonlinear CAS signal is aligned with the orientation of surface plasmon resonance of gold nanorods, which coincides with what H Kim *et al* found [4]. A similar Intensity-polarization pattern was seen for randomly oriented gold nanorods, as Fig 2 (b) shows. However, two manifest differences should be noticed. First of all, the pattern is much closer to a circle, which would appear if gold nanorods were evenly distributed along all the different orientations or when gold nanospheres were used as a substitute. As a result, the direction of $\theta=0^\circ$ at which the largest signal was got should be the direction that most gold nanorods were oriented in. Secondly, when the beams' polarizations were perpendicular to the direction that most gold nanorods were placed along with, this sample still emitted relatively large CAS signals.

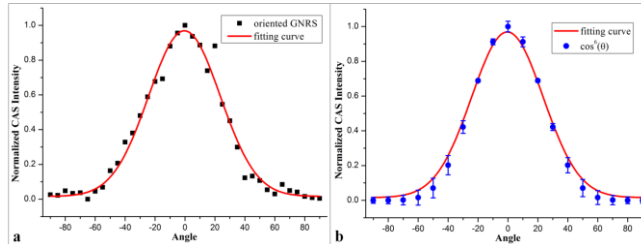


Fig. 3. (a) The data of CAS signal emitted from regularly oriented GNRS was fitted with a curve, (b) coherent anti-Stokes emission as a function of beams' polarization (denoted by θ , the angle between beams' polarization and the long axis of GNRS), which shows a $\cos^6(\theta)$ dependence.

Further investigation was carried out by fitting the data of CAS intensities emitted from the first sample (regularly oriented GNRS) with a curve (shown in Fig 3 (a)), which proves that CAS signals show a $\cos^6(\theta)$

dependence, where θ is referred to the angle between beams' polarization and the long axis of GNRS. This $\cos^6(\theta)$ dependence demonstrates that CAS signal is originating from a third-order nonlinear process, corresponding with the result of H Kim *et al* [4].

4. Imaging capability

We also verified the possibility of imaging nanoscale gold structures by CAS signals. The "pump" and "Stokes" beams were reduced to less than 3mW in all before they were focused on the sample. Pattern of the sample is shown by SEM graph (Fig 4 (a)). This pattern consisted of small aggregations, most of which were formed by single-layer densely-packed gold nanorods as Fig 4 (c) shows. ImageJ helped us analyze and find out that the number of gold nanorods constituting aggregations No.1 to No.10 ranged from a few to several hundred, and the dimension of these structures was from less than 100 nm to several micrometers.

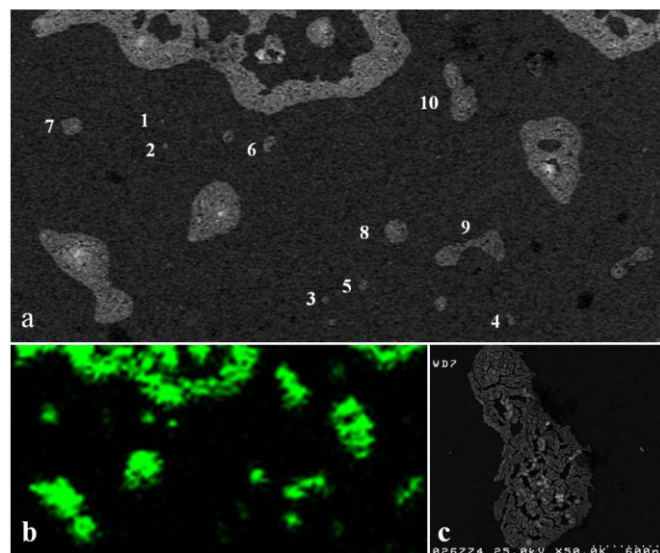


Fig. 4. (a) The SEM pattern of gold nanorods aggregated structures formed on silicon wafers, (b) corresponding CAS image, (c) the zoomed-in detail of aggregation No.10.

The resulting CAS image was recorded and shown in Fig 4 (b), from which it is clear that the coherent anti-Stokes emission of the smallest gold nanorods aggregation (aggregation No.1) can be seen. And it can be easily resolved from other structures such as aggregation No.2 simply because they are separated with a comparatively large space which is bigger than the size of focal spot. The size of the smallest structure was calculated to be around 100 nm and it only contained a few, like four to five particles.

References.

- [1] Kim H, Taggart DK, Xiang C, Penner RM, Potma EO, "Spatial control of coherent anti-Stokes emission with height-modulated gold zig-zag nanowires," *Nano Lett* **8** 2373-2377 (2008).
- [2] Nikoobakht B, El-sayed MA, "Preparation and growth mechanism of gold nanorods (NRs) using seed-mediated growth method," *Chem Mater* **15** 1957-1962 (2003).
- [3] Chen C-D, Cheng S-F, Chau L-K, Wang CRC, "Sensing capability of the localized surface plasmon resonance of gold nanorods," *Biosens Bioelectron* **22** 926-932 (2007).
- [4] Nath N, Chikoti A, "A colorimetric gold nanoparticle sensor to interrogate biomolecular interactions in real time on a surface," *Anal Chem* **74** 504-509 (2002).

Postdeadline Session II

Friday, 9 November

15:30 - 17:15

Begonia Room

Postdeadline Submissions from
Subcommittees 3 and 4

50-GHz-spaced, 8x499-Gb/s WDM Transmission over 720-km SSMF using per-channel 41.6-GBd PDM-64QAM

Wei-Ren Peng, Hidenori Takahashi, Takehiro Tsuritani, and Itsuro Morita

KDDI R&D Laboratories Inc., 2-1-15 Ohara, Fujimino, Saitama 356-8502, Japan,
Phone: +81-49-278-7853, Fax: +81-49-278-7853, Email: pe-weiren@kddilabs.jp

Abstract: We demonstrate the world's first single-carrier-based, 400-Gb/s-class and 50-GHz-spaced WDM system using 41.6-GBd PDM-64QAM per channel. Eight channels are successfully transmitted over 720-km SSMF with hybrid Raman and EDF amplification.

1. Introduction

400 Gb/s per channel, expected to be the next generation Ethernet line-rate standard, has motivated lots of researches on 400-Gb/s-class wavelength division multiplexing (WDM) transmissions [1-6]. With the consideration of currently commercialized 50-GHz grid, it would be highly appreciable if the developed 400-Gb/s channels could be arranged with 50-GHz channel spacing. Thus, there have been many demonstrations on 50-GHz-spaced, 400-Gb/s WDM transmission achieving a net spectral efficiency (SE) of ~8.0 bit/s/Hz [3-6]. However, all these demonstrations have relied on the use of multiple low-capacity subcarriers to synthesize the desired 400 Gb/s, which would force the transmitter and receiver to take parallel processing scheme, for which laser and modulator arrays are needed at the transmitter, and photodiode and digital signal processing (DSP) arrays are required at the receiver as well, thus keeping the transceiver high in both the cost and complexity. Therefore, it would be quite advantageous if these 400-Gb/s channels could be produced using simpler single-carrier scheme and, at the same time, could be arranged with 50-GHz channel spacing.

Recently, we have demonstrated the digital-to-analog-converter-free (DAC-free) generation and 1200-km transmission of a single-carrier-based 497-Gb/s signal using 41.4-GBd PDM-64QAM [7]. In that paper we've mentioned this signal might be a suitable candidate for 50-GHz-spaced 400-Gb/s WDM systems. However, such a high symbol rate, greater than (0.8 x channel spacing), would lead to an unpredictable penalty from both the strong filtering and linear crosstalk when implemented in a 50-GHz-spaced WDM system. Thus, its feasibility in a 50-GHz-spaced WDM system has yet to be confirmed. In fact, there has been no experimental evidence showing that 50-GHz-spaced 400-Gb/s WDM system could be carried out using single carrier per channel.

In this paper, using our developed 41.6-GBd (499 Gb/s, and ~400 Gb/s without overheads) PDM-64QAM as per channel, we successfully demonstrate the first 50-GHz-spaced 400-Gb/s WDM system based on single-carrier scheme. We transmit eight channels over 720-km standard single mode fiber (SSMF) with hybrid Raman/Erbium-doped-fiber (EDF) amplification and obtain bit error rates (BERs) of all channels lower than 2.4e-2, the 20% soft-decision FEC threshold [8]. These results are achieved by optical pre-shaping for equalizing spectrally the signal power [7], and also the long-tap filtering (LTf) for reflection compensation [7, 10].

2. Experimental setup and offline processing

Figure 1 depicts the experimental setup. At the transmitter, eight external cavity lasers (ECLs, linewidth < 100 kHz), running from 192.65 to 193.00 THz with channel spacing of 50 GHz, are used as the WDM light sources. The outputs from the odd-channel lasers are combined with an optical 4x1 coupler and modulated into 64QAM signals with our 64QAM generator (64QAM Gen.). This 64QAM generator, as illustrated in Fig. 2, utilizes one in-

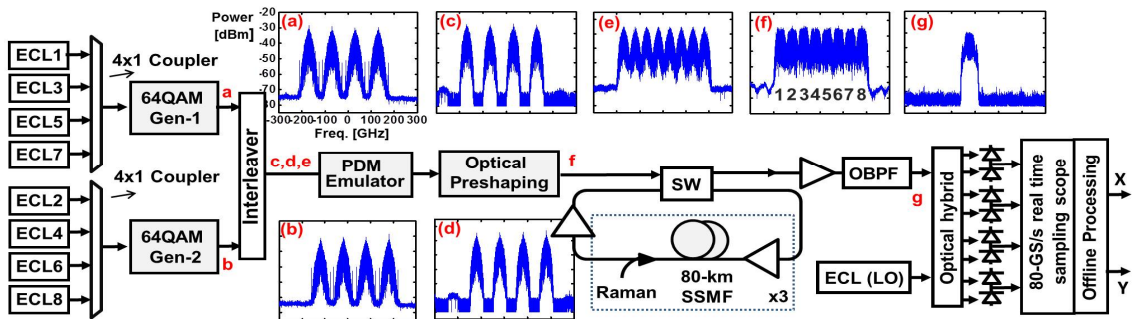


Fig. 1 Experimental setup for DAC-free generation and 720-km WDM transmission of 41.6-GBd PDM-64QAM.

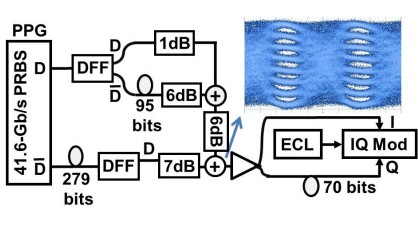


Fig. 2 Details of “64QAM Gen” module in Fig. 1. The inset shows the 41.6-GBd eight-level drive signal.

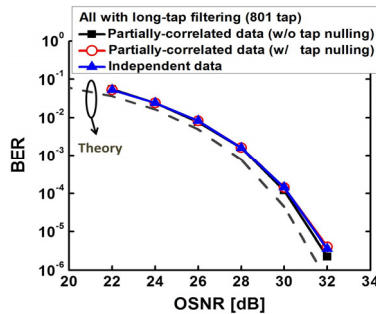


Fig. 3 Numerical results with experimental data pattern (partially-correlated data) and with independent data pattern, all with 801-tap filter.

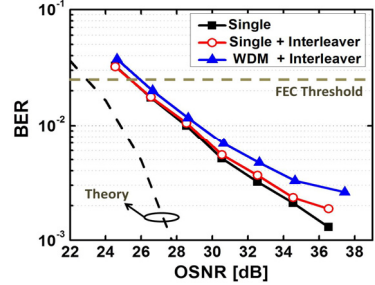


Fig. 4 Experimental BER versus OSNR (0.1 nm noise bandwidth).

phase/quadrature (I/Q) modulator with ~26-GHz 3-dB bandwidth and V_{π} of 2.2V. The required eight-level electrical signals at the I and Q branches of the modulator are synthesized by three pseudo random binary sequences (PRBSs) of length $2^{15}-1$ which are three of the four outputs from two D-type flip-flops fed respectively with 41.6-Gb/s data and its delayed inversion out of a pulse pattern generator (PPG). The applied attenuations and delays for each binary sequence are depicted in the figure (each addition is implemented with one passive combiner which has ~6-dB loss) and the eye pattern of the synthesized 41.6-GBd eight-level signal can be found in the inset. An electrical linear amplifier is followed to boost its peak-to-peak amplitude to ~2.2V. The amplified signal is then split, delayed by 70 symbols, and fed to I and Q branches of the optical I/Q modulator, resulting in 41.6-GBd 64QAM. After 64QAM modulation, the odd-channel optical spectrum can be found in Fig. 1(a). The even-channel 64QAMs are obtained in a similar way and its spectrum is shown in Fig. 1(b). Note that the second 64QAM generator comprises similar components as the first one and during experiment the two individual PPGs are running independently so that their output patterns for odd and even channels should be pseudo-uncorrelated. After 64QAM generators, the odd and even channels are combined through a 50:100GHz wavelength interleaver, of which the output spectrum is shown in Fig. 1(e). We also depict the spectra of only odd and only even channels in Fig. 1(c) and 1(d) to illustrate the interleaver’s filtering effects. A followed PDM emulator, which splits equally the input signal, delaying one copy by 1051 symbols, and recombines it at the output, is used to emulate the target per-channel 41.6-GBd PDM-64QAM (499 Gb/s). After accounting for 20% FEC and ~4% Ethernet overheads, the net data rate would be ~400 Gb/s. Due to the limited bandwidth of the optical modulator, an optical filter which performs preshaping for each channel is applied to pre-emphasis the signal power at high frequencies, after which the signal spectra is shown in Fig. 1(f). The signal is then sent into the fiber recirculating loop which consists of three spans of 80-km SSMF (average span loss \approx 16 dB) with hybrid Raman (backward) and EDF amplification. The average on-off Raman gain is ~12 dB in each span.

At the receiver, an optical amplifier is used to enhance the signal power and a followed optical band-pass filter (OBPF) with ~45-GHz 3-dB bandwidth is applied to select the desired channel and remove the out-of-band noise. The filtered signal’s spectrum can be found in Fig. 1(g). The filtered signal is then detected by a polarization-diversity intradyne receiver, which includes an optical hybrid and four balanced photodiodes. The local oscillator (LO) is performed by another ECL with <100-kHz linewidth and its central wavelength is tuned to the desired channel wavelength for semi-homodyne detection. The four outputs from the balanced photodiodes, the real and imaginary parts of both polarizations, are recorded by two cooperated 32-GHz, 80-GS/s real-time sampling scopes. The stored data with a length of 2-million sampling points are processed offline in a desktop computer.

The offline processing is described in detail as follows: i) deskew and orthogonalization. ii) Digital filtering with $(0.52/T)$ 3-dB bandwidth, where T is the symbol duration. iii) Resampling with two samples per symbol. iv) Frequency-domain chromatic dispersion compensation. v) Clock recovery. vi) Polarization-dependent (2x2), 31-tap, $T/2$ -spaced adaptive butterfly finite impulse response filter (FIR) with constant modulus algorithm (CMA) for pre-convergence followed by radius-directed algorithm (RDA) for steady-state operation. vii) Polarization-independent carrier recovery using block-based blind phase search (BPS) method with a block size of ~40 [9]. viii) Two sets of polarization-independent, 801-tap, T -spaced FIR filter with least-mean-square (LMS) algorithm [7, 10]. The purpose of the long-tap filters is to mitigate electrical reflections [10] caused by impedance mismatches between electrical components at the transmitter. (In fact, reflections can be even observed by directly linking a PPG to a scope. These reflections are found to do limited harm to the low-QAM signals, such as QPSK; however, its impact will become

larger for 64QAM in which the symbol spacing is much reduced [10]). Since at the transmitter each 64QAM symbol is synthesized by six same binary inputs with relative delays, symbols with those delays might be partially-correlated. For this we deliberately null those taps (tap nulling), and also its neighboring four, to avoid using those partially-correlated symbols for equalization. Note that the two polarizations are de-correlated by 1051 symbols and thus they can still be assumed independent even with the use of 801-tap LTF. ix) Decision and BER evaluation. BER is obtained with direct error counting method.

3. Results and discussions

Firstly we numerically illustrate the appropriate use of the LTF in Fig. 3. “Partially-correlated data” utilizes the same data pattern as our transmitter and “tap nulling” means the tap coefficients of LTF are nulled at positions matching to those partially-correlated symbols (see Section 2). “Independent data” utilizes random data pattern of which no correlated symbol would appear within the equalization range of the LTF. For all cases the LTF is always used. We’ve found that, when using the LTF, performances of partially-correlated and independent data are very similar and no unfair gain from the partially-correlated symbols has been found. Therefore, we would apply LTF for reflection compensation throughout this paper.

For the following results, optical preshaping (~2.4-dB gain at BER = 2.4e-2) and LTF with tap nulling (~0.8-dB gain at BER = 2.4e-2) are always applied throughout this paper. Their benefits have been discussed in our previous publication [7, 10] and thus are omitted here.

Shown in Fig. 4 is the measured optical signal to noise ratio (OSNR, 0.1-nm noise bandwidth) tolerance in back-to-back for which we consider the following three cases: 1) single channel without interleaver, 2) single channel with interleaver, and 3) WDM with interleaver. The required OSNR at the 20% soft-decision FEC threshold (BER = 2.4e-2, [8]) are 25.4, 25.4 and 26 dB, respectively. Interestingly, the interleaver’s filtering effect is found to be almost negligible due to the use of flat-top interleaver while ~0.6-dB penalty is found from WDM linear crosstalk.

In Fig. 5, we measure the BER as a function of per-channel launch power for 4th channel after 720-km transmission, where the channel index is given in Fig. 1(f). We’ve found that about -3 dBm/ch can yield the best performance and thus used it for the following measurements.

In Fig. 6 we investigate BER as a function of distance for the 4th channel, and in Fig. 7 we show BERs of all channels after 720-km transmission. All channels can yield BERs lower than the FEC threshold (2.4e-2) [8]. The recovered constellations for the X- and Y- polarizations of the 4th channel are shown in the insets. We find that the noise statistics can be well approximated by a normal distribution and thus confirm the appropriate use of the soft-decision FEC.

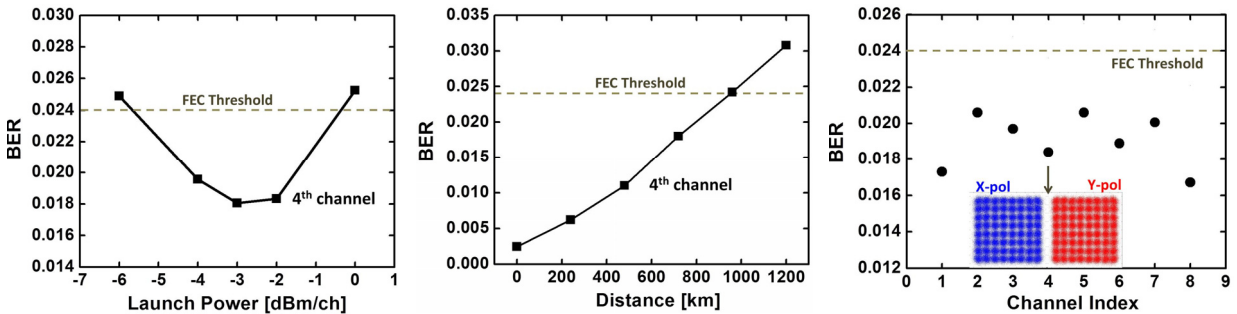


Fig. 5 Experimental BER versus per-channel launch power for the 4th channel. Channel index is given in Fig. 1(f).

Fig. 6 Experimental BER versus distance for the 4th channel.

Fig. 7 Experimental BERs of all channels after 720-km transmission. Channel index is given in Fig. 1(f).

4. Conclusions

We’ve demonstrated the world’s first single-carrier-based, 50-GHz-spaced 400-Gb/s WDM system using 41.6-GBd PDM-64QAM per channel. Eight-channel transmission over 720-km SSMF is achieved with 20% FEC overhead.

(This work was partly supported by NICT, Japan)

References

- [1] Y.-K. Huang et al., OECC’10, PD3.
- [2] V.A.J.M Sleijfer et al., OFC’12, W4C3.
- [3] H. Takahashi et al., ECOC’10, Tu3C1.
- [4] A. Sano et al., OFC’12, PDP5C3.
- [5] X. Zhou et al., ECOC’11, We8B2.
- [6] X. Zhou et al., OFC’12, PDP5C6.
- [7] W.-R. Peng et al., OECC’12, PDP1-3.
- [8] D. Chang et al., OFC’11, TuN2.
- [9] T. Pfau et al., JLT, pp. 989, 2009.
- [10] W.-R. Peng et al, “On the long-tap filtering gain in optical high-order QAM transmission systems,” submitted to OFC’13.

Real-time Transoceanic Transmission of 1-Tb/s Nyquist Superchannel at 2.86-b/s/Hz Spectral Efficiency

Yue-Kai Huang¹, Eduardo Mateo², Masaki Sato³, Dayou Qian¹, Fatih Yaman¹, Takanori Inoue², Yoshihisa Inada², Shaoliang Zhang¹, Yoshiaki Aono³, Tsutomu Tajima³, Takaaki Ogata², and Yasuhiro Aoki²

¹NEC Laboratories America, Inc., Princeton, NJ 08540, USA

²Submarine Network Division, NEC Corporation, 34-6, Shiba 5-chome, Minato-ku, Tokyo 108-0014, Japan

³Converged Network Division, NEC Corporation, Abiko, Japan

kai@nec-labs.com

Abstract: Real-time 1-Tb/s superchannel transmission over 5,400-km using 100-GbE based subcarriers was achieved with an optical bandwidth of 350-GHz. The distance was further extended to 7,200-km by using digital Nyquist-shaped subcarriers with 1-dB margin.

OCIS codes: (060.2330) Fiber optics communications; (060.2360) Fiber optics links and subsystems.

1. Introduction

As 100-Gb/s systems are being commercially deployed, new technologies enabling beyond 100-Gb/s transmission are generating tremendous interests nowadays [1-5]. Dual-polarization (DP) 16-ary quadrature-amplitude modulation (16QAM) is one of the potential candidates for its high spectral efficiency (SE) [1-2]. However, the large constellation size of DP-16QAM requires significantly higher optical signal-to-noise ratio (OSNR) which reduces the tolerance to fiber nonlinearity and laser phase noise. Therefore, for ultra-long haul transmission based on commercially available fibers and cost-effective repeater spacing, DP quadrature phase shift keying (QPSK) is still a superior format [3-5]. Optical multi-carrier (MC) superchannel is also a promising technology for realizing line-rates beyond 100-Gb/s, either by modulating individual lasers in parallel to achieve typical SE of DWDM systems [3], or by tightly packing subcarriers using phase-locked optical tones to increase SE [4-5]. Newly, software defined pulse shaping technologies, either implemented in the optical or digital domain, can be applied to confine the subcarrier signal energy and reduce subcarrier spacing without inter-carrier interference (ICI). Optical superchannel can be designed using software-defined optics (SDO) to improve transmission performance and network flexibility, and it has been shown that distance adaptive transmission can be achieved by tuning the channel S.E. through either modulation format or carrier spacing [5-6].

In this work, for the first time, we demonstrated 1-Tb/s superchannel transmission over 5,400km uncompensated link using ten parallel real-time 127-Gb/s subcarriers. The use of 127-Gb/s subcarriers has the advantage of streamlining system integration by retaining 100-GbE client interfaces and optical transport unit (OTU) framing. By using Nyquist shaping technology in the optical domain, the subcarrier spacing could be reduced to 35-GHz, and the 1-Tb/s superchannel occupies only a bandwidth of 350-GHz. To the best of our knowledge, this is the largest SE (2.86 b/s/Hz) achieved in ultra-long haul transmission systems based on real-time 127-Gb/s subcarriers. To further extend transmission reach, superchannel pulse-shaping was implemented in the digital domain by means of high-speed digital-to-analog converters (DAC). The reach of the 1-Tb/s superchannel could be extended to 7,200km with 1-dB system margin thanks to the reduced ICI provided by digital Nyquist shaping. A hybrid superchannel scheme is also demonstrated in this paper by mixing subcarriers with different Nyquist shaping techniques.

2. System Design and Setup

Fig. 1 shows the experimental setup for the real-time 1-Tb/s superchannel transmission. First, ten 127-Gb/s optical subcarriers are generated using an array of ten “flexible grid 100-GbE transceivers” implemented in a super-transponder prototype system. In this prototype, the client interface module (CFP) is based on 100-GbE but the super-transponder concept could also adopt future client interfaces such as 400GbE or 1TbE. Each subcarrier includes a OTU4 framer, forward error correction (FEC) block, and optical internetworking forum 100GLH-EM compliant DP-QPSK digital coherent transceiver module. The transceiver module consists of a DP-QPSK modulator, a polarization and phase diversity coherent optical receiver, and digital coherent signal processing large scale integrated (DSP-LSI) chip [7], which incorporates results from the “R&D on High Speed Optical Transport System Technologies” project supported by the Ministry of Internal Affairs and Communications of Japan [8].

We tightly packed the output of ten flexible grid 100-GbE transceivers using a combination of passive couplers and a two-input-port software-defined optical filter. Ten real-time 127-Gb/s subcarriers carrying independent data streams were spaced at 35-GHz. Optical Nyquist shaping was applied to each subcarrier by the software-defined optical filter using an optimized pre-defined profile with the maximum transmittance at the edge of each subcarrier. Even though the subcarrier spacing is fixed at 35 GHz in this experiment, the use of “flexible grid 100-GbE transceivers” and software defined optical filter can accommodate arbitrary spacing through SDO design. With each

subcarrier running at 31.75-GHz baud-rate, the 1-Tb/s superchannel is ~10% above Nyquist rate, occupying only a bandwidth of 350-GHz. The resulted 2.86-b/s/Hz SE is 43% higher than 100-Gb/s systems with 50-GHz spacing.

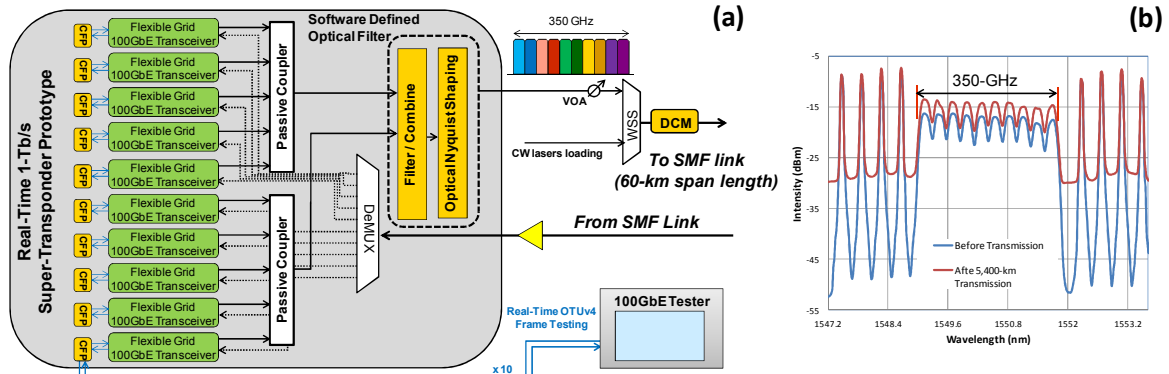


Fig. 1. (a) Experimental setup for 1-Tb/s real-time superchannel; (b) Spectrum (0.1-nm resolution) with the CW loading lasers.

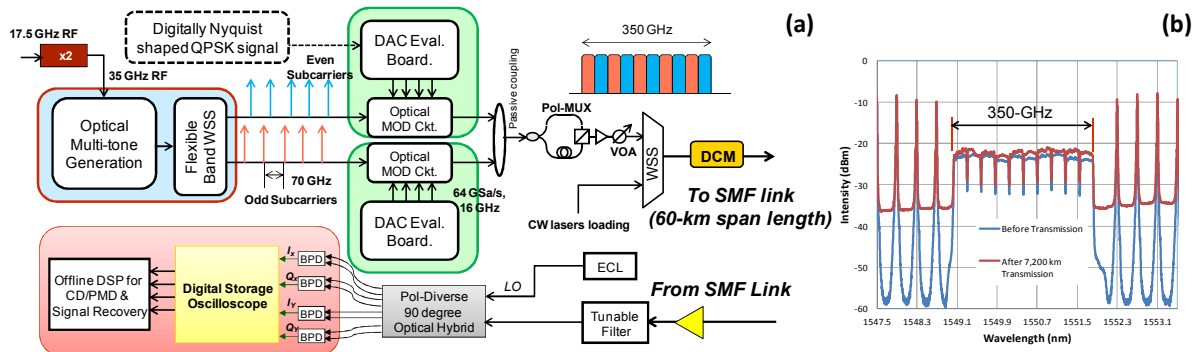


Fig. 2. (a) Setup for the 1-Tb/s superchannel with electrical Nyquist subcarriers; (b) Spectrum (0.01-nm resolution) with the CW loading lasers.

The fiber link test-bed consists of multiple spans of 60-km single mode fiber (SMF) with erbium-doped fiber amplifiers (EDFAs) to compensate the span loss. The 1-Tb/s superchannel is combined with multiple continuous wave (CW) lasers, as shown in Fig. 1(b), using a wavelength selective switch (WSS) and a variable optical attenuator (VOA) to optimize the launch power of the superchannel before transmission. A dispersion compensation module (DCM) that consisted of multiple cascaded fiber Bragg gratings (FBGs) was used for partial pre-compensation of link's chromatic dispersion (CD). At the receiver, passive optical splitters and tunable optical filters are used to route each subcarrier to its designated “flexible grid 100-GbE transceiver” for real-time pre-FEC and post-FEC bit error rate (BER) counting using a built-in BERT function. The residual link CD and polarization mode dispersion (PMD) are entirely compensated by the DSP LSI. The client side BERs at OTU-4 level for each subcarrier can be measured one at a time through the CFP using a 100G Ethernet analyzer.

For performance comparison, a 350-GHz bandwidth 1-Tb/s superchannel is also generated by aggregating 10 DP-QPSK subcarriers with electrical Nyquist pulse shaping, as shown in Fig. 2(a). The phase-locked 35-GHz spaced optical combs are created by wide-band phase modulating a 100-kHz line-width external cavity laser (ECL) at 193.35 THz. A flexible-band WSS is used to filter and equalize the ten optical carriers before splitting them into odd and even groups. The two groups are separately modulated with de-correlated QPSK signals, where the 32G baud-rate Nyquist-pulse-shaped symbols are generated using a PRBS $2^{15}-1$ sequence and outputted from a high-speed DAC with 65-GS/s sampling rate, before they are passively combined. Polarization multiplexing is performed by splitting the signal, delaying one copy with de-correlation of 100 symbols, and rotating it to the orthogonal polarization before polarization recombining. At the receiver, the signal is filtered by a 0.4nm optical tunable filter (OTF) and downconverted into baseband in a polarization-diversity coherent receiver. The output signals are sampled and digitized by real-time oscilloscopes with 50-GS/s sampling rate and 18-GHz bandwidth. The data is processed using similar offline DSP as in [4]. For BER computation, 20 data sets of 2- μ s duration corresponding to more than 4×10^6 bits per subcarrier were captured and processed.

3. Results and Discussions

Fig. 3(a) plots the back-to-back (BTB) BER vs. OSNR curve for different schemes. First, a curve for single carrier 100-Gb/s is measured in real-time with 50-GHz rectangular filter profile applied. We then measured the curve for multi-carrier operation at 35-GHz spacing and a 2.5-db OSNR penalty is immediately observed at $BER = 1 \times 10^{-2}$

due to sharp filtering and ICI. By optimizing the optical Nyquist shaping, the penalty is reduced to 1.5 dB. Switching to electrical Nyquist shaping provided 1 dB sensitivity improvement for single channel operation, but more importantly it essentially eliminated ICI thanks to the rectangular spectral profile allowing the multicarrier operation to have the same receiver sensitivity as the single channel.

Fig. 3(b) shows the 1-Tb/s superchannel performance by plotting the Q-factor (calculated from BER) against signal launch power. After 5,400-km transmission, the optimal launch power for 127-Gb/s optical Nyquist subcarrier is around -2 dBm with 8.3-dB Q-factor. The pre-FEC BERs of all ten 127-Gb/s subcarriers are measured and plotted in Fig. 3(b). All subcarriers achieved error free condition after soft-decision (SD) FEC and their corresponding client-side data at the OTU-4 level are also confirmed to be error-free in real time. Due to its superior BTB performance, the electrical Nyquist superchannel can have longer reach and the optimal power after 7,200-km is ~ -3.5 dBm with 8.7-dB Q-factor. All ten subcarriers achieved 1.5-dB margin below the SD-FEC limit.

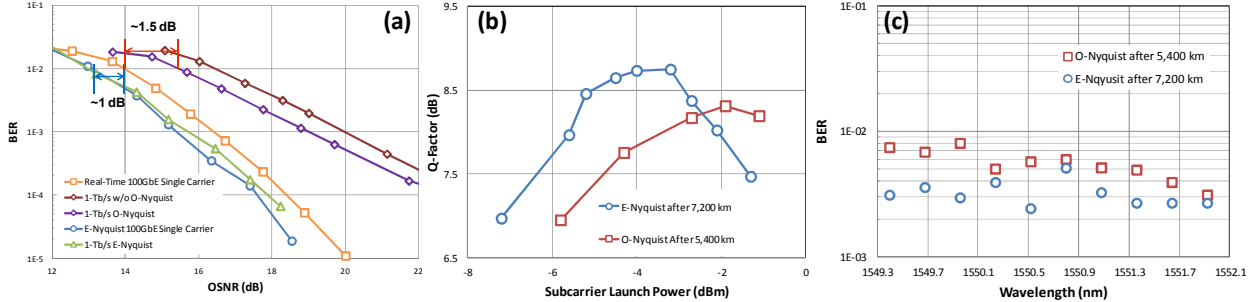


Fig. 3. (a) BTB BER vs. OSNR curves; (b) Q-factors vs. subcarrier launch power and (c) BER sweep for different Nyquist shaping techniques.

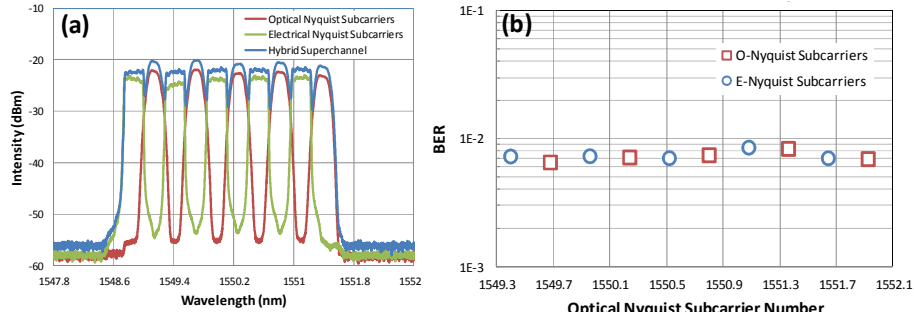


Fig. 4. 1T superchannel transmission using hybrid subcarriers: (a) captured optical spectrum; (b) BER sweep for after 7,200-km transmission.

We also designed a hybrid 1-Tb/s superchannel consisted of a real-time super transponder with five optical Nyquist-shaped subcarriers and five electrical Nyquist-shaped subcarriers, formed by passively combining the even subcarriers in Fig. 2(a) with five 70-GHz spaced 127-Gb/s real-time subcarriers in Fig. 1(a). In this case, the performance of optical (electrical) Nyquist subcarriers increased (decreased) due to the drop (rise) of ICI from immediate neighbors, as shown in Fig. 4(a). The reach of optical Nyquist subcarriers was extended to 7,200 km. The pre-FEC BERs of all ten subcarriers are plotted in Fig. 3(b), achieving >1-dB margin. Real-time error-free operation for the five optical Nyquist subcarriers is also confirmed. This hybrid superchannel scheme could be implemented through SDO and useful in upgrade scenarios where network operators can combine two transmitter technologies to achieve evenly-spread performances.

4. Conclusion

Real-time transmission of 1-Tb/s superchannel was demonstrated over 350-GHz optical bandwidth using parallel 127-Gb/s subcarriers by optical Nyquist shaping. The achieved 2.86-b/s/Hz SE is 43% higher than current 100-GbE WDM systems. The superchannel was successfully transmitted over 5,400-km of SMF, confirming true bit error free operation in real-time. To the best of our knowledge, this is the longest transmission distance and highest SE for 1-Tb/s systems based on real-time 100-GbE operation. Finally, by modifying the superchannel composition to alternating digitally- and optically-shaped subcarriers, an operation suitable for SDO implementation to meet upgrade demands, system reach could be further extended to 7,200 km with > 1 dB margin.

5. References

- [1] F. Buchali, et. al., *OFCC/NFOEC 2012*, OWC4C, Mar. 2012.
- [2] J. Li, et. al., *ECOC 2012*, Th.2.C.1, Sep. 2012.
- [3] J. Rahn, et. al., *OFCC/NFOEC 2012*, PDP5D.5, March 2012.
- [4] T.J. Xia, et. al., *OFCC/NFOEC 2011*, PDDA3, Mar. 2011.
- [5] Y.-K. Huang, et. al., *OFCC/NFOEC 2012*, OM3H.4, Mar. 2012.
- [6] T. J. Xia, et. al., *OECC 2012*, 5A2-3, Jul. 2012.
- [7] <http://www.ntt-electronics.com/en/products/electronics/100GDSPLSI.html>
- [8] E. Yamazaki, et. al., *Opt. Exp.*, 19(14), pp. 13179, Jul. 2011.

168×103 Gb/s 25-GHz-Spaced C-band Transmission over 2240 km SSMF with Improved Nonlinearity Using DFT-S OFDM-8PSK Modulation

Qi Yang, Xiao Xiao, Chao Li, Ming Luo, Zhixue He, Cai Li, Rong Hu, Xu Zhang, Shaohua Yu

State Key Laboratory of Optical Communication Technologies and Networks, Wuhan Hubei 430074, China

qyang@wri.com.cn

Abstract: With nonlinearity improvement using DFT-S OFDM-8PSK modulation, we have successfully demonstrated a transmission of 168×103 Gb/s C-band optical PDM-OFDM signals over 2240 km SSMF with 25 GHz channel spacing.

OCIS codes: (060.1660) Coherent communications; (060.2330) Fiber optics communication

1. Introduction

In recent years, coherent optical orthogonal frequency division multiplexing (CO-OFDM) has drawn great attention due to its high spectral efficiency, dispersion resilience, and flexibility in frequency multiplexing [1]. The researches and applications have been extensively carried out in large capacity / long haul transmission and next generation dynamic optical networks [2-4]. In [5], a long haul transmission of a 448-Gb/s reduced-guard-interval CO-OFDM over 2000 km ultra-large-area fiber has been demonstrated. Recently, 101.7 Tb/s transmission over 3×55 km standard single mode fiber (SSMF) applying PDM-128QAM CO-OFDM in C- and L-bands was reported [6]. However, the high peak-to-average power ratio (PAPR) in conventional CO-OFDM causes excessive nonlinearity effect in fiber link, which constraints the transmission reach dramatically. Thus, fiber nonlinearity mitigation in CO-OFDM system becomes an important research topic [7-9]. Discrete Fourier transform (DFT) spread OFDM is an efficient technique to reduce the PAPR for CO-OFDM transmission systems, which improves the overall transmission nonlinearity performance [10-12]. In [12], a transmission demonstration of 440.8-Gb/s DFT-S OFDM signal shows ~ 1 dB nonlinearity improvement compared to the conventional OFDM.

DFT-S OFDM with M-ary PSK modulation can improve the PAPR more significantly than M-ray QAM modulation due to constant transmitted signal power [13]. In this paper, we choose 8PSK as the main modulation format to achieve both high spectral efficiency and good tolerance to nonlinear phase noise. With the additional nonlinearity improvement introduced by DFT spread and distributed Raman amplification, we successfully demonstrate a 168×103 Gb/s coherent optical DFT-S OFDM-8PSK C-band transmission over 2240 km SSMF with ITU-T standardized 25 GHz channel spacing [14]. When applying 20.5% soft-decision forward error correction (FEC) technique, the bit error ratio (BER) measured for all the sub-channels after transmission is under the error threshold of 2×10^{-2} .

2. Experimental setup

Fig. 1 shows the experimental setup for the 168×103 Gb/s DFT-S OFDM-8PSK transmission system. To emulate 25 GHz C-band carrier sources at the transmitter, eight tunable laser sources are first divided into odd/even pairs, and then fed into the phase modulator (PM) based multi-carrier generators. The PMs are driven with strong RF sine waves (~ 1.5 W) at frequency of 25 GHz. Each laser can generate up to 21 optical carriers. In this fashion, these eight lasers can totally provide $21 \times 8 = 168$ optical carriers. One programmable wavelength selective switch (WSS, Finisar 4000S) is used to combine the PM outputs, which simultaneously performs the function of spectral reshaping and flattening, as shown in Fig. 1(a). The right inserted figure shows the generated multi-carriers in 7th Channel. Note that for each measurement at the interest wavelength, the corresponded optical carrier is suppressed and replaced with an individual ECL. The transmitted signal is generated off-line by MATLAB program with a data sequence of $2^{31}-1$ pseudo-random binary sequence (PRBS) and mapped onto 8PSK constellation. An arbitrary waveform generator (AWG) is used to produce RF signal at 12 GS/s. Then all optical carriers are simultaneously modulated by an optical I/Q modulator. It is worthy to point out that all the modulated sub-bands are correlated. Un-correlated configuration for neighboring bands will further improve the transmission performance [8]. Another optical intensity modulator (IM) driven by a 6.09375 GHz sine wave is used to further duplicate the signal to three copies. The bandwidth of transmitted RF signal for each sub-band is 18.28125 GHz, which is less than the channel spacing (~ 25 GHz). The modulated optical spectrum is shown in Fig. 1(b). For each sub-band, the payload mapped with 8PSK constellation is partitioned to two sets. Each set is comprised of 64 subcarriers. 2 out of total subcarriers are

used to estimate the phase noise. 64-point DFT spreading is first employed by the two sets. When mapping the signal onto frequency domain, the middle 2 subcarriers are unfilled to avoid contamination from DC. By padding zeros on the higher frequency part, another 256-point IFFT is used to convert the frequency domain signal to time domain. 1/32 of the symbol period is used as the cyclic prefix to compensate the channel dispersion. The optical OFDM signal is then fed into a polarization splitter, with one branch delayed by one OFDM symbol period to emulate the polarization-multiplexing, resulting in a total data rate of 34.36 Gb/s per sub-band. Thus, the data rate for each channel is $3 \times 34.36 \text{ Gb/s} = 103 \text{ Gb/s}$. The spectral efficiency within each channel is 5.64 bit/s/Hz. The transmission link is constructed by a fiber recirculation loop, which contains four spans of 80 km SSMF with Raman amplifiers only. At the receiver side, an ECL (linewidth of $\sim 100 \text{ kHz}$) is utilized as the optical local oscillator (LO) and coupled into a polarization-diversity coherent receiver to mix with the signal. The signal is detected by a typical coherent receiver. The four RF signals for the two IQ components are then fed into a Tektronix oscillator scope and are acquired at 50 GS/s and then processed off-line. The recovered 8PSK constellations in both polarizations are also shown in the left inserted figures.

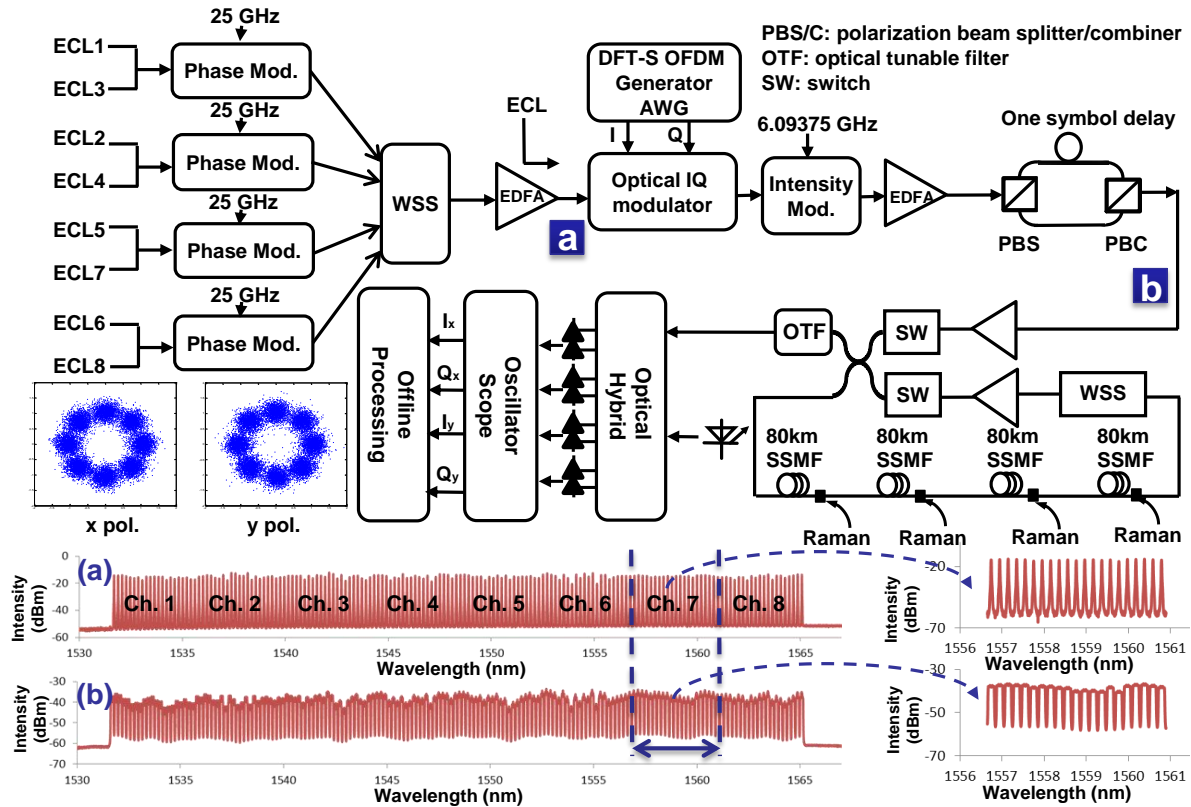


Fig. 1 Experimental setup for 168x103 Gb/s DFT-S OFDM-8PSK transmission: (a) 168 carriers generated by the first optical phase modulator; (b) optical spectrum for 168x103 Gb/s DFT-S OFDM-8PSK signal. Right inserted figures shows the carriers and modulated signal in 7th channel.

3. Experimental results and discussion

We first conduct a BER versus OSNR performance measurement for a 103 Gb/s (before FEC) CO-OFDM signal in a back-to-back configuration for OFDM-8PSK, OFDM-8QAM and DFT-S OFDM-8PSK, which is shown in Fig. 2. The performance of conventional OFDM-8PSK and DFT-S OFDM-8PSK are very close (OSNR=18.5 dB for $\text{BER}=10^{-3}$), while OFDM-8QAM slightly outperforms ($\sim 1 \text{ dB}$) the two 8PSK schemes [15]. To investigate the nonlinearity performance of the three schemes, we then measured the BER as a function of the launch power after 2240 km SSMF transmission (in Fig. 3). For the launch power less than -3.2 dBm, with the help of the reduced PAPR, DFT-S OFDM-8PSK outperforms OFDM-8PSK, but OFDM-8QAM still shows better performance than DFT-S OFDM-8PSK in this power region. When further increasing the launch power, the nonlinearity effect limits the best BER performance of OFDM-8QAM $\sim 1 \times 10^{-3}$ (optimum launch power of 0.2 dBm). However, the optimum launch power of DFT-S OFDM-8PSK can further reach 1.4 dBm with BER of 5.17×10^{-4} . This experimental result proves that with the help of DFT spread technique, the nonlinearity tolerance can be significantly improved during the long haul transmission.

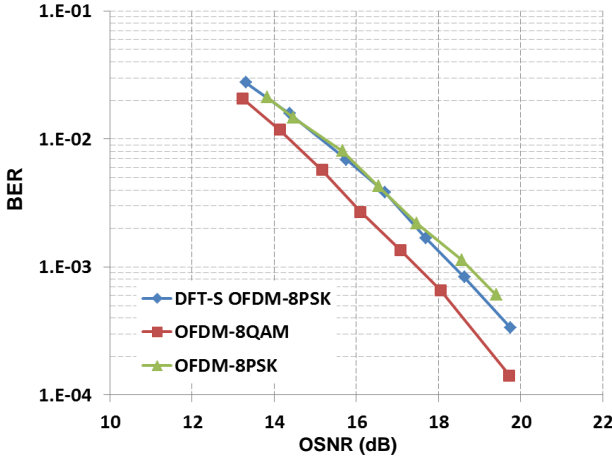


Fig. 2 BER performance against OSNR for DFT-S OFDM-8PSK, OFDM-8QAM, and OFDM-8PSK in a back-to-back configuration.

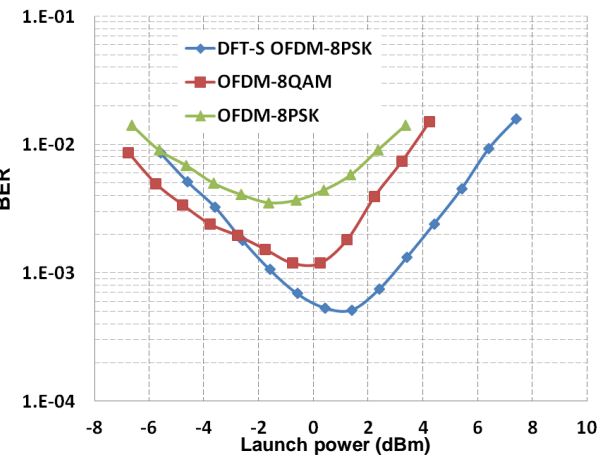


Fig. 3 BER vs. launch power for DFT-S OFDM-8PSK, OFDM-8QAM, and OFDM-8PSK after 2240 km transmission.

Fig. 4 shows BER versus OSNR for a 103 Gb/s CO-OFDM signal after 2240 km SSMF transmission. Each curve is tested under its corresponding optimum launch power. The required OSNR (BER = 10^{-3}) for OFDM-8QAM is 22 dB. In contrast to the results in back-to-back, the required OSNR for DFT-S OFDM-8PSK is 1.4 dB better than OFDM-8QAM, which is due to the improved nonlinearities caused by the DFT spread during the transmission.

Finally, we carry out the BER measurement for all 168 bands after 2240 SSMF transmission, which is shown in Fig. 5. All the tested BERs are under 20.5% FEC threshold (2×10^{-2}). The inset shows the optical spectrum of the entire C-band signal after 2240 km transmission.

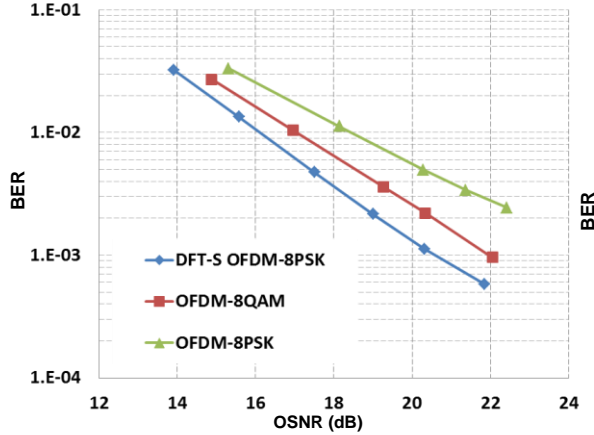


Fig. 4 BER performance against OSNR for DFT-S OFDM-8PSK, OFDM-8QAM, and OFDM-8PSK after 2240 km transmission.

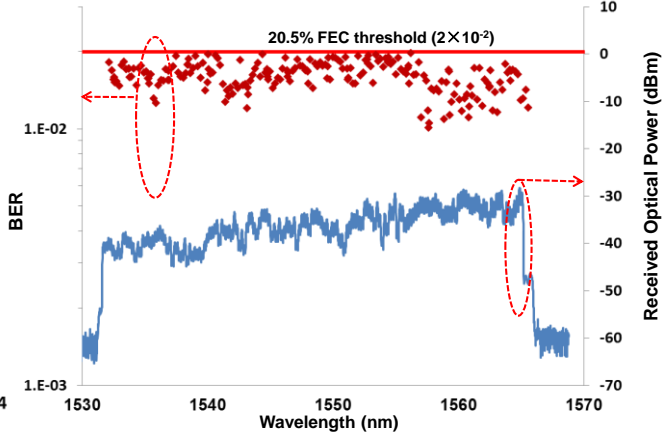


Fig. 5 BER performance for DFT-S OFDM-8PSK after 2240 km transmission.

4. Conclusions

With the help of DFT-S OFDM-8PSK, and distributed Raman amplification, we successfully demonstrate a 168×103 Gb/s DFT-S OFDM transmission over 2240 km SSMF at ITU-T standardized 25 GHz channel spacing. The spectral efficiency within each channel is 5.64 bit/s/Hz.

Acknowledgement

This work is supported by the National Basic Research (973) Program of China (2010CB328300), and 863 Program of China (2012AA011302).

5. References

- [1] W. Shieh et al., Electronics Letters, 42, 587 (2006).
- [2] Q. Yang et al., J. Lightwave Technol. 27, 168, (2009).
- [3] Y. Ma et al., Opt. Express 17, 9421, (2009).
- [4] G. Shen et al., IEEE Communications Letters, 15, 890 (2011).
- [5] X. Liu et al., J. Lightw. Technol., 29, 483-490, (2011).
- [6] D. Qian et al., J. Lightwave Technology, 30, 1540 (2012).
- [7] A. Lowery, Opt. Express, 15, 12965 (2007).
- [8] X. Liu et al., J. Lightw. Technol., 27, 3632 (2009).
- [9] M. Nazarathy et al., Opt. Express, 16, 15777 (2008).
- [10] Y. Tang et al., Photon. Technol. Lett. 22 , 1250–1252 (2010).
- [11] Q. Yang et al., Opt. Express 20, 2379 (2012).
- [12] X. Chen et al., Opt. Express 19, 26198 (2011).
- [13] C. Li et al., P. Technology Letters, 24, 1704-1707, (2012).
- [14] ITU-T G.694.1 standard.
- [15] Z. He et al., OFC'2012, paper JW2A.43, (2012).

Experimental assessment of an OFDMA-based statistical PON with flexible bandwidth allocation and sign-labels

Iván N.Cano, Ángel Peralta, Xavier Escayola, Victor Polo, María C. Santos, Josep Prat

Department of Signal Theory and Communications, Universitat Politècnica de Catalunya, Jordi Girona 1-3, E-08034, Barcelona, Spain
ivan.cano@tsc.upc.edu

Abstract: A statistical OFDM-PON was experimentally tested with flexible bandwidth allocation for proper detection of ONUs with differential link loss. Sign-labels were also added to boost the system sensitivity by 3dB.

OCIS codes: (060.0060) Fiber optics and optical communication; (060.2330) Fiber optics communications

1. Introduction

Orthogonal frequency division multiple access (OFDMA) has been proposed as candidate for the second next generation passive optical networks (PON) due to features like high dispersion tolerance and fine bandwidth (BW) granularity [1]. A statistical network with non-preselected light sources and wavelength control was proposed to keep OFDMA-PON cost-attractive [2, 3]. Besides, to keep the receivers simple, direct-detection with sign-label insertion was adopted to increase the sensitivity by 3dB [4].

A system requirement demanded by operators for future PONs is the reuse of existing fiber infrastructure [5]. This demands the receiver to have sufficient dynamic range to handle differential losses cause by users spread around a central office. This paper experimentally investigates the use of flexible BW allocation in OFDM to compensate for the difference in loses encountered by the several users of the PON. The study was based on a statistical network with identical ONUs with the purpose to keep implementation simple.

2. Network topology

A power splitter based PON tree architecture with multiple services like the one of Accordance (Fig. 1a) [6]. The network is a statistical OFMDA-PON where both the OLT and ONUs are based on low-cost IMDD. The ONU transmitter (Tx) consists a λ random distributed feedback (DFB) laser with temperature and current control circuit to regulate the emission λ and avoid optical beat interference (OBI). This control allowed a λ shift of up to 1.6nm with steps of 0.02nm. The use of temperature and current control simultaneously helped to reduce the transition time from few seconds to less than a second (Fig. 1b). The OLT contains an intelligent algorithm like the one proposed in [2] to adjust the λ of the ONUs lasers by sending instruction to the circuits.

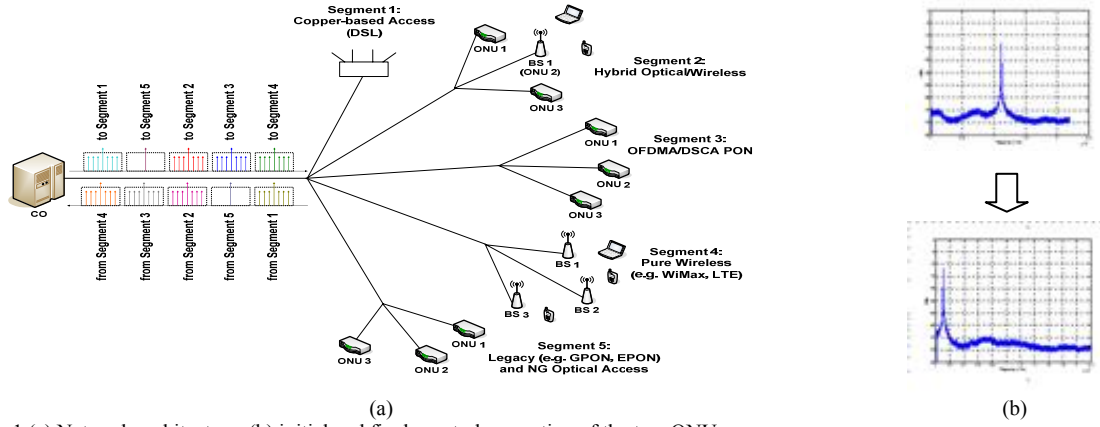


Fig. 1 (a) Network architecture, (b) initial and final spectral separation of the two ONUs

3. Experimental setup

The study was mainly related to the upstream because it is more challenging than downlink. The experimental setup consisted of two ONUs transmitting initially at 1554.5nm and 1554.7nm. ONU₁ was connected to the PON and afterwards ONU₂ was turned on. Then ONU₂ was tuned to displace its emission λ rapidly by 0.1nm to 1554.6nm where reception can still be carried out without high interference. Both ONUs were then transmitting data simultaneously towards the OLT as depicted in Fig. 2a. For each ONU, 2^{18} bits were generated randomly and

mapped into quadrature phase shift keying modulation (QPSK). In order to get a real signal, the QPSK symbols were accommodated to have Hermitian symmetry in the iFFT. To test the bandwidth allocation, the total 256 subcarriers were divided between ONU₁ and ONU₂, which used the lower and higher frequencies respectively. The remaining subcarriers were set to zero in each ONU as shown in the insets of Fig. 2a. The OFDM signals were loaded in an arbitrary wavelength generator (AWG) which produced samples at 5GSa/s with 8 bits resolution in two separate channels. Each output signal then directly modulated non-preselected DFB laser, launching a power of 0dBm each. The Tx optical power of each ONU was controlled by a variable optical attenuator (VOA). Both optical signals were then joined by a 50/50 coupler and the complete OFDM uplink signal passed through an 8dB optical attenuator for emulating a total splitting ratio of 16. The signal then travelled through 25km of single mode fiber (SMF) and was detected by a single 10GHz PIN photodiode (PD) preceded by an erbium doped fiber optical amplifier (EDFA) which kept the input optical power to the PD at -9dBm. The signal was then sampled with a 50GHz real-time sampling oscilloscope which also processed the data immediately after sampling in a pseudo-real-time way. Finally the bit error ratio (BER) for each ONU was computed. To improve the sensitivity of the system, the absolute value of the electrical OFDM signal was taken and a label indicating the samples that were negative was added. The receiver (Rx) simply determined the samples that had to be set negative with the help of the sign-label. The signals and a schematic of the Tx and Rx are shown in Fig. 2b.

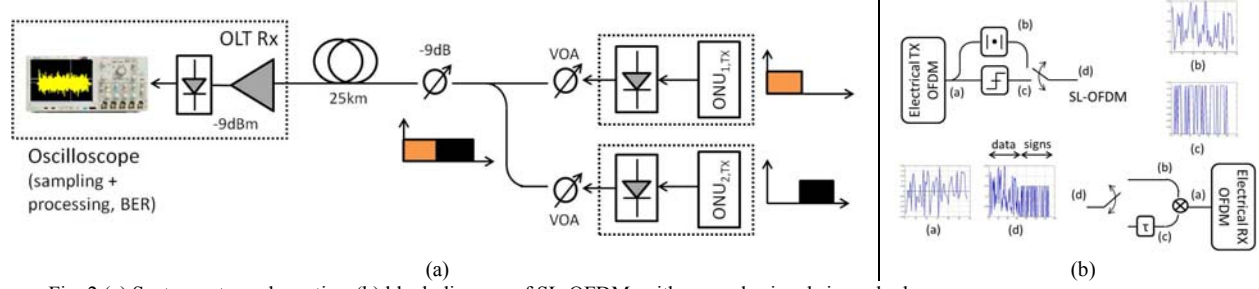
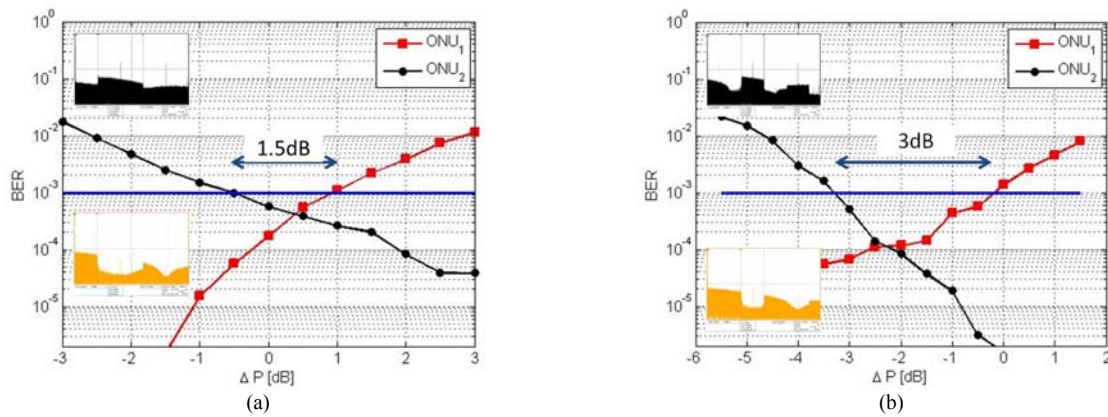


Fig. 2 (a) System setup schematics, (b) block diagram of SL-OFDM with example signals in each phase

4. Results

Firstly, the total BW was divided equally among the two ONUs, adjusting the power also to be equal for both ONUs. Then, the Tx optical power of ONU₂ was varied keeping constant ONU₁ power. Fig. 3a plots the average BER of ONU₁ and ONU₂ obtained against the difference in power measured considering ONU₁ as reference ($\Delta P = P_{\text{ONU}1} - P_{\text{ONU}2}$) with equal BW for both ONUs. Considering a target FEC limit BER of 10^{-3} , it can be noticed that the dynamic range margin of the receiver is extremely limited (around 1.5dB) highly constraining the network design. This is because the noise from the two ONUs add up and being so close in spectrum reduces the performance of the system. To avoid such limitation, the subcarriers were asymmetrically allocated to the ONUs. The spectrum of ONU₂ was reduced by half and the freed BW was added to ONU₁. The cases when ONU₂ has 25%, 12.5% and 3.125% of the BW are plotted in Fig. 3b, 3c, and 3d respectively. Notably, the dynamic range of the Rx increased and the ONUs can transmit up to a limit of 3dB, 4.25dB, and 9.1 dB power difference correspondingly and still both being properly simultaneously detected.



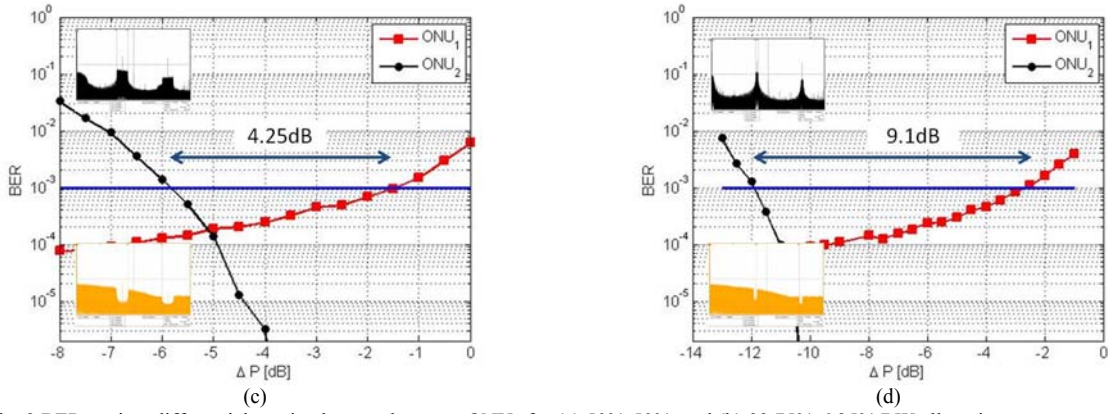


Fig. 3 BER against differential received power between ONUs for (a) 50%-50%, and (b) 93.75%-6.25% BW allocation

To further increase the sensitivity of the system, the sign-label was tested for downlink following the setup of Fig. 2 with QPSK modulation and 256-points FFT. Fig. 4a and 4b plot the performance in terms of the BER against the received optical power with an APD and a PIN in the Rx correspondingly. The use of the sign-label boosts the receiver sensitivity by a little more than 3dB at the FEC limit of $BER=10^{-3}$. The lower sensitivity observed when using the APD is explained by the absence of optical amplifier and a higher electrical noise.

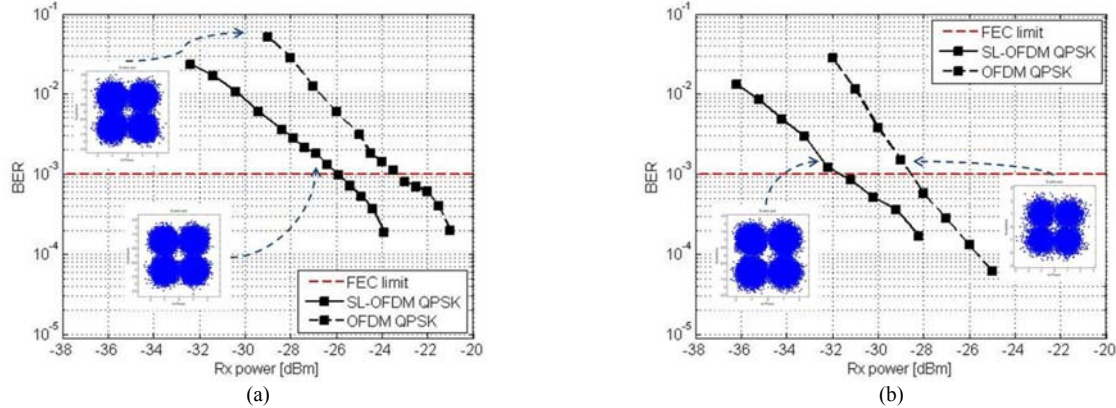


Fig. 4 BER plot against received optical power with an (a) APD and (b) PIN PD in Rx

5. Conclusions

A statistical OFDMA-based PON with flexible BW allocation was experimentally tested. The available BW was partitioned asymmetrically among two ONUs and the received power needed for detecting both OFDM signals simultaneously at an acceptable BER was measured. With the flexible BW, the differential power increased from 1.5dB when the BW is distributed equal to 11.4dB when the lower rate ONU gets only 1 subcarrier. Moreover, a sing label was added to the downlink to further enhance the sensitivity of the receiver. These labels could be used in the upstream signal in an interleaved way. The results motivate for keeping the research on OFDM-PONs and its BW granularity feature to compensate for differential link-losses appearing in deployed fiber infrastructure.

This work was supported by European project ACCORDANCE and CONACYT grant 185291

6. References

- [1] N. Cvijetic, "OFDM for next-generation optical access networks," *J. Lightw. Technol.* **30**, 384-398 (2012)
- [2] I.Cano, M.C.Santos, V.Polo, and J.Prat, "Dimensioning of OFDMA PON with non-preselected independent ONUs sources and wavelength-control," in *Proc. of ECOC*, Geneva, Switzerland, 2011, paper Tu.5.C.2
- [3] W.Poehlmann, T. Pfeiffer, "Demonstration of wavelength-set division multiplexing for a cost effective PON with up to 80Gbit/s upstream bandwidth," in *Proc. of ECOC*, Geneva, Switzerland, 2011, paper We.9.C.1
- [4] I.Cano, *et al.*, "Sign labeled OFDM with intensity-modulation direct detection in PON," *proc. ECOC 2012*, paper P6.04
- [5] P. Chanclou, *et al.*, "Network operator requirements for the next generation of optical access networks," in *IEEE Network* **26**, 8-14 (2012)
- [6] K.Kanonakis, *et al.*, "An OFDMA-based optical access network architecture exhibiting ultra-high capacity and wireline-wireless convergence," in *IEEE Commun. Mag.* **50**, 71-78 (2012)

First Demonstration of Cross Stratum Resilience for Data Center Services in OpenFlow-based Flexi-Grid Optical Networks

Hui Yang¹, Jie Zhang¹, Yongli Zhao¹, Shanguo Huang¹, Yuefeng Ji¹, Jianrui Han², Yi Lin², Young Lee²

(1) State Key Laboratory of Information Photonics and Optical Communications, Beijing University of Posts and Telecommunications, China;

(2) Huawei Technologies Co., Ltd. Email address: {fyanghui, lgr24, yonglizhao}@bupt.edu.cn

Abstract: We demonstrate for the first time cross stratum resilience for data center services in OpenFlow-based Flexi-Grid optical networks. The results from a large scale trial are first verified on our testbed with 200 OpenFlow-enabled nodes.

OCIS codes: (060.4250) Networks; (060.4256) Networks, network optimization; (060.4510) Optical communications

1. Introduction

With the emergence of cloud computing and high-bitrate video applications, data center services have presented the high burstiness and high-bandwidth characteristics, especially including super-wavelength application beyond 100G. In order to support these channels operating flexibly, data center networks can be interconnected by Flexi-Grid optical networks to allocate spectral resources in a dynamic and efficient manner [1-2]. Additionally, an increasing number of network-based data center applications require the end-to-end quality of experience (QoE) guarantees [3]. In case of complete network link or data center failure, depending on the technological heterogeneity and resource diversity, the recovery of services guaranteeing end-to-end QoE is practically impossible in independent operation scenario. Therefore, from the operators' point of view, it is necessary to globally control network and application resources to incorporate resilience in such a combined data center and Flexi-Grid optical network environment.

For the first time, this paper proposes a novel cross stratum resilience (CSR) architecture for data center services in OpenFlow-based Flexi-Grid optical networks, by introducing a data center resource management (DCRM) strategy. CSR can enable a joint optical network and application stratum resources cooperation to enhance the service resilience and responsiveness of end-to-end data center demands. The overall feasibility and efficiency of the proposed architecture is also experimentally demonstrated on our OaaS testbed [4] with 200 OpenFlow-based Flexi-Grid optical nodes [5-6] for the first time in terms of blocking probability and path resilience latency.

2. CSR functional architecture

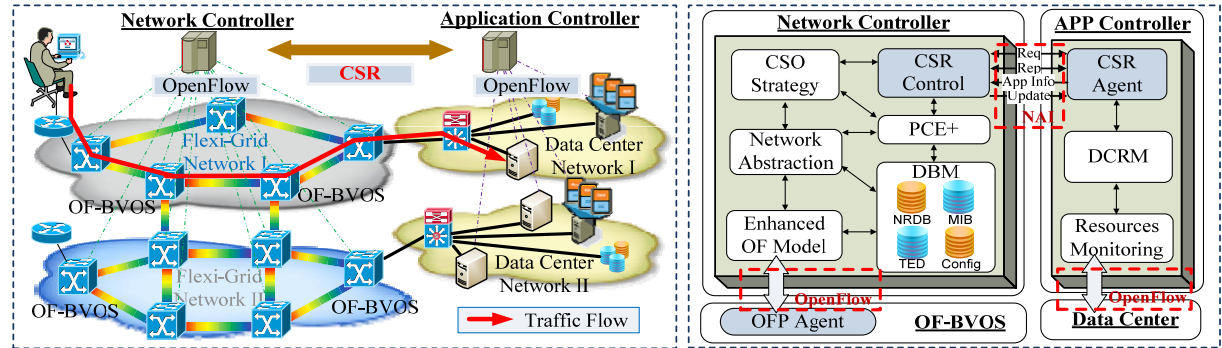


Fig. 1. The architecture of CSR for DC services in OF-based Flexi-Grid optical networks. Fig. 2. The functional models of CSR architecture.

The CSR architecture for data center services in OpenFlow-based Flexi-Grid optical networks is illustrated in Fig. 1. The Flexi-Grid optical stratum networks are used to interconnect distributed data center (DC) networks, the latter of which deployed application stratum resources (e.g., CPU and memory). To control the heterogeneous networks with extended OpenFlow protocol (OFP), OF-enabled bandwidth-variable optical switch nodes with OFP agent software are required, which are referred to as OF-BVOS and proposed and demonstrated in [6]. The architecture especially emphasizes the cooperation between application controller (AC) and network controller (NC) to realize CSR with joint and global interworking of cross stratum resources. The responsibility for the AC is concerned with monitoring and maintaining application stratum resources in DC servers for CSR, while NC sustains network stratum information abstracted from physical network and resilient lightpath provisioning in Flexi-Grid optical networks. Once network or application stratum failure occurs and protection/restoration in single stratum does not guarantee end-to-end QoE, the CSR interacting between AC and NC provides recovery connectivity and application to the user.

The responsibilities of the functional modules in AC and NC are shown in Fig. 2. In NC, network abstraction model abstracts the required optical resources via enhanced OF model and interworks the information to perceive Flexi-Grid networks through extended OFP. In case of complete network link failure, CSR control model decides to apply resilience scheme associated with the application connection via network-application interface (NAI). In AC, CSR agent can receive this request and forward it to data center resource management (DCRM) model in turn, responding the CSR reply with backup DC nodes monitored and maintained in DCRM. Receiving this application resources information from AC, the end-to-end resilient path computation can be completed in PCE considering cross stratum optimization (CSO) strategy of network and application resources [3]. Enhanced OF model performs spectrum assignment for the computed path and provisions the resilient lightpath by using extended OFP.

3. Interworking procedure for CSR with DCRM strategy

DCRM strategy. The application occupation of different service types in each server is expressed using a DCRM table, in which each element indicates the usage of the corresponding DC and service type. The DCRM table of each DC network is maintained in AC as shown in Fig. 3(a). Each row in the table denotes the application usage in the corresponding service type, while the statistics of them represents the service distribution. From another perspective, the sum of each column indicates DC usage among service types. Two maintenance strategies can be implemented in AC with this table. First, at least one server can provide each type in each DC network, so as to the recovery even the gateway or DC failure occurs; moreover, server usage doesn't exceed the failure threshold risk for each DC. The CSO procedure and periodical virtual machine migration using DCRM tables can be proceeded to achieve the aims.

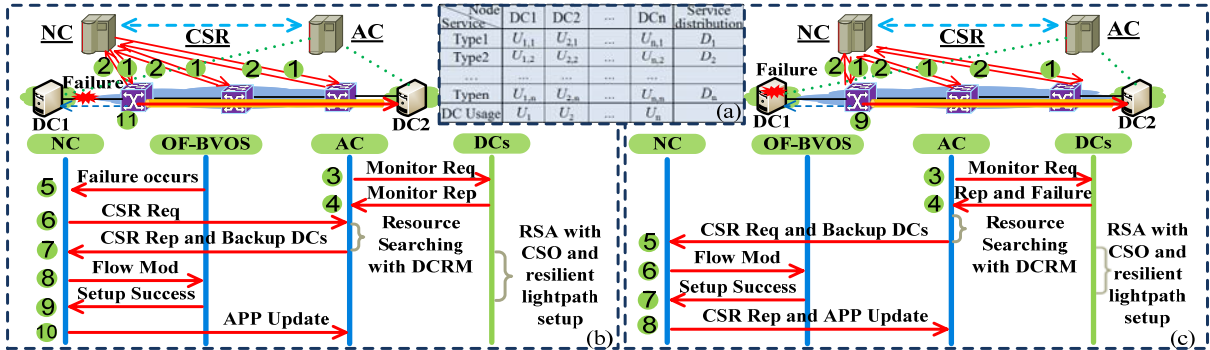


Fig. 3. The DCRM table in AC (a) and interworking procedure of CSR for DC services when (b) network link failure or (c) DC failure occurs.

Interworking procedure of CSR. Fig. 3(b)-(c) show the interworking procedure of CSR for DC services in two failure scenarios, i.e., network link failure and DC failure. In Fig. 3(b), NC sends optical flow monitor request to each OF-BVOS periodically, obtaining status information from them. In case there is a failure in inter-domain link, the providing service from DC1 will fail to be offered to user. The adjacent network node finds the failure and reports it to NC through extended OFP. With the analyzing in network stratum, NC escalates the resilience to DC application for a possible change of resource origin and forwards the request to AC in turn. After the initial session handshake, AC receives CSR request and searches for alternative DC resources and locations with DCRM strategy, and responds to NC the CSR reply with backup DCs. The resilient lightpath considering CSO of optical and application resources can be computed in NC, and then proceeds to establish an end-to-end elastic spectrum path by controlling all corresponding OF-BVOSs along the computed path by using extended OFP. When NC obtains setup success reply from the last OF-BVOS, the service can be recovered utilizing the cross stratum resources effectively. After that, application usage in AC can be updated to keep synchronization by receiving update message from NC. In Fig. 3(c), due to application stratum resources monitored and maintained in AC real-time, in case of the DC failure, AC discovers it timely and looks for the alternative servers in the same host location. If alternative resources are only available in the remote locations, AC provides such information to network stratum for connectivity change of elastic spectrum path guaranteeing the QoE. Receiving the CSR request with application information, NC computes the lightpath with CSO strategy and assigns the spectrum at corresponding OF-BVOS through extended OFP. Then NC updates the application utilization to AC after resilient lightpath provisioning successfully.

4. Large scale demonstration and experimental evaluation

To evaluate the performance of the proposed architecture, we set up a multi-domain Flexi-Grid optical networks with DCs comprising both control and data planes based on our OaaS testbed [4], as shown in Fig. 4 (a). In data plane, two OF-BVOS nodes are equipped with Finisar WaveShaper4000S which has the ability to emulate the super-wavelength traffic. We develop a software OFP agent according to the API function of WaveShaper to control its hardware through OFP. DCs and the other nodes are realized on an array of virtual machines created by VMware

software running at servers. Since each virtual machine has the operation system and its own computation resource, the virtual OS technology makes it easy to set up experiment topology, which is comprised of 200 nodes and divided into 4 domains [4]. The NC is assigned to support the proposed architecture and deployed in three servers for CSR control, CSO computation and extended OF control, while the database servers are responsible for maintaining traffic engineering database, management information base, connection status and the configuration of the database and transport resources. The AC server is used for CSR agent and monitoring the application resources from DC networks with DCRM strategy. User plane is deployed in a server and applies the required application.

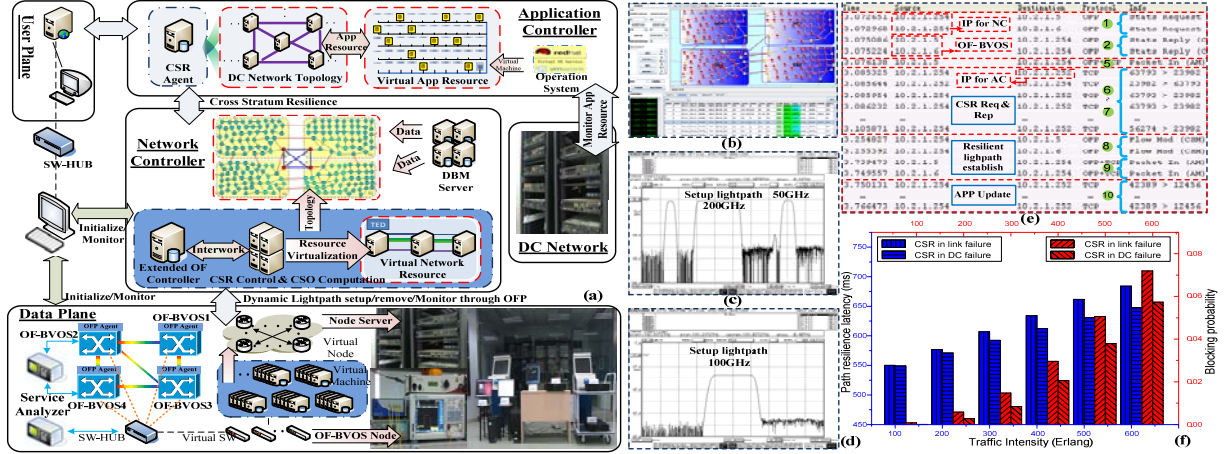


Fig. 4. (a) Experimental testbed for CSR. (b) Application interface of testbed. (c, d) Bandwidth spectrum after CSR. (e) Wireshark capture of the message sequence for CSR in NC. (f) Comparison on path resilience latency and blocking probability between two CSR scenarios.

CSR based on DCRM strategy is verified for DC services and experimentally compared between two failure scenarios on established testbed. The traffic requests from OF-based flexible grid network node to DC node are established with spectrum randomly from 400GHz to 50GHz, where the adjustable minimal frequency slot is 12.5GHz. They arrive to the network following a Poisson process and results have been extracted through the generation of 1×10^5 demands per execution. Two different CSR design scenarios have been designed and implemented when network link and DC failure occur randomly. The experimental results are shown in Fig. 4(b)-(f). Fig. 4(e) illustrates the Wireshark capture of the message sequence for CSR deployed in NC, which are the same as the procedures we depicted in Fig. 3 (b)-(c). In addition, Fig. 4 (f) compares the performances of CSR between two failure scenarios in terms of blocking probability and path resilience latency. As shown, CSR in DC failure scenario reduces blocking probability effectively than link failure scenario, especially when the network is heavily loaded. Another phenomenon can be seen that CSR in DC failure scenario outperforms the other scenario in the path resilience latency significantly. The reason is DC failure can be perceived by AC to process DCRM strategy immediately, while the link failure perceived by NC will be provided to AC for the application information in the other scenario. These results are further emphasized in Fig. 4(b)-(d) which shows application interface and resilient optical spectrum on the link between two OF-BVOS after CSR.

5. Conclusions

This paper proposes a novel cross stratum resilience architecture with DCRM strategy for DC services in OpenFlow-based Flexi-Grid optical networks. For the first time, our experiments demonstrate that CSR can utilize cross optical network and application stratum resources effectively and enhance the end-to-end resilience responsiveness of DC services on OaaS testbed with 200 OF-BVOS nodes.

Acknowledgment

This work has been supported in part by 863 program (2012AA011301), 973 program (2010CB328204), NSFC project (61271189, 61201154, and 60932004) and RFDP Project (20090005110013).

6. References

- [1] G. Shen, et al., "From coarse grid to mini-grid to gridless: How much can gridless help contentionless," Proc. of OFC/NFOEC, OTuI3 (2011).
- [2] T. Takagi, H. Hasegawa, K. Sato and et al., "Disruption Minimized Spectrum Defragmentation in Elastic Optical Path Networks That Adopt Distance Adaptive Modulation," Proc. of ECOC, Mo.2.K.3 (2011).
- [3] H. Yang, et al., "Cross Stratum Optimization of Application and Network Resource based on Global Load Balancing Strategy in Dynamic Optical Networks," Proc. of OFC/NFOEC, JTh2A.38 (2012).
- [4] Y. Zhao, et al., "Experimental Demonstration of Optical as a Service (OaaS) based on OpenFlow," Proc. of OECC, PDP1-4 (2012).
- [5] M. Channegowda, et al., "First Demonstration of an OpenFlow based Software-Defined Optical Network Employing Packet, Fixed and Flexible DWDM Grid Technologies on an International Multi -Domain Testbed," Proc. of ECOC, Th.3.D.2 (2012).
- [6] J. Zhang, et al., "Experimental Setup for OpenFlow-based Elastic Lightpath Provisioning in Flexi-Grid Optical Networks," ECOC2012, P5.01.

Shared Backup Path Protection (SBPP) in Elastic Optical Transport Networks

Gangxiang Shen^{1*}, Yue Wei¹, Qi Yang²

1. School of Electronic and Information Engineering, Soochow University, Suzhou, Jiangsu 215006, China

2. State Key Laboratory of Optical Communication Technologies and Networks, Wuhan, Hubei 430074, China

*Correspondence email: shengx@suda.edu.cn

Abstract: We consider the share backup path protection (SBPP) and 1+1 protection techniques for CO-OFDM-based elastic optical networks. We develop mixed integer linear programming (MILP) models to minimize required protection capacity and used link spectrum in the network.

OCIS codes: (060.4250) Networks; (060.4257) Networks, network survivability

1. Introduction

The coherent optical orthogonal frequency division multiplexing (CO-OFDM)-based elastic optical networks receive much attention due to its flexibility in bandwidth allocation and efficiency of fiber spectrum utilization [1]. Though many studies have been carried out for the design and performance evaluation on this type of network, most of them considered unprotected lightpath services. Only few studies considered the issue of network protection [2-3]. Network protection is of paramount importance for an optical transport network since it carries a large amount of traffic demand and any network failure such as a fiber cut can cause a significant number of network services terminated.

Among many network protection techniques, share backup path protection (SBPP) is considered as one of the most promising schemes due to its combined advantages of operational simplicity, speed, and efficiency [4]. SBPP is a *failure-independent* path-oriented scheme where the protection route is identified in advance, and protection capacity is cross-connected on the protection route in real time. Its protection capacity efficiency is realized by protection capacity sharing on the common links of protection lightpaths whose corresponding working lightpaths do not share any common link.

Most of the prior works on SBPP focused on the SONET/SDH networks and recently on the dense wavelength division multiplexing (DWDM) optical networks [4]. In this paper, for the first time we apply the SBPP scheme to the CO-OFDM elastic optical networks [5]. As the unique and challenging features of this study, we need to ensure the special constraints of *spectrum continuity* along a lightpath route and *frequency slot neighboring* in the spectrum domain for each lightpath connection. We develop a mixed integer linear programming (MILP) model for the SBPP scheme. Also, in order to evaluate the capacity efficiency of the SBPP scheme, we compare the results of SBPP with those of the 1+1 scheme in terms of protection capacity and used link spectrum in the network.

2. Shared backup path protection (SBPP) and 1+1 protection

This section introduces the concept of SBPP in contrast to the 1+1 protection scheme in the context of CO-OFDM-based elastic optical network. As shown in Figs. 1 and 2, when a span fails, both of the techniques find a replacing path directly between the two path end-nodes. For example, if span (6-8) fails, working path (1-3-6-8) gets affected and a switch-over is performed onto a predefined protection route (0-2-4-7-8) for failure recovery. Similarly, if span (0-1) fails, working path (0-1-4) gets affected and a switch-over is performed onto a predefined route (0-2-4) for failure recovery. Under the 1+1 protection technique, to enable 100% failure recovery, the same amount of capacity should be reserved on each protection path as that of its corresponding working path. Thus, as shown in Fig. 1, seven frequency slots (FSs) are reserved on the common spans (0-2) and (2-4) that are shared by the two protection routes.

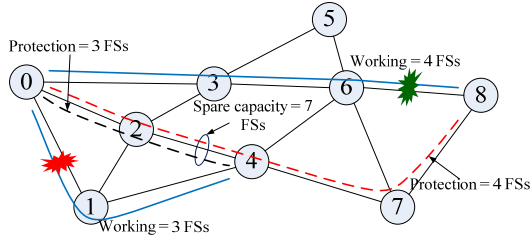


Fig. 1. An example of 1+1 protection

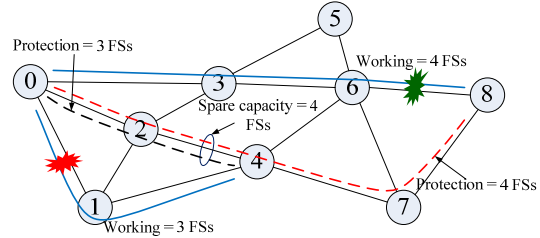


Fig. 2. An example of SBPP protection

In contrast, SBPP is advantageous of allowing protection capacity sharing on the common spans traversed by multiple protection paths if their corresponding working paths do not share any common link. For example, in Fig. 2, spans (0-2) and (2-4) are commonly traversed by two protection paths (0-2-4-7-8) and (0-2-4). As the two working paths do not share any common link, the two protection paths can share protection capacity on the spans to reserve only four FSs, which is sufficient to guarantee full recovery of non-simultaneous failures of spans (0-1) and (6-8).

3. MILP design models for SBPP and 1+1 protection

In this section, we present the MILP models for the above-mentioned two protection schemes. We first introduce the model for SBPP. Given a set of lightpath traffic demands with each requiring a predefined number of FSs, we minimize required protection capacity and used link spectrum in the network. We assume that the elastic optical networks are operated under the flexi-grid mode which assumes that each fiber spectrum is divided into many FSs with a constant small granularity [4]. We also assume that between each pair of nodes there is only a single shortest route employed to establish the working lightpath, while there are multiple routes (link-disjoint from the working route) that can be selected to establish the protection lightpath. The sets and parameters of the model are as follows.

Parameters: S is the set of links. R is the set of node pairs. B_r is the set of backup routes of node pair r . $\eta_i^r = 1$ if failure span i hits the working path of node pair r ; 0, otherwise. $\zeta_j^{r,b} = 1$ if the b^{th} eligible backup route for node pair r crosses span j ; 0, otherwise. $x_r^t = 1$ if the working path for node pair r and the working path for node pair t share a common span; 0, otherwise. $y_r^{b,t} = 1$ if the working path for node pair r and backup path b of node pair t share a common span; 0, otherwise. $z_{a,r}^{b,t} = 1$ if backup path a of node pair r and backup path b of node pair t share a common span and meanwhile their corresponding working paths share a common span; 0, otherwise. d_r is the number of required FSs between node pair r . ∇ is a large value. α is a weight factor.

Variables: $\rho_{b,r} = 1$ if the b^{th} backup route of node pair r is chosen; 0, otherwise. f^r is an integer variable denoting the index of starting FS of the working lightpath between node pair r . e_b^r is an integer variable denoting the index of starting FS of backup path b of node pair r . $\alpha_r^t = 1$ if f^r is larger than f^t ; 0, otherwise. $\beta_r^{b,t} = 1$ if f^r is larger than e_b^t ; 0, otherwise. $\delta_{a,r}^{b,t} = 1$ if e_a^r is larger than e_b^t ; 0, otherwise. s_j is the number of spare capacity units (in FS) assigned on span j . c is the maximum index of the used FSs on all the fiber links in the network.

$$\text{Objective: Minimize } \sum_{j \in S} s_j + \alpha \cdot c \quad (1)$$

Subject to:

$$c \geq f^r + d^r \quad \forall r \in R \quad (2)$$

$$\sum_{b \in B_r} \rho_{b,r} = 1 \quad \forall r \in R \quad (4)$$

$$\sum_{r \in R} \sum_{b \in B_r} \eta_i^r \cdot \rho_{b,r} \cdot \zeta_j^{r,b} \cdot d^r \leq s_j \quad \forall i, j \in S, i \neq j \quad (6)$$

$$f^r + d^r - f^t \leq \nabla \cdot (\alpha_r^t + 1 - x_r^t) \quad \forall r, t \in R, r \neq t \quad (8)$$

$$c \geq e_b^r + d^r \quad \forall r \in R \quad \forall b \in B_r \quad (3)$$

$$e_b^r \leq \nabla \cdot \rho_{b,r} \quad \forall r \in R \quad \forall b \in B_r \quad (5)$$

$$f^t - f^r \leq \nabla \cdot (1 - \alpha_r^t + 1 - x_r^t) - 1 \quad \forall r, t \in R, r \neq t \quad (7)$$

$$e_b^t - f^r \leq \nabla \cdot (1 - \beta_r^{b,t} + 2 - \rho_{b,t} - y_r^{b,t}) - 1 \quad \forall b \in B_t \quad \forall r, t \in R, r \neq t \quad (9)$$

$$e_b^t + d^t - f^r \leq \nabla \cdot (1 - \beta_r^{b,t} + 2 - \rho_{b,t} - y_r^{b,t}) \quad \forall b \in B_t \quad \forall r, t \in R, r \neq t \quad (11)$$

$$f^r + d^r - e_b^t \leq \nabla \cdot (\beta_r^{b,t} + 2 - \rho_{b,t} - y_r^{b,t}) \quad \forall b \in B_t \quad \forall r, t \in R, r \neq t \quad (10)$$

$$e_b^t - e_a^r \leq \nabla \cdot (1 - \delta_{a,r}^{b,t} + 3 - \rho_{b,t} - \rho_{a,r} - z_{a,r}^{b,t}) - 1 \quad \forall a \in B_r \quad \forall b \in B_t \quad \forall r, t \in R, r \neq t \quad (12)$$

$$e_a^r + d^r - e_b^t \leq \nabla \cdot (\delta_{a,r}^{b,t} + 3 - \rho_{b,t} - \rho_{a,r} - z_{a,r}^{b,t}) \quad \forall a \in B_r \quad \forall b \in B_t \quad \forall r, t \in R, r \neq t \quad (13)$$

Objective (1) is to minimize the link protection capacity and used link spectrum of the whole network. Here we set α to be a small value such that minimizing the protection capacity becomes the first priority. Constraints (2) and (3) tell that the maximal FS index in the whole network should be always greater than the ending FS index of the lightpaths between any node pair. Constraint (4) ensures that there is only one backup route selected for any node pair. Constraint (5) says that a backup path between a node pair can be assigned with a starting FS index only if the backup path is selected in constraint (4). Constraint (6) ensures that sufficient spare capacity is reserved on link j such that all the restorable flows can be supported. Constraints (7) and (8) ensure that the allocated spectra for the working paths to different node pairs should not overlap on a common link. Constraints (9), (10), and (11) ensure that the working path of a node pair does not overlap the backup paths of other node pairs in the spectra. Likewise, constraints (12) and (13) ensure that the allocated spectra for the backup paths to different node pairs should not overlap on a common link.

The MILP model for 1+1 protection can be extended from that of SBPP. The differences are as follows: (i) Parameter η_i^r is not required, and constraint (6) becomes $\sum_{r \in R} \sum_{b \in B_r} \zeta_j^{r,b} \cdot d^r \leq s_j$ since spare capacity

sharing is not allowed under the 1+1 protection; (ii) Under 1+1 protection, $z_{a,r}^{b,t} = 1$ if backup path a of node pair r and backup path b of node pair t share a common span; 0, otherwise.

4. Results and discussions

To evaluate the performance of the SBPP and 1+1 protection schemes in the CO-OFDM-based elastic optical networks, we consider three test networks: (a) a six-node eight-link network (n6s8, average nodal degree = 2.7), (b) the 11-node and 26-link COST239 network (average nodal degree = 4.7), and (c) the 14-node 21-link NSFNET network (average nodal degree = 3.0). For all the networks, the traffic demand on each node pair is random with a uniform distribution within a certain range. We set a maximum number of FSs, X , and each node pair can choose any number (between 1 and X) of FSs. Without losing generality, this study sets X to be five. In addition, we employed the K-disjoint shortest path algorithm to find all eligible protection routes for each node pair. All these route are link-disjoint from the shortest working route.

Fig. 3 shows the working and spare capacity and used spectrum in unit of FS for the three test networks. We can see that SBPP can achieve better capacity efficiency than the 1+1 protection scheme in both terms of protection capacity and used link spectrum for all the test networks. This is attributed to the fact that SBPP allows protection capacity sharing among multiple protection lightpaths whose corresponding working lightpaths do not share any common link. Fig. 4 shows the results of *spare capacity redundancy* which is defined as a ratio of total protection capacity to total working capacity. Again, we can see that the SBPP scheme shows to have much lower spare capacity redundancy in all the test cases. In addition, comparing the spare capacity redundancies of the three test networks, we find that the redundancy of the COST239 network is lower than those of the n6s8 and NSFNET networks. This is because the COST239 network has a higher average nodal degree, which increases spare capacity sharing opportunities and thus helps reduce spare capacity redundancy. For the 1+1 scheme, we have a similar observation, i.e., a network with a higher nodal degree tends to have a lower spare capacity redundancy. This is attributed to the fact that a denser network provides more shorter protection routes, which therefore help reduce the sum of link protection capacity.

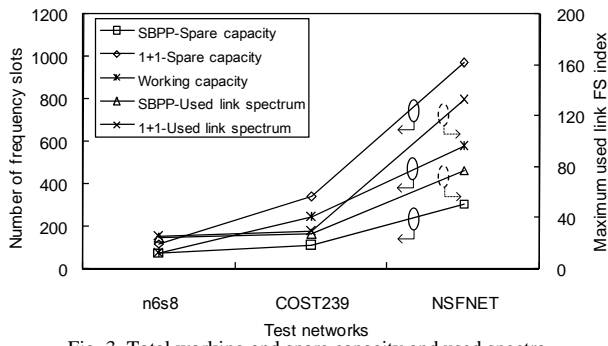


Fig. 3. Total working and spare capacity and used spectra

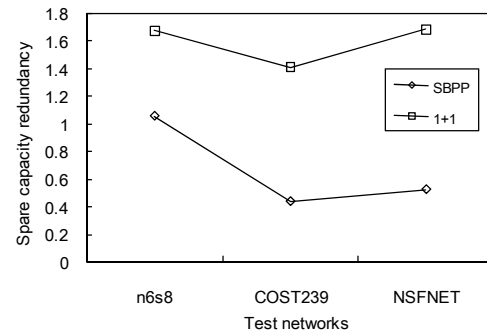


Fig. 4. Spare capacity redundancy

5. Conclusion

We considered the SBPP and 1+1 protection schemes in the context of CO-OFDM-based elastic optical networks. Under the assumption of spectrum continuity, we developed MILP models to minimize required spare capacity and used link spectrum in the network. Due to the spare capacity sharing feature, our results indicate that the SBPP scheme requires much lower spare capacity compared to the traditional 1+1 protection scheme. In addition, it was observed that a higher nodal degree can help improve spare capacity redundancy for SBPP, which is attributed to the fact that a denser network provides more opportunities for spare capacity sharing.

Acknowledgements: This work was jointly supported by the National 863 Plans Project of China (2012AA011302), the National Natural Science Foundation of China (NSFC) (61172057), and the Open Project (2011GZKF031110) from the State Key Laboratory of Adva. Optical Comm. Systems and Netw., Shanghai JiaoTong University, China.

References

- [1] W. Shieh and I. Djordjevic, *OFDM for Optical Communications*, Academic Press, 2009.
- [2] Y. Sone *et al.*, "Highly survivable restoration scheme employing optical bandwidth...," in *Proc. OFC/NFOEC 2009*, Paper OThO2.
- [3] X. Shao *et al.*, "Shared-path protection in OFDM-based optical networks with...," in *Proc. OFC/NFOEC 2012*, Paper OTh4B.
- [4] W. D. Grover, *Mesh-Based Survivable Networks*, Upper Saddle River, NJ: Prentice Hall PTR, 2003, Chap. 6.
- [5] G. Shen and M. Zukerman, "Spectrum-efficient and agile CO-OFDM...," *IEEE Communi. Magazine*, vol. 50, no. 5, pp. 82-89, May 2012.

Postdeadline Session III

Friday, 9 November

15:30 - 17:30

Marigold Room

Postdeadline Submissions from
Subcommittee 6 and from Symposium on Advanced
Photonics Materials

Thin-Film Absorbers based on Gold Nanoparticles decorated Silicon Nanowires on thin Gold film

Fugen Chen, Liu Yang and Sailing He

Centre for Optical and Electromagnetic Research, Zijingang Campus, Zhejiang University, Hangzhou 310058, China

Email: sailing@zju.edu.cn

Abstract: We proposed a thin-film absorber based on gold nanoparticles decorated silicon nanowires on thin gold film, with which broadband and enhanced absorption was experimentally demonstrated compared with others without gold nanoparticles or gold film.

OCIS codes: (160.4236) Nanomaterial; (310.3915) Metallic, opaque, and absorbing coatings.

1. Introduction

Solar energy is a special kind of natural source in abundance for human beings on earth. Photovoltaic solar cells, converting sunlight directly into electricity, are one of the most important technologies to utilize solar energy. Silicon nanowires (SiNWs) have been shown to have high-efficiency sunlight harvesting ability due to the strong scattering of light in them. Moreover, when forming radial p-n or p-i-n junctions or Si-liquid junctions on SiNWs, the photocarrier separation and collection efficiencies can be greatly enhanced due to the short distance for photocarriers to transport to the electrode. Therefore, SiNWs are considered as a promising platform for photovoltaic solar cells ([1] and references therein). Other ways to utilize solar energy are based on converting solar energy into electricity via heat or into heat directly. In these means, solar absorbers are of critical role in harvesting sunlight. Metamaterials are preferred to form electromagnetic wave absorbers in different wavelength bands due to their flexibility of design and ultrahigh absorption under impedance matching conditions ([2] and references therein). In the visible band, metals, supporting surface plasmon polaritons (SPPs), are always employed as the absorbing materials. Here in this paper, we proposed and experimentally demonstrated a novel solar absorber based on gold nanoparticles (AuNPs) decorated SiNWs on gold (Au), where photocarriers are not considered. The SiNWs fabricated by silver (Ag)-assisted electroless etching method are vertically transferred from the Si substrate onto an Au film via crack formation. Without the thick Si substrate, our absorber becomes very thin.

2. Experiments and Results

The schematic diagram of our proposed absorber is shown in Fig. 1. It consists of SiNWs decorated with Au nanoparticles (AuNPs@SiNWs) on top of an Au film. Transparent polydimethylsiloxane (PDMS) used here provide a mechanical support for the SiNWs. The Au film is about 100 nm thick, which is thick enough to suppress light transmission through it. Most AuNPs are randomly placed on the surfaces of SiNWs from their tops to the positions about 3 μ m below. Light incident from the top will be scattered by SiNWs as well as the AuNPs. The scattered light which cannot be absorbed by SiNWs or AuNPs will be reflected by the bottom Au film, re-scattered by the top AuNPs and finally trapped between the two Au layers until being absorbed completely. Therefore, broadband and efficient absorption can be predicted.

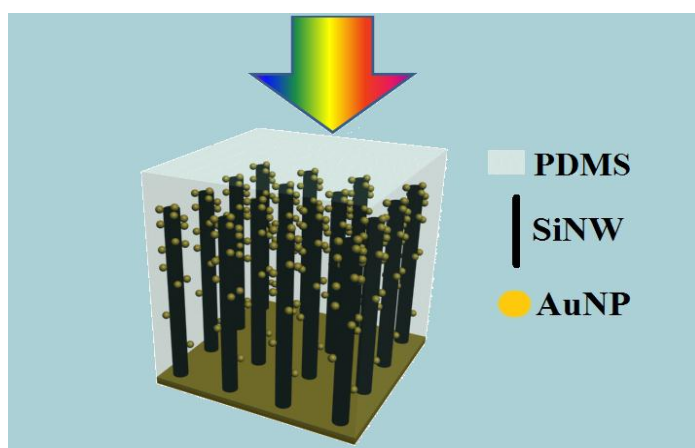


Fig. 1 Schematic diagram of our proposed thin-film absorber.

In our experiments, the well-established Ag-assisted electroless etching method was employed to fabricate SiNWs [3]. First, a clean Si wafer was immersed into a solution of 0.5 M HF/0.005 M AgNO₃ for 2 min at room temperature to form a thin layer of uniform Ag nanonetwork on the surface of the wafer. After that, we put the Ag coated wafer into the etching solution of 10% HF/0.6% H₂O₂ at room temperature for 40 min. Fig. 2(a) shows the SEM (scanning electron microscopy) picture of the etched SiNWs of about 5 μm long, which are uniform in a very large area. The diameters of SiNWs are all about 150 nm as shown in the inset of Fig. 2(a). In order to make the splitting of the SiNWs easier off the Si substrate and still keep their vertical arrangement, we employed a crack-assisted vertical transfer method, reported first by Weisse, et al. [4]. After SiNWs were fabricated, the sample was soaked in a 75 °C DI water bath for 4 hours. During this step, the Ag nanonetwork becomes delaminated and some Ag nanoparticles (AgNPs) are attached to the sidewalls of SiNWs. Being taken out of the water, the sample was quickly dried by nitrogen and even on a hot plate for seconds to thoroughly remove the water between SiNWs, and immediately returned back into the etching solution for a time (which is not very important). At the start of the second etching process, horizontal cracks are formed due to the sidewall AgNPs. As the etching proceeds, the delaminated Ag nanonetwork is healed and reattached to the bottom Si wafer, generating elongated SiNWs. Fig. 2(b) shows the SEM picture of this sample after removal of remaining Ag. From this figure, cracks are clearly seen between the firstly- and secondly-etched SiNWs. In order to decorate the SiNWs with AuNPs, we simply immersed the cracked SiNW wafer into a 1 mM HAuCl₄ solution for 5 min at 60 °C. The SEM picture in Fig. 2(c) shows that AuNPs were deposited randomly on the sidewalls of the start of SiNWs due to the fact that little HAuCl₄ solution could penetrate downwards between SiNWs. With cracks on SiNWs, it is easy to transfer the SiNWs with or without AuNPs from the wafer onto other substrates. Here we utilized PDMS to mechanically support the SiNWs by simply pouring diluted PDMS (with silicone elastomer curing agent at 10:1) into the cracked SiNW arrays. Upon degassing and curing at 80 °C for 2 hours, the PDMS can be peeled off along the cracked interface with the secondly-etched SiNWs left on the thick Si substrate. The firstly-etched SiNWs are embedded in the free PDMS film as shown in Fig. 3. AuNPs@SiNWs can also be transferred with the same method. A 100 nm-thick Au film was sputtered on the cracked end of SiNWs in free PDMS. Finally our absorber schematically shown in Fig. 1 was achieved with AuNPs@SiNWs on Au thin film. For comparison, we also fabricated other absorbers based on SiNWs embedded in PDMS films, namely, pure SiNWs, pure SiNWs on Au thin film, AuNPs@SiNWs, in which SiNWs were fabricated during the above processes.

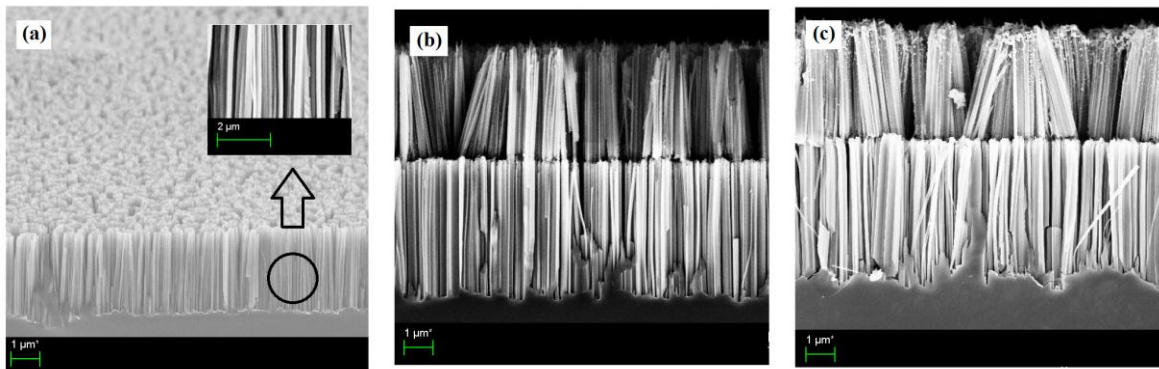


Fig. 2 SEM pictures of (a) first-etched SiNWs; (b) cracked SiNWs; (c) cracked SiNWs decorated with AuNPs.

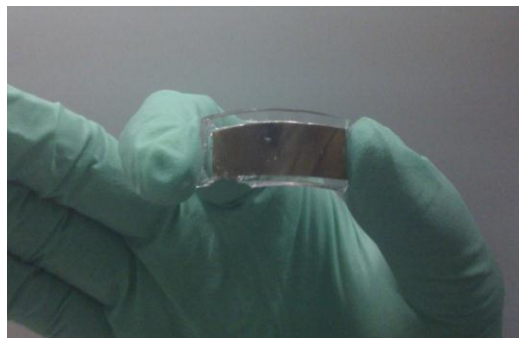


Fig. 3 Optical image of transferred SiNWs embedded in PDMS.

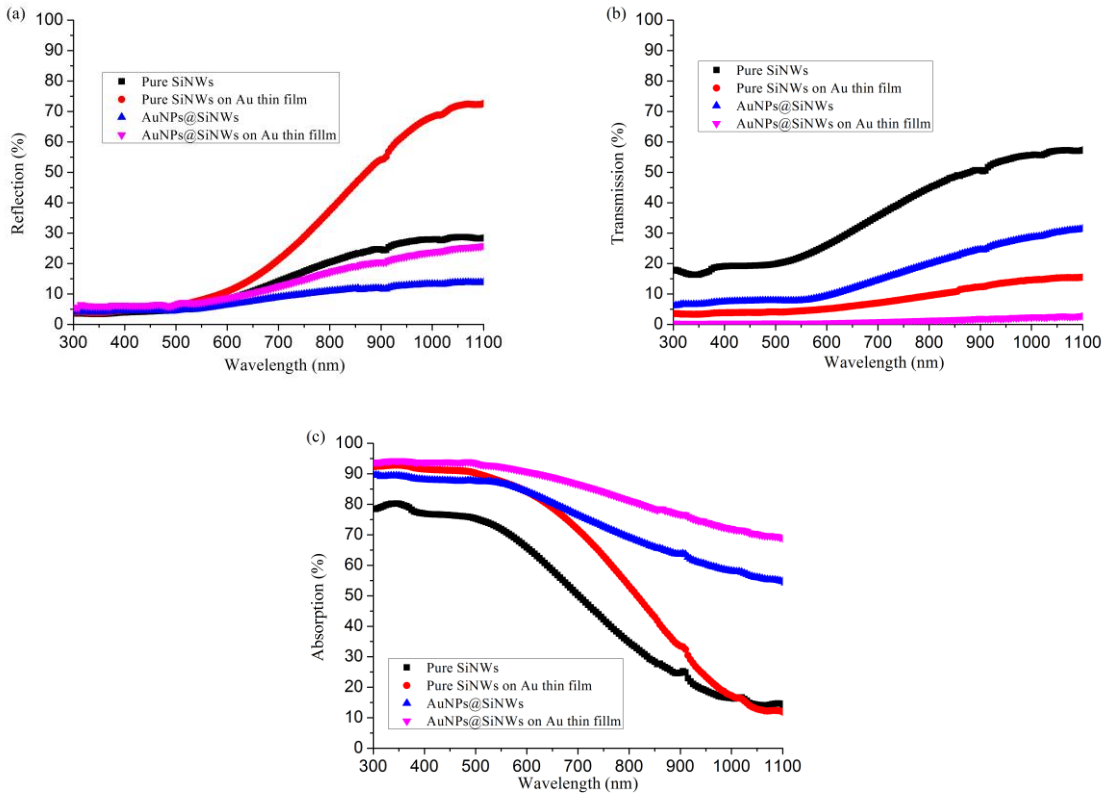


Fig. 4 (a) Reflection, (b) Transmission and (c) Absorption spectra of our proposed solar absorber based AuNPs@SiNWs on Au thin film (purple inverted triangles), pure SiNWs (black rectangles), pure SiNWs on Au thin film (red circles), and AuNPs@SiNWs (blue triangles).

Optical performances of the above absorbers are characterized by Perkin Elmer Lambda 1050 with a 150 mm integrating sphere. The reflection, transmission and absorption spectra are shown in Fig. 4. From Fig. 4(a), one sees comparable low reflections for all absorbers in the wavelength range from 300 to 500 nm. Our absorber shows moderate reflections beyond 500 nm. Comparing the four reflection spectra in Fig. 4(a), we find that top AuNPs help suppress reflection but the bottom Au films are negative for anti-reflection. However, the bottom Au films can significantly reduce light transmission as shown in Fig. 4(b). Since only a small portion of light remains when passing through the top AuNPs and SiNWs (see the transmission spectrum of the AuNPs@SiNWs based absorber indicated by blue triangles in Fig. 4(b)), our absorber shows the smallest transmission spectrum over the whole wavelength range considered here. By extracting reflection and transmission spectra in Figs. 4(a) and (b) from unity, absorption spectra can be easily obtained, which are plotted in Fig. 4(c). Our absorber has the highest absorption spectrum of all absorbers due to the suppression of both reflection and transmission. In detail, absorptions over 80% are obtained in the wavelength range below 840 nm. Typically below 500 nm, absorptions are as high as 94%.

3. Conclusions

In conclusion, we have proposed and fabricated a thin-film solar absorber based on AuNPs@SiNWs on thin Au film. Enhanced absorption was achieved in comparison with other absorbers without top AuNPs or bottom Au film.

4. References

- [1] K. Q. Peng, and S. T. Lee, "Silicon nanowires for photovoltaic solar energy conversion," *Adv. Mater.* **23**, 198-215 (2011).
- [2] C. M. Watts, X. L. Liu, W. J. Padilla, "Metamaterial electromagnetic wave absorbers," *Adv. Mater.* **24**, 98-120 (2012).
- [3] K. Peng, Y. Wu, H. Fang, X. Zhong, Y. Xu, and J. Zhu, "Uniform, axial-orientation alignment of one-dimensional single-crystal silicon nanostructure arrays," *Angew. Chem. Int. Ed.* **44**, 2737-2742 (2005).
- [4] J. M. Weisse, D. R. Kim, et al. "Vertical transfer of uniform silicon nanowire arrays via crack formation," *Nano Lett.* **11**, 1300-1305 (2011).

A Broadband, Omnidirectional Absorber Based on a Slot Waveguide Grating on a Metallic Substrate

Feng Zhang^{1,2}, Liu Yang^{1,2}, Yi Jin^{1,2}, Sailing He^{1,2,*}

¹Centre for Optical and Electromagnetic Research, State Key Laboratory of Modern Optical Instrumentations, Zhejiang University, Hangzhou 310058, China

²Zhejiang Provincial Key Laboratory for Sensing Technologies, Zhejiang University, Hangzhou 310058, China

* Email: sailing@zju.edu.cn

Abstract: We proposed a broadband, omnidirectional absorber based on a slot waveguide grating on a metallic substrate. Average absorption of ~90% was achieved with bandwidth of 1100 nm over a wide angle range (0 - 80 °).

OCIS codes: (160.4236) Nanomaterial; (310.3915) Metallic, opaque, and absorbing coatings.

1. Introduction

Perfect absorption of light without any reflection or transmission is of critical importance in optical energy conversion processes, where broadband perfect absorbers are required to harvest and absorb photons as many as possible. Recent advances in micro-/nano-technology become helpful to create many flexible designs of broadband perfect absorbers based on micro-/nano-structures [1-5]. In our previous work [6], we numerically demonstrated that by combining two kinds of optical modes, namely, Bloch and SPP modes, broadband, omnidirectional, and polarization-independent absorption can be easily achieved. Here in this paper, we will show that by combining multiple physical phenomena together, an ultrabroadband and enhanced absorption can be achieved. Our structure consists of a gold (Au) substrate covered with a Slot Waveguide Grating (SWG), which contains two Ge nanowires (NWs) with a small separation between them in each period. Compared with conventional grating structure with one NW in each period, our SWG-based structure has a rather flatter absorption spectrum over a broad wavelength range from 300 to 1400 nm and is also angle-insensitive (from 0 to 80 °).

2. Simulation and Discussion

Our proposed SWG based absorber is shown in Fig. 1(a), where there are two Ge NWs separated by d in each period on a gold (Au) substrate. The NW widths are set equal, i.e., $w_1 = w_2$, unless otherwise specified. The grating height is set to h . The Au substrate is assumed to be thick enough to avoid any transmission through it. We fix the grating period to 620 nm, i.e., $P = 620$ nm, throughout the paper. For comparison, a conventional grating with only one NW of width, w , in each period is plotted in Fig. 1(b) with the same period, $P = 620$ nm, and the NW height, h .

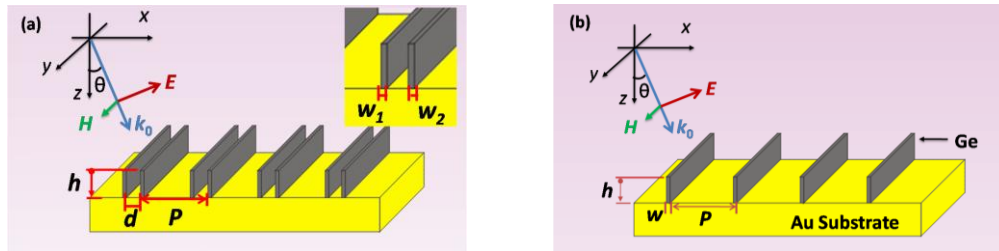


Fig. 1. Schematic diagram of (a) a SWG-based absorber with two NWs in each period; (b) a conventional absorber with only one NW in each period. A TM-polarized plane wave is incident from the top with an incident angle, θ , and a wave vector, k_0 .

We employed the finite element method to simulate the optical responses when a plane wave is incident from the top with an incident angle, θ , and a wave vector, k_0 , as shown in Fig. 1. The light wavelength, λ , is chosen from 300 to 1500 nm, beyond which Ge has little absorption. Here, only transverse-magnetic (TM) polarization is considered in order to excite the polarization-sensitive slot waveguide and SPP modes. The dielectric constant of Ge is chosen from previously published experimental result [7]. And the Au is described by the Drude dielectric function [8], where $\omega_p = 1.3673 \times 10^{16}$ s⁻¹ is the plasma frequency and $\gamma = 1.0027 \times 10^{14}$ s⁻¹ is the damping parameter. Through numerical simulation, the partial absorptions in each of the compositional material, A_{Ge} and A_{Au} , can be calculated via the equation below:

$$A_{\text{Ge or Au}} = \frac{\iint \frac{\pi}{\lambda} \cdot \text{Im}(\epsilon_{\text{Ge or Au}}) |E|^2 dx dy}{\text{Source power}} \quad (1)$$

where, $\text{Im}(\epsilon)$ is the imaginary part of the material's dielectric constant. Then the total absorption, A , equals to the summation of both partial absorptions, that is, $A = A_{\text{Ge}} + A_{\text{Au}}$.

Figs. 2(a) and (b) show the spectra of total absorption, A , and partial absorption in Ge, A_{Ge} , respectively for the conventional absorbers with NW widths of 140 nm (green curve) and 280 nm (red curve), and our SWG-based absorber with $w_1 = w_2 = 140$ nm and $d = 95$ nm (blue curve). We name these three structures Case 1, Case 2, and Case 3, respectively for easy description. From Fig. 2, it is shown that for all three cases absorptions in Ge dominate the total absorptions in the wavelength range below 1400 nm and there are sharp drops around 1400 nm, beyond which the absorption of Ge indicated by the imaginary part of its refractive index is at least one order of magnitude smaller [7]. Here Au's absorptions become larger due to excitations of SPPs, but do not contribute much to the total absorption. In both Ge absorption and total absorption spectra shown in Figs. 2(a) and (b), ripples can be observed, which are mainly due to the Fabry-Parot (FP) interferences between the forward and backward waves reflected by the Au and grating surfaces. Since the grating heights are all the same in the three cases, the small peaks in these absorption spectra appear at almost the same wavelengths.

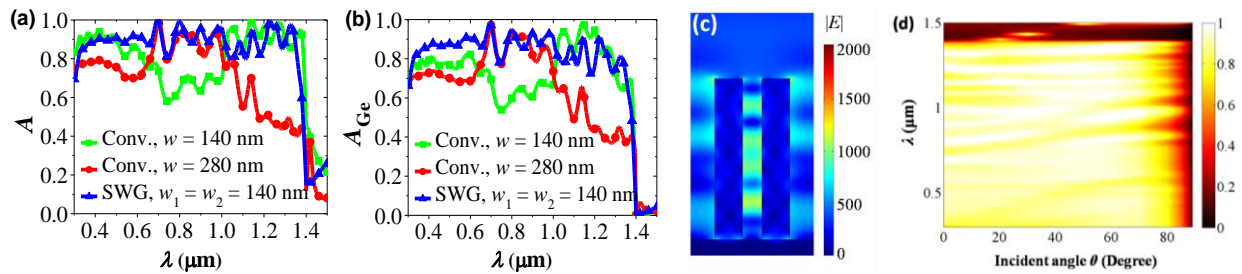


Fig. 2. Spectra of (a) Total absorption, A ; and (b) partial absorption in Ge, A_{Ge} ; for three cases: Cases 1 and 2 are the conventional cases with $w = 140$ nm (green curve) and $w = 280$ nm (red curve); Case 3 is our SWG-based nanostructure with $w_1 = w_2 = 140$ nm and $d = 95$ nm (blue curve), respectively. Other structural parameters are: $P = 620$ nm and $h = 1500$ nm. (c) Electric filed distribution, $|E|$, at $\lambda = 1230$ nm for Case 3. (d) The angle-resolved absorption spectra for Case 3.

For Cases 1 and 2, three sections appear clearly in the absorption spectra in the wavelength range below 1400 nm as shown in Figs. 2(a) and (b). Absorption of Case 1 is higher than that of Case 2 in the ranges of $\lambda < 620$ nm and $\lambda > 1000$ nm, but is lower in the range of $620 \text{ nm} < \lambda < 1000$ nm. According to the diffraction theory, in the wavelength range of $\lambda < P = 620$ nm, reflective diffraction orders are stronger in Case 2 of $w = 280$ nm due to its larger filling ratio, producing lower absorption than Case 1 of $w = 140$ nm. At $\lambda = 620$ nm, Rayleigh anomaly occurs, where the 1st reflective diffraction order becomes propagating horizontally along the air-grating surface. Therefore, absorption increases in Case 2 but decreases in Case 1 where the light experiences less absorbing material as shown in Figs. 2(a) and (b). According to the phase-matching condition for the refractive diffractions, the 1st refractive diffraction order becomes another Rayleigh anomaly at $\lambda = 1096$ nm for case 1 and propagating horizontally along x direction. For Case 2, Rayleigh anomaly of the 2nd refractive diffraction order occurs at $\lambda = 822$ nm. And for the wavelengths beyond each Rayleigh anomaly, the energy will be redistributed between the remaining diffraction orders, of which the 0-order diffraction gains more energy. Then the FP resonances in the y direction dominate the absorption spectra. In the wavelength range beyond 1000 nm, we find that SPPs are excited at the bottom interface between Ge NW and Au with one and three magnetic field maxima respectively for Cases 1 and 2. In contrast with Case 1 with narrow 140 nm-wide NW in each period, much more light is leaking out of the wider 280 nm-wide NW in Case 2. This is due to the fact that the phase changes twice along the x direction within the Ge NW, which evolves gradually from the bottom phase induced by the excited higher-order SPP mode at the surface of the Au substrate. Such phase change along the x direction makes the wider NW "narrower", resulting in a worse confinement than the narrower half-width NW.

Interestingly, by introducing a slot into the 280 nm-wide NW in each period, an ultra-broadband absorption spectrum was achieved for our proposed absorber of Case 3 combining both merits of Cases 1 and 2 as shown in Figs. 2(a) and (b). In the short wavelength range below 1000 nm, stronger scattering is generated by two NWs in each period in Case 3 where the 1st refractive diffraction order experiences more changes of index in comparison with Case 2 of one 280 nm-wide NW in each period, and more absorbing materials in comparison with Case 1 of

one 140 nm-wide NWs in each period. Therefore, the absorption spectrum becomes flatter with absorption comparable to that of Case 1 at $\lambda < 620$ nm and to that of Case 2 at $620 \text{ nm} < \lambda < 1000$ nm. In the long wavelength range beyond 1000 nm, SPPs are also generated with well-confined magnetic field at the bottom of each Ge NW. In comparison with Case 2, the slot inserted in the 280 nm-wide NW totally redistributes the initial phase distribution of SPPs at the bottom surface of Ge NW. And it gives a smooth phase change along the x direction within each Ge NW and thus a better confinement of magnetic field. Meanwhile, since the two NWs are separated by a rather small distance of $d = 95$ nm, the evanescent electric fields of the NWs overlap in the slot, generating slot waveguide mode [9] with much stronger electric field confined in it as shown in Fig. 2(c). Quite different from Case 2 with a 280 nm-wide NW in each period, light impinging on the SWG of Case 3 sees a waveguide array of lower effective refractive indices consisting of two NWs and a slot in between in each period. Therefore, more FP fringes are generated in such slot waveguides. The combined optical behaviors contribute to enhanced absorption in this wavelength range compared with Case 2. In general, our proposed SWG-based absorber, Case 3, has a much better absorption performance over the whole wavelength range from 300 to 1400 nm as shown in Fig. 2(a). In comparison with the partial absorption spectra of Ge is shown in Fig. 2(b), Ge SWG itself is a very good absorber and our proposed SWG-based absorber, Case 3, can be exploited further for a high-efficiency photovoltaic solar cell with the Ge SWG as the solar absorber and the Au substrate as the bottom electrode, where the directions of light absorption and photocarrier collection can be orthogonalized to further enhance its power conversion efficiency. Fig. 2(d) shows the angle dependence of the absorption spectra. It shows that the absorption spectrum are maintained well even when the light is incident at a very large angle of 80°.

3. Conclusion

In summary, an ultrabroadband and omnidirectional absorber has been investigated systematically. The numerical results show that average absorption of ~90% was achieved over a broad wavelength range from 300 to 1400 nm and a wide angle range from 0 to 80°.

4. References

- [1] H. A. Atwater and A. Polman, "Plasmonics for improved photovoltaic devices," *Nat. Mater.*, **9**(3), 205-213 (2010).
- [2] C. M. Watts, X. Liu, and W. J. Padilla, "Metamaterial electromagnetic wave absorbers," *Adv. Mater.*, **24**, OP98–OP120 (2012).
- [3] K. Aydin, et al., "Broadband polarization-independent resonant light absorption using ultrathin plasmonic super absorbers," *Nat. Commun.*, **2**, 517 (2011).
- [4] Y. Cui, et al., "Ultra-broadband Light Absorption by a Sawtooth Anisotropic Metamaterial Slab," *Nano Lett.*, **12**(3), 1443-7 (2011).
- [5] T. Søndergaard, et al., "Plasmonic black gold by adiabatic nanofocusing and absorption of light in ultra-sharp convex grooves," *Nat. Commun.*, **3**(969), 22828629 (2012).
- [6] L. Yang, L. Mo, Y. Okuno, and S. He, "Optimal design of ultra-broadband, omnidirectional, and polarization-insensitive amorphous silicon solar cells with a core-shell nanograting structure," *Prog. Photovolt.: Res. Appl.*, DOI: 10.1002/pip.2206 (2012).
- [7] David F. Edwards, "Germanium (Ge)" in *Handbook of Optical Constants of Solids*, E.D. Palik, ed. (Academic, Orlando, Fla. 1985).
- [8] A. Vial, A. S. Grimault, D. Macías, and D. Barchiesi, "Improved analytical fit of gold dispersion: application to the modeling of extinction spectra with the FDTD method," *Phys. Rev. B*, **71**(8), 085416–085422 (2005).
- [9] V. R. Almeida, et al., "Guiding and confining light in void nanostructure," *Opt. Lett.*, **29**(11), 1209–1211 (2004).

Multiband electromagnetic absorbers based on a metal/dielectric multilayer stack

Wenyan wang¹, Yanxia Cui^{1,2,*}, Jun Xu³, Yinyue Lin¹, Ximin Tian¹,

Yuying Hao¹, Sailing He², and Nicholas X. Fang³

¹College of Physics and Optoelectronics, Taiyuan University of Technology, Taiyuan 030024, China

²Centre for Optical and Electromagnetic Research, State Key Laboratory of Modern Optical Instrumentation, JORCEP (KTH-ZJU Joint Center of Photonics), Zhejiang University, Hangzhou, Zhejiang 310058, China

³Department of Mechanical Engineering, Massachusetts Institute of Technology, Cambridge, Massachusetts 02139, USA

* yanxiacui@gmail.com

Abstract: Based on a planar structure comprising of a metal/dielectric multilayer stack and a thick metal substrate layer, we have obtained an omnidirectional, polarization-insensitive and multiband thin absorber in the visible regime.

OCIS codes: (230.4170) Multilayers (310.6860) Thin films, optical properties (310.3915) Metallic, opaque, and absorbing coating

1. Introduction

Over the past years, electromagnetic (EM) wave absorbers have been extensively investigated driven by the potential applications in thermo-photovoltaics, thermal emitters, EM modulators, and sensors [1]. There are diverse means to design an efficient EM absorber working at a single frequency, such as using a metamaterial layer [2] or a metallic grating [3].

Recently, a series of work focus on overcoming the narrowband limit of EM absorbers for the special use in solar energy harvesting and explosive detection. By blending various different strong resonators together within one unit cell, one can obtain multiband/broadband absorption in the spectra (see references 84-106 in Ref. [1]). Broadband absorption can also be realized based on some interference mechanisms [4]. In 2012, Cui *et. al* designed an ultra-broadband absorber with a FWHM of 86% using a tapered slowlight anisotropic metamaterial device [5]. However, most of these multiband/broadband designs are difficult to be fabricated due to the structure complexity.

In contrast, one-dimensional (1D) planar stacks require very little nanofabrication. Using periodic metal-dielectric multilayer stacks on a dielectric substrate, good spectral selectivity for thermal emitter applications has already been predicted experimentally in 2004 [6]. Later, Lee and Zhang proposed an asymmetric Fabry-Perot (FP) resonance cavity constructed by coating a dielectric layer onto the reflector and then a thin metallic film on the dielectric layer to obtain a close-to-unity thermal absorber/emitter [7]. In 2009, Sergeant *et. al* removed the periodicity constraint and use an aperiodic metal-dielectric stack as broadband thermal emitters [8]. It can be said that metallic films with thickness of the order of the skin depth, when arranged as a 1D stack, exhibit photonic effects which can be used to tailor the spectral absorbtivity/emissivity. However, very few researches have studied the physical principle of such devices.

Here, we propose an efficient multiband absorber comprising of a 1D planar stack made of silver (Ag) and silicon dioxide (SiO_2) on top of a silver substrate. By numerical and analytical calculation methods, we can obtain the absorbability higher than 90% at multiple wavelengths. We find that the number of the resonant peaks is related to the number of the Ag/ SiO_2 composite layers. Besides, our absorber shows the property of polarization insensitivity and angular insensitivity. The multi-resonance effect is due to the interaction between FP cavity modes distributed in different composite layers.

2. Structures and methods

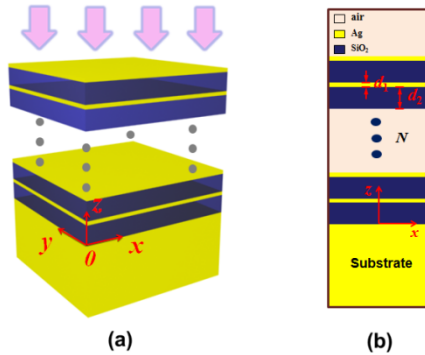


Fig. 1. Configuration of the proposed device.

Fig. 1 shows the 3D configuration and the cross section of the proposed absorber. The thicknesses of Ag and SiO_2 are $d_1 = 16 \text{ nm}$ and $d_2 = 80 \text{ nm}$, respectively. The refractive index of SiO_2 is set to 1.52 and that of silver is wavelength dependent as found in Ref. [9]. The silver substrate with 300 nm thickness can block all light transmission. So the absorption efficiency is $A = 1 - R$ (R represents the reflection efficiency). The number of the Ag/ SiO_2 composite layers on top of the silver substrate is defined as N . When $N = 1$, the structure is exactly the same as that in Ref. [7]. We simulate the structure in x - z plane using the Rigorous Coupled-wave Analysis (RCWA) method [10] as shown in Fig. 1b and arbitrary period along x direction is chosen for calculation. The incident plane wave has TE polarization with the electric field perpendicular to x - z plane (E_y) or TM polarization with the magnetic field H_y .

3. Results and discussions

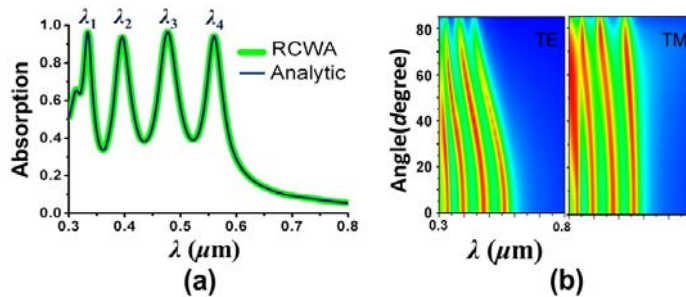


Fig. 2 (a) Absorption spectra for the proposed structure when $N = 4$ at normal incidence for TE/TM polarization. Thick: calculated by RCWA method. Thin: calculated by the analytic method based on characteristic matrix. (b-c) Map of angular absorption spectra for TE and TM polarization, respectively.

First, we take the structure when $N = 4$ as an example. Its absorption spectra at normal incidence for TE and TM polarizations are identical; see the thick line in Fig. 2a. This agrees very well with the analytical results based on the characteristic matrix method for analyzing the transmission/reflection efficiency of multilayer thin films [11]. Within the considered wavelength range of $[0.3, 0.8] \mu\text{m}$, we obtain four strong resonant peaks at $\lambda_1, \lambda_2, \lambda_3$ and λ_4 , for all of which the absorption efficiency is higher than 93%. We also study the cases at off-normal incidences and show the maps of angular absorption spectra for TE and TM polarization in Fig. 2b. It is seen that the four absorption peaks are retained very well for TM wave, while for TE wave the absorption peaks suffer some blue shift at large incident angles. Overall, we can say that our absorber is an omnidirectional, polarization-insensitive and multiband device.

In Ref. [7], it is pointed that Ag films work as reflective coatings while the SiO_2 insulator is employed to form the FP cavity for absorbing light. To know the principle of our multiband absorber, we study its field distributions of amplitude $|E_x|$ and phase $\Phi(E_x)$ for TM wave at normal incidence at the peaks of λ_1 , λ_2 , λ_3 and λ_4 , respectively; see

Fig. 3a and 3b. In Fig. 3a, one sees that the fields are concentrated at different layers at different wavelengths. Fig. 3b shows that the fields in the four composite layers have different phase distributions at different wavelengths. If we use the sign ‘+’ to represent a phase close to $\pi/2$ and the sign ‘-’ to represent a phase close to $-\pi/2$. The phase distributions in the four composite layers at $\lambda_1\text{--}\lambda_4$ can be represented by ‘+ - + -’, ‘+ - - +’, ‘+ + - -’, and ‘+ + + +’, respectively (as labeled in Fig. 3b). This is a typical hybridization effect of cavity resonances [12]. It is also expected to explain the multiresonance effect of our absorber by the analytical formula based on the characteristic matrix method.

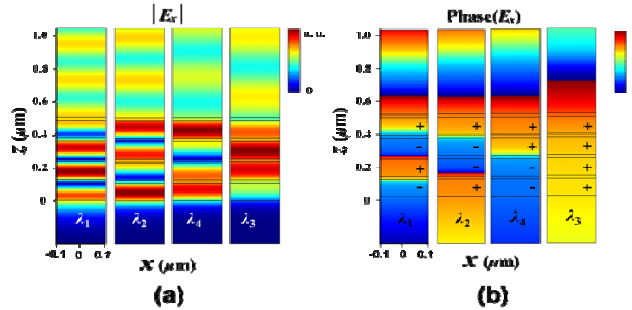


Fig. 3. Distributions of magnetic field $|E_x|$ and phase $\Phi(E_x)$ for the absorption peaks of λ_1 , λ_2 , λ_3 , and λ_4 as labeled in Fig. 1a. Signs of ‘+’ and ‘-’ in (b) represent the phase states close to $\pi/2$ and $-\pi/2$, respectively.

Next, we investigate the absorption spectra at normal incidence of our structure when the number of Ag/SiO₂ composite layer (N) is tuned from 1 to 8. It is seen clearly that the number of peaks is increased gradually when N is increased. For example, there are eight distinct absorption peaks when $N = 8$. Except that the 8th peak close to 0.6 μm is a bit lower, all other seven peaks have considerable absorption efficiency.

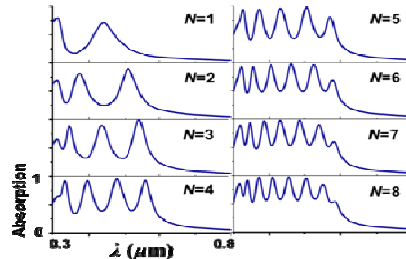


Fig. 4. Absorption spectra of the proposed structure when N is tuned from 1 to 8.

4. Conclusions

To sum up, we have proposed an omnidirectional, polarization-insensitive and multiband thin absorber in the visible regime by placing a stack of Ag/SiO₂ multilayers on top of a silver substrate. The comprehensive study and experimental work is going on. This work is supported by the NSFC of China (No. 11204205), Natural Foundation of Shanxi (No. 2012011020-4), and Special Foundation of Taiyuan University of Technology (No. 2012L033).

References

- [1] C. M. Watts, X. Liu, *et. al* Advanced Materials **24**, OP98-OP120 (2012).
- [2] N. I. Landy, S. Sajuyigbe, *et. al* Phys. Rev. Lett. **100**, 207402 (2008).
- [3] N. Bonod, G. Tayeb, *et. al* Opt. Express **16**, 15431-15438 (2008).
- [4] J. Sun, L. Liu, G. Dong, *et. al* Opt. Express **19**, 21155-21162 (2011).
- [5] Y. Cui, K. H. Fung, *et. al* Nano Letters **12**, 1443-1447 (2012).
- [6] A. Narayanaswamy, and G. Chen, *et. al* Phys. Rev. B **70**, 125101 (2004).
- [7] B. J. Lee, and Z. M. Zhang, *et. al* J. Appl. Phys. **100**, 063529 (2006).
- [8] N. P. Sergeant, M. Agrawal, *et. al* Opt. Express **18**, 5525-5540 (2010).
- [9] E. D. Palik, Handbook of Optical Constants of Solids (Academic Press, New York 1998).
- [10] M. G. Moharam, and T. K. Gaylord, J. Opt. Soc. Am. A **3**, 1780 (1986).
- [11] M. Born and E. Wolf, Principles of Optics, 7th edition (Cambridge University Press, Cambridge, UK 1999).
- [12] Y. Cui, K. H. Fung, *et. al* Opt. Express **20**, 17552-17559 (2012)

Thin film a-Si Solar Cells combining with nanodome antireflection structure and silver back reflector

Xiu Wu, Yumin Liu, Zhongyuan Yu, Zhihui Chen, Chengjie Wu

State Key Laboratory of Information Photonics and Optical Communications, Beijing University of Posts and

Telecommunications, P.O. Box 49, Beijing 100876, China

microliuyumin@hotmail.com

Abstract: We use FEM to analyze performance of the solar cell combining with nanodome antireflection structure and silver back reflector. Optimization is carried out and an optimal structure with short circuit current in 21.9016mA/cm^2 is obtained.

OCIS codes: (350.6050) Solar Energy; (310.1210) Antireflection coatings; (250.5403) Plasmonics.

1. Introduction

Recently, developing high performance light trapping in thin film solar cell attract a lot of attention. Among these light trapping methods, back reflector, antireflection layer and Surface plasmons structure have been researched in depth [1-3]. The light harvesting mechanisms of them are increasing backward light reflection, decreasing forward light reflection, and enhancing electromagnetic (EM) field at the surface of metal when incident light meets the specific irradiation conditions. In this paper, we combine the nanodome antireflection structure with silver back reflector in a a-Si solar cell. We employ finite element method (FEM) to simulate the EM field distribution basing on which short circuit current is calculated. Considering the influence of the nanodome geometric parameters on the performance of the solar cell, we meticulously tune the nanodome width and height and obtain a optimal structure with nanodome width in 180nm, height in 110nm and short circuit current in 21.9016mA/cm^2 (normal incident). We illustrate the quantum efficiency spectrum and analyze the enhancing mechanisms of the optimal structure comparing with the reference structure (flat solar cell without nanodome). The influence of the incident angle is also considered.

2. Physical model and numerical method

Figure 1 illustrates one period of the cross-sectional view of solar cell structure under study. On top of the solar cell is a 20nm thick indium tin oxide (ITO) roof film with b in width, and T in height acting as a top transparent electrode. The bottom electrode is a 50nm thick flat silver back-contact. Between the ITO roof and the silver back-contact is sandwiched with a-Si whose thickness is 130nm. The refractive index of ITO is set at 1.7 and the refractive index of Ag and a-Si are the experimental data in [4]. We set the periodic boundary condition along x direction and perfect electric conductor boundary condition at the bottom of the y direction. Short circuit current is calculated by:

$$J_{sc} = \frac{q}{hc} \int \lambda QE(\lambda) S(\lambda) d\lambda \quad (1)$$

Where q is elementary charge, h is Planck constant, c is the speed of light, λ is wavelength, QE is quantum efficiency which is defined as the ratio of the collected charge carriers and the number of input photons of a given energy, and S is the weighted sun spectrum (AM 1.5 spectral irradiance). To match the solar spectrum to a-Si absorption, a wavelength range from 330nm to 880 is considered.

3. Results and discussion

Figure 2 illustrates the result of nanodome optimization. For a 130nm thick a-Si layer with a flat silver back-contact, we sweep the nanodome width from 150nm to 200nm with an interval in 5nm and the nanodome height from 70nm to 130nm with an interval in 5nm. The short circuit currents for various geometric parameters are mapped in Fig.2 (a) and most of them are larger than $21\text{mA}/\text{cm}^2$. To observe the optimizing result perspicuously, the optimal nanodome height and maximum short circuit current are described as functions of nanodome width in Fig.2 (b). As figure 2 shown, the optimal nanodome structure has width in 180nm and height in 110nm , which promotes the short circuit current to $21.9016\text{mA}/\text{cm}^2$.

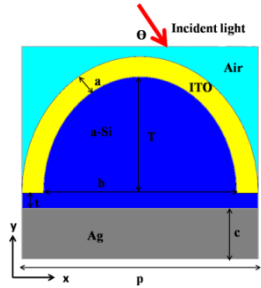


figure 1. The cross-sectional view of the structure under study.

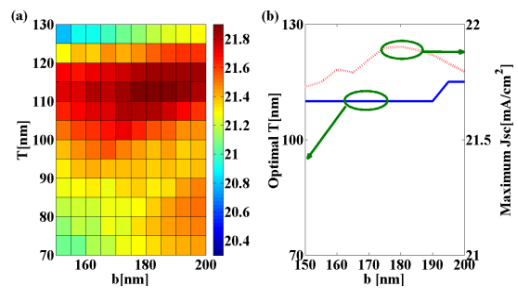


figure 2: short circuit current with different geometric parameters

To discuss the enhancement mechanisms of the roof structure, we illustrate the quantum efficiency spectrum for various structures including flat solar cell with 130nm thick active layer (blue dash line) and proposed structure (red solid line) under both TE (figure 3 (a)) and TM (figure 3 (b)) polarization. Three enhancements mechanisms can be identified in the whole wavelength range. The first enhancement is related to broadband antireflection effect caused by the gradually increasing effective refractive index from air to active layer, which mainly decreases the reflection at short wavelength range both in TE and TM polarization as figure 3 shows. Actually, while nanodome height increasing or nanodome width decreasing, spatial effective refractive index will changes more slowly and leads the impedance matching between the interfaces, which finally reduces the reflectivity and improve the quantum efficiency. The second enhancement derives from the blue shifted of Fabry-Perot absorption peak leading to a better matching with the solar spectrum. Figure 4 (a,b) illustrate the the electrical field amplitude distribution of solar cell with optimal roof structure at 710nm and 790nm in TE polarization condition. Comparing to figure 4(b), figure 4 (a) shows a much enhanced electrical field, which demonstrate the blue shift of FP resonance wavelength while changing flat structure to roof structure. Third enhancement originates from SPP resonance which happens only under TM polarization. For solar cell with optimal roof structure ($\text{RW}=180\text{nm}, \text{RH}=110\text{nm}$), nanaodome acting as not only antireflection layer but also diffraction grating which stimulates SPP resonance, increases the quantum efficiency at most wavelength under TM polarization compared with TE polarization and producs a absorption peak at 860nm (as figure 3(b) shows). Figure 4 (c,d) show the magnetic-field distribution of solar cell with optimal roof structure at 700nm and 860nm in TM polarization. In figure 4 (c), one can see not only a intense cavity mode in the active layer but also a infirm SPP mode distributing along the metal surface, which means that the enhancement at 700nm is a maxture of FP resonance and SPP mode. Figure 4 (d) shows intense magnetic-field profile along the metal surface revealing that the root of enhancement at 860 in TM polarization is SPP resonance.

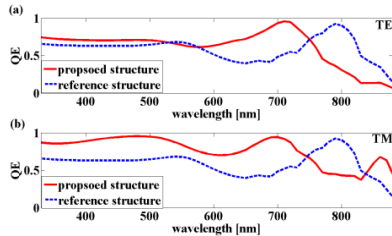


figure 3. Quantum efficiency spectrum for various structures

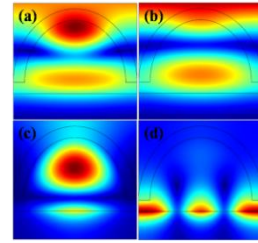


figure 4 . Simulated EM filed of proposed solar cell structure

Further research is done to consider the influence of the incident angle to the short circuit current, which is compared with flat solar cell with 130nm thick active layer (as figure 5 shows).The result is illustrated in figure 5. When incident angle is 90 degree (normal incident), short circuit current is enhanced compared to flat solar cell under both TE and TM polarization. however, when incident angle is larger or smaller than 90 degree, short circuit current is weaken under TE polarization (red dash line) and enhanced under TM polarization (red solid line). It's worth mentioning that short circuit current enhancement factor under TM polarization is much larger than the attenuation factor under TE polarization, which means the superiority of the proposed solar cell under unpolarized illumination (black dotted line) can be maintained for all incident angles. An average enhancement approaching to 7.38% is obtained for angles varying from 0 degree to 180 degree.

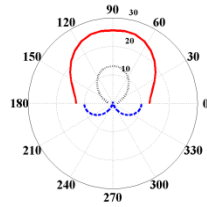


figure 5. short circuit current enhancement as a function of the angle of incidence.

4. Summary

We use finite element method to analyze performance of the solar cell combining with nanodome antireflection structure and silver back reflector. Optimization is carried out and a optimal structure with short circuit current in 21.9016mA/cm^2 is obtained. The influence of the incident angle is also considered. Compared with the flat solar cell with active layer in 130nm, an average enhancement approaching to 7.38% is obtained for angles varying from 0 degree to 180 degree.

Acknowledgements

This work was supported by the National Natural Science Foundation of China (Grant Nos. 60908028, 60971068, 10979065, and 61275201), and the Program for the New Century Excellent Talents in University (Grant No. NCET-10-0261) and the Chinese University Scientific Fund (Grant No.2011RC0402).

Reference

- Guozhen Yue, Laura Sivec, Jessica M.Owens, BaoJie Yan, Jeffrey Yang, and Subhendu Guha, "Optimization of back reflector for high efficiency hydrogenated nanocrystalline silicon solar cells," *Appl. Phys. Lett.* **95**, 263501(2009).
- Jia Zhu, Zongfu Yu, George F. Burkhard, Ching-Mei Hsu, Stephen T. Connor, Yueqin Xu, Qi Wang, Michael McGehee, Shanhui Fan, and Yi Cui, "Optical Absorption Enhancement in Amorphous Silicon Nanowire and Nanocone Arrays," *Nano. Lett.* **9**(1), 279-282(2009).
- Ricky B. Dunbar, Thomas Pfadler, and Lukas Schmidt-Mende, "Highly absorbing solar cells—a survey of plasmonic nanostructures," *Opt. Express* **20**(S2), A177-A189 (2012).
- David F. Edwards, "amorphous silicon (a-Si)" in *Handbook of optical constants of solids*, E.D. Palik, ed. (Academic, Orlando, Fla. 1985).

Detailed Study of Different CuInSe₂ Nanocrystal Shapes and Their Effect on the Photocurrent Response of Dye-Sensitized Solar Cells

Ramy Nashed^{a,b,*}, Ahmed Aziz^b, Ahmed Shehata^b, Ahmed I. Abdel-Salam^b, Mona B. Mohamed^c

^a Renewable Energy Laboratory, American University in Cairo, AUC Avenue, P.O. Box 74, New Cairo 11835, Egypt
e-mail address: ramy.nashed@aucegypt.edu

^bCharacterization Lab, Nanotech Egypt for Photo-Electronics, Dreamland, 6th October City, Egypt

^cNational Institute of Laser Enhanced Science (NILES), Cairo University, Giza, Egypt

Abstract: The effect of CuInSe₂ (CIS) nanocrystal shape, incorporated with the electrolyte solution, was investigated. CIS nanoflowers give the best performance when both conversion efficiency and photocurrent response are taken into account.

OCIS codes: (160.4236) Nanomaterials; (160.6000) Semiconductor materials

1. Introduction

The demand on energy is now increasing at an unprecedented rate due to the high technology revolution. The current energy sources are unable to cope with this increasing energy demand and hence new sources of energy need to be investigated. Solar energy is a very promising solution since the amount of solar energy reaching the earth is four orders of magnitude greater than the current world's energy consumption [1]. Also it is very clean and renewable. However, the cost of solar energy is still very expensive which prevents it from being widely spread. About 50% of the solar cell cost comes from the material [2] and hence cheap materials are needed in order for solar energy to be widely implemented.

Dye-Sensitized Solar Cells (DSSCs) are a promising solar cell structure due to their simple fabrication process, low cost, and a reasonable efficiency of about 11% [3]. However, the maximum current that can be extracted from the cell decreases exponentially with time due to the high resistance that the iodide ions suffer in the viscous electrolyte medium which decreases the reduction rate of the electrons at the counter electrode [4]. We have previously shown that introducing CuInSe₂ (CIS) quantum dots with the electrolyte enhances the photocurrent response and leads to a nearly constant electric current over time [5]. This is due to the high hole mobility in CIS which increases the overall mobility in the CIS/electrolyte blend. It was shown previously that the physical and chemical properties of the nanostructures largely depend on their shapes [6]. In this work, we study the effect of the nanocrystal shape on the photocurrent response of DSSCs.

2. Results and Discussion

We have synthesized CIS quantum dots, nanorods, and nanoflowers using only commercial salts of Cu, In, selenium powder, trioctylphosphine, and oleyl amine on the basis of the procedure reported by Tang et al [7]. Our synthesis marks an advance for chalcopyrite nanomaterial solar cells and offers a possible template for the synthesis of other ternary and quaternary nanomaterials. Figure 1 shows the TEM images of the prepared nanostructures. It is clear that the nanoflowers are more uniformly distributed all over the sample and form a well-interconnected network compared to quantum dots and nanorods.

A reference solar cell is fabricated without the incorporation of CIS layer to which we compare the performance of the solar cells after adding the CIS layer. Figure 2 illustrates the schematic diagram of the reference as well as the proposed cell. It is based on natural dye (hibiscus) due to its low cost despite its low efficiency. However, this is justified since the main goal here is to study the photocurrent response and not to improve the efficiency. As pointed out in our previous work, adding the CIS layer before the dye degrades the performance considerably and so the dye is added before incorporating the CIS layer [5].

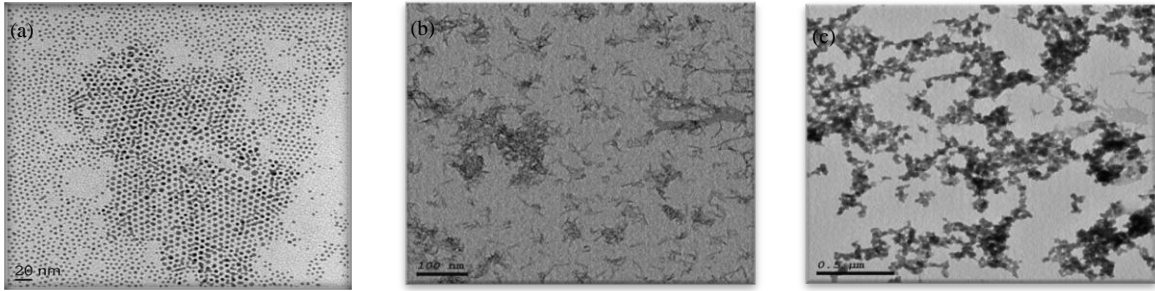


Figure 1: TEM images of CIS (a) quantum dots, (b) nanorods, (c) nanoflowers

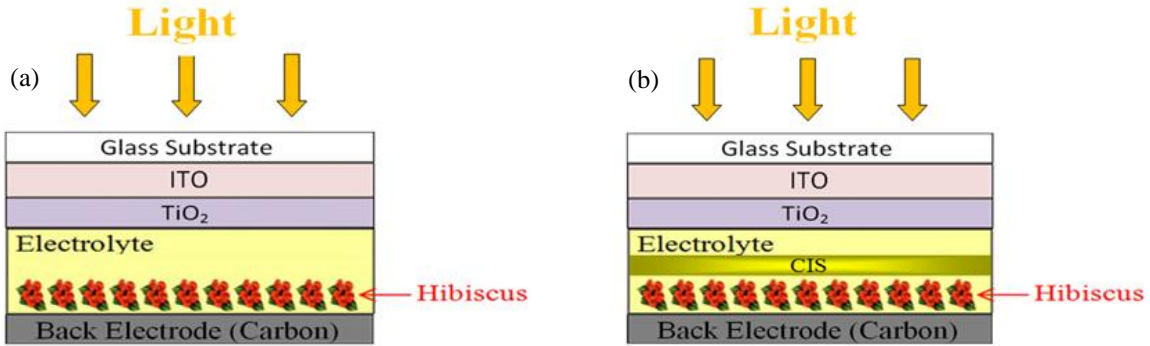


Figure 2: Schematic diagram of (a) reference cell, (b) proposed structure with CIS layer

Figure 3 shows the I-V curve of the solar cells before and after incorporation of CIS. The short circuit current of the reference cell is $2309 \mu\text{A}$, its open circuit voltage is 480 mV , and its fill factor is 0.25. This leads to an efficiency of $50 \times 10^{-3} \%$. For the solar cell containing CIS quantum dots, the short circuit current drops by about 50% to $1244 \mu\text{A}$, but the open circuit voltage and the fill factor increases to 500 mV and 0.26 respectively, which compensate the reduction in the short circuit current and give an efficiency of $35 \times 10^{-3} \%$. The CIS nanoflowers show a short circuit current of $1200 \mu\text{A}$, which is very close to that obtained from the quantum dots. The open circuit voltage drops to nearly 460 mV but the fill factor rises to 0.32, leading to an efficiency of $32 \times 10^{-3} \%$. On the other hand, the nanorods did not give a good performance with a short circuit current of $380 \mu\text{A}$, an open circuit voltage of 130 mV , a fill factor of 0.24, and an efficiency of $2.2 \times 10^{-3} \%$, which is one order of magnitude lower than the other fabricated cells.

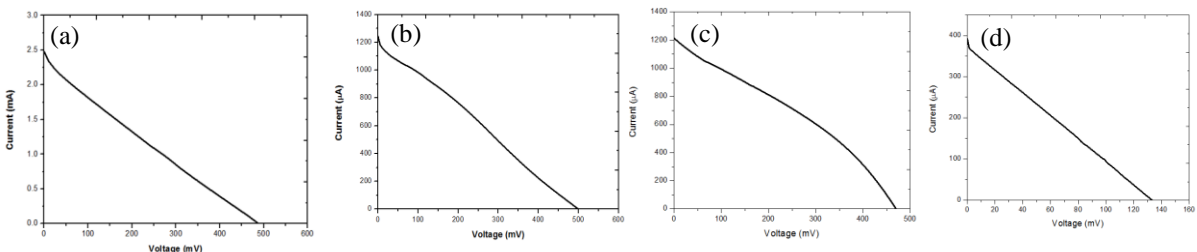


Figure 3: I-V curve of (a) reference cell, (b) solar cell with CIS quantum dots, (c) solar cell with CIS nanoflowers, and (d) solar cell with CIS nanorods

The photocurrent response for the fabricated solar cells is shown in Figure 4. Note that the settling time for the reference cell is more than 17 seconds. Adding CIS nanocrystals enhanced the response considerably. CIS quantum dots reduce the settling time to 150 milliseconds. CIS nanoflowers further reduce the settling time to 50 milliseconds and CIS nanorods gives the smallest settling time of 48 milliseconds. However, incorporating CIS nanorods leads to very low conversion efficiency, as shown in

Figure 3. Taking both the conversion efficiency and the photocurrent response into account, we arrive at the conclusion that CIS nanoflowers give the best performance. This is because the nanoflowers are uniformly distributed and highly interconnected throughout the whole sample, as shown in Figure 1. This provides a continuous path for the charge carriers between the dye and the back electrode. Table 1 summarizes the different figures of merit of the fabricated solar cells.

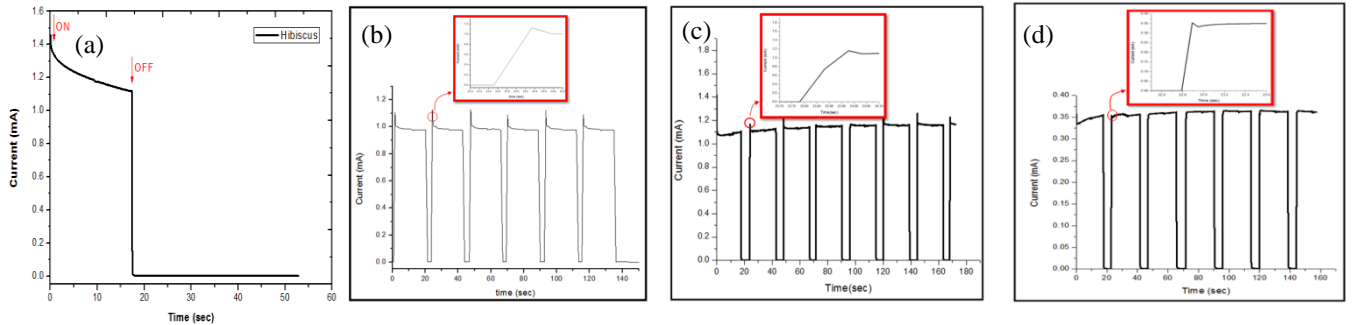


Figure 4: Photocurrent response of (a) reference cell, (b) solar cell with CIS quantum dots, (c) solar cell with CIS nanoflowers, (d) solar cell with CIS nanorods

Table 1: Comparison of the photovoltaic figures of merit for the fabricated CIS-based DSSCs as well as the reference cell

	Reference Cell	CIS quantum dot	CIS nanoflower	CIS nanorod
Isc (μ A)	2309	1244	1200	380
Voc (mV)	480	500	460	130
FF	0.25	0.26	0.32	0.24
$\eta\%$	50×10^{-3}	35×10^{-3}	32×10^{-3}	2.2×10^{-3}
Settling time (ms)	> 17000	150	50	48

Conclusion

The effect of CIS nanocrystal shape, which was added to the electrolyte-dye network, was investigated. It was shown that CIS nanorods has the best photocurrent response, however, the conversion efficiency is very low. CIS nanoflowers have the best performance when considering both conversion efficiency and photocurrent response.

References

- [1] N. S. Lewis, "Powering the Planet", MRS Bulletin, **32**, 808-820 (2007).
- [2] V. E. Ferry, J. N. Munday, and H. A. Atwater, "Design Considerations for Plasmonic Photovoltaics", Adv. Mater., **22**, 4794-4808 (2010).
- [3] M. A. Green, K. Emery, Y. Hishikawa, W. Warta, and E. D. Dunlop, "Solar cell efficiency tables (version 39)", Prog. Photovolt: Res. Appl., **20**, 12–20 (2012).
- [4] S. Ito, S. M. Zakeeruddin, R. Humphry-Baker, P. Liska, R. Charvet, P. Comte, M. K. Nazeeruddin, P. Pechy, M. Takata, H. Miura, S. Uchida, and M. Grätzel, "High-Efficiency Organic-Dye-Sensitized Solar Cells Controlled by Nanocrystalline-TiO₂ Electrode Thickness", Adv. Mater., **18**, 1202 (2006).
- [5] R. Nashed, E. Grgis, A. Shehata, A. I. Abdel-Salam, M. B. Mohamed, "Remarkable Enhancement of the Photocurrent Response of Dye-Sensitized Solar Cells using CuInSe₂ Nanocrystals", Accepted at Asian Communications and Photonics Conference (ACP), 2012.
- [6] M. T. Ng, C. B. Boothroyd, and J. J. Vittal, "One-Pot Synthesis of New-Phase AgInSe Nanorods", J. Am. Chem. Soc., **128**, 7118-7119 (2006)
- [7] X. Xin, M. He, W. Han, J. Jung, Z. Lin, "Low-cost CZTS counter electrodes for high-efficiency dye sensitized solar cells", Angew. Chem. Int. Ed., **50**, 2 (2011)

Investigation on the exciplex and electroplex based on 2-(4-trifluoromethyl-2-hydroxyphenyl)benzothiazole] zinc as donor or acceptor

Jingcheng Song^{a, b}, Wenyan Wang^{a, b}, Zhengfu Yan^{a, b}, Yuying Hao^{a, b*}, Yanxia Cui^{a, b}, Ting Ji^{a, b}

^aCollege of Physics and Optoelectronics, Taiyuan University of Technology, Taiyuan 030024, China

^bKey Lab of Advanced Transducers and Intelligent Control System, Ministry of Education, Taiyuan University of Technology, Taiyuan 030024, China

*haoyuying@tyut.edu.cn

Abstract: The electroplex or exciplex between 2-(4-trifluoromethyl-2-hydroxyphenyl)benzothiazole] zinc [Zn(4-TfmBTZ)₂] and several charge transport materials is investigated. This investigation is significant for utilizing effectively Zn(4-TfmBTZ)₂ in monochromatic or white organic light-emitting diode (OLED) design.

OCIS codes: (230.3670) organic Light-emitting diodes; (160.2100) Electro-optical materials

1. Introduction

Organic light-emitting diodes (OLEDs) have been widely studied due to their potential applications. In most OLEDs, the electroluminescence (EL) is from the radiative decay of molecular excited states, namely excitons. But the emissions of bimolecular excited state species, such as exciplex and electroplex, are often observed in some hetero-junction OLEDs. The electroplex emission is visible mostly under electric-excitation and not normally under photo-excitation, but exciplex emission is readily observed in both EL and photoluminescence (PL) processes. The bimolecular excited state species usually lead to an additional red-shifted broad band emission [1, 2]. In monochromatic OLED, the bimolecular species ought to be avoided for good color purity [3]. Contrarily, the bimolecular emission becomes an important technology to design white OLED [4, 5].

It is well known that bis(2-(2-hydroxyphenyl)benzothiazolate)zinc (Zn(BTZ)₂) can be used as an effective white light emission and electron transport material in EL device [6, 7]. 2-(4-trifluoromethyl-2-hydroxyphenyl) benzothiazole] zinc [Zn(4-TfmBTZ)₂] [8, 9], a derivative of Zn(BTZ)₂, one additional electron-withdrawing group trifluoromethyl incorporating in 4-position of BTZ, is a very interesting blue emission material. In this paper, the exciplex or electroplex between Zn(4-TfmBTZ)₂ and several charge transport materials was investigated. This investigation is significant for utilizing effectively Zn(4-TfmBTZ)₂ in monochromatic or white OLED design.

2. Experimental

The OLEDs are prepared by thermal evaporation of different organic layers onto patterned, precleaned and ultraviolet ozone treated indium tin oxide (ITO) coated glass substrates in an vacuum system at a base pressure of 4.0×10^{-4} Pa without breaking vacuum. The EL spectra were obtained by FR-655. The PL spectra of organic films deposited on quartz substrates were measured by F280 fluorescence spectrophotometer.

3. Results and Discussions

3.1 Electroplex at HTL / Zn(4-TfmBTZ)₂ interface

The electroplex between Zn(4-TfmBTZ)₂ and N,N'-diphenyl- N,N'-bis(1-naphthyl)-

(1,1'-biphenyl)-4,4'-diamine (NPB) had been studied [8, 9]. There the device of ITO/NPB (60nm)/Zn(4-TfmBTZ)₂ (30nm)/BCP(10nm)/Alq₃ (30nm)/ LiF (1.0nm) /Al (150nm) was designed, where BCP (2,9-dimethyl-4,7-diphenyl-1,10-phenanthroline) was used as a hole-blocking layer, 8-hydroxyquinoline aluminum (Alq₃) as electron transport layer. The dependence of EL spectra on voltage is shown in Fig.1(a). The peak at 460nm is associated with NPB exciton emission. While the peak at 580nm is attributed to the electroplex emission between Zn(4-TfmBTZ)₂ and NPB, because the exciplex and charge transfer complex emission had been excluded by UV-visible absorption spectra and PL spectra [8]. The electroplex is a cross transition recombination between electrons blocked on LUMOs of Zn(4-TfmBTZ)₂ and holes blocked on HOMOs of NPB, as shown in Fig.3(b). When 1,1-bis[(di-4-tolylamino)phenyl]cyclohexane (TAPC) with higher LUMO level of 2.0eV relative to NPB was used instead of NPB, the electrons are blocked and accumulated on LUMO level of Zn(4-TfmBTZ)₂ [see Fig.3(b)], the only electroplex emission at 586nm, a cross transition between Zn(4-TfmBTZ)₂ and TAPC is observed at 4V, as shown in Fig.1(b). Of course, the exciton emission of Zn(4-TfmBTZ)₂ at 474nm is visible with the increasing voltage. The electroplex and exciton emission compete with each other. The electroplex emission at low electric-field is relatively favorable while the exciton emissions are facilitated at high electric-field. The electroplex emission is slightly blue-shifted with increasing drive-voltage.

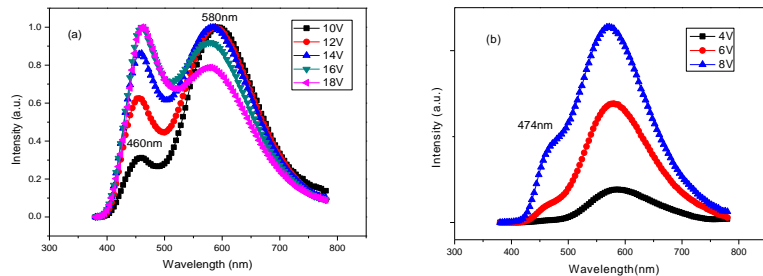


Fig.1(a) The EL spectra of (a) ITO/NPB(60nm)/Zn(4-TfmBTZ)₂(30nm)/BCP(10nm)/Alq₃(30nm)/LiF(1.0nm) /Al(150nm); (b)ITO/TAPC (30nm)/ Zn (4-TfmBTZ)2(30nm)/ /LiF(1.8nm)/Al(150nm) at different voltage

3.2 Exciplex at Zn(4-TfmBTZ)₂ / ETL interface

In order to eliminate the electroplex at NPB/Zn(4-TfmBTZ)₂ interface, the device of ITO/NPB(40nm)/[Zn(4-TfmBTZ)₂8wt%:mcp](30nm)/Bphen(40nm)/LiF(1nm)/Al(200nm) was designed, where the 4, 7 – diphenyl - 1, 10-phenanthroline (Bphen) was used as electron transport material, (N, N'-dicarbazoyl-3,5-benzene (mcp) as host material. The doping concentration of Zn(4-TfmBTZ)₂ was fixed 8wt%. The EL spectra are shown in Fig. 2(a). Unexpectedly, a new broad band at 621nm is observed. In order to confirm its origin, 1,3,5-Tri(1-phenyl-1H-benzo[d]imidazol-2-yl)phenyl (TPBi) as electron transport material was used instead of Bphen, the corresponding EL spectrum is displayed in Fig.2.(b). The intrinsic emission of Zn(4-TfmBTZ)₂ at 461nm, being in agreement with the emission of Zn(4-TfmBTZ)₂ in THF [8], is obtained. Therefore, the emission of 621nm is originated from the [Zn(4-TfmBTZ)₂ 8wt%:mcp]/Bphen interface. Nevertheless, the peak of 621nm disappear in no doping device of ITO/NPB(40nm)/mcp(30nm)/Bphen(40nm)/LiF(1nm)/Al(200nm). So the emission of 621nm is suggested from Zn(4-TfmBTZ)₂ /Bphen interface emission. In order to confirm further its nature, the PL spectra of Bphen, Zn(4-TfmBTZ)₂, Bphen:Zn(4-TfmBTZ)₂ (weight ratio of 1:1) films were measured, as shown in Fig.3. In mixture film of Bphen : Zn(4-TfmBTZ)₂, a new and broad band

peaked at 582nm accompanied by shoulder peak at 618nm is observed. So the emission of 621nm is identified as the emission of the exciplex $[\text{Zn}(4\text{-TfmBTZ})_2 \text{Bphen}^*]$ [see Fig.3(b)] .

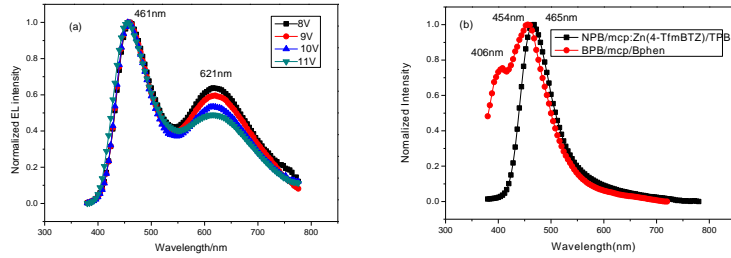


Fig.2. EL spectra of (a)ITO/NPB/[Zn(4-TfmBTZ)₂]8%:mcp]/Bphen/LiF/Al; (b) ITO/NPB(40nm)/ [Zn(4-TfmBTZ)₂]8%:mcp](30nm)/TPBi(40nm)/LiF(1nm)/Al(200nm)(black line) and ITO/NPB(40nm)/mcp(30nm)/ Bphen (40nm)/LiF(1nm)/Al (200nm)(red line)

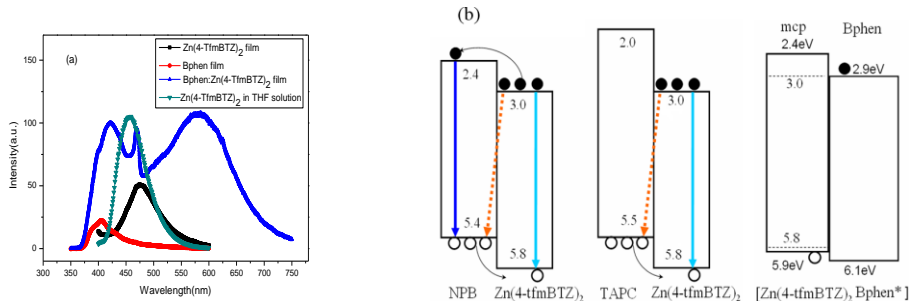


Fig.3 (a) PL spectra of Bphen, Zn(4-TfmBTZ)₂, Bphen:Zn(4-TfmBTZ)₂ film and Zn(4-TfmBTZ)₂ in THF solution with concentration of 10^{-5}M [8]; (b) Energy band diagram of organic materials used in this studies

4. Conclusion

2-(4- trifluoromethyl-2-hydroxyphenyl) benzothiazole zinc $[\text{Zn}(4\text{-TfmBTZ})_2]$ is a very novel blue emission materials. The electropolex or exiplex between $\text{Zn}(4\text{-TfmBTZ})_2$ and several charge transport materials is identified. This investigation is significant for utilizing effectively $\text{Zn}(4\text{-TfmBTZ})_2$ in monochromatic or white OLED design.

Acknowledgements

This work is financially supported from National Natural Scientific Foundation of China (60976018, 61274056, 11204205, 11204202), Natural Foundation of Shanxi (2012011020-4)

Reference

- [1] J. Kalinowski, Mater. Sci.-Poland 27(2009)735.
- [2] M. Cocchi, D. Virgili, C. Sabatini, J. Kalinowski, Chem. Phys. Lett. 421(2006) 351
- [3] Z. Hong, C. Liang, R. Li, W. Li, D. Zhao, D. Fan, D. Wang, B. Chu, F. Zang, L.S. Hong and S.T. Lee, Adv. Mater. (Weinheim, Ger.)131(2001)241.
- [4] E. L. Williams, K. Haavisto, J. Li, and G. E. Jabbour, Adv. Mater. (Weinheim, Ger.) 19(2007)197 .
- [5] M. Cocchi, J. Kalinowski, L. Murphy, J.A. Gareth Williams, V. Fattori, Org. Electron. 11 (2010) 388
- [6] Y. Hamada, T. Sano, H. Fujii, Y. Nishio, H. Takahashi, and K. Shibata, Jpn. J. Appl. Phys., part 1, 35 (1996)1339
- [7] G. Yu, S. Yin, Z. Shuai, D. Zhu, J. Am. Chem. Soc.123(2003)14816
- [8] Y.Y. Hao, W.X. Meng, H. X. Xu , H. Wang, X. G. Liu , B. S. Xu, Org. Electron. 12(2011) 136
- [9] Y. Zhang, W.X. Meng, Y.Y. Hao, H. X. Xu , H. Wang, B. S. Xu, Appl. Phys. A: Mater. Sci. Process, 106(2012)709

Quasicrystal metamaterials: a route to optical isotropy

S. Kruk¹, C. Helgert^{1,2}, M. Decker¹, I. Staude¹, C. Etrich², C. Menzel², C. Rockstuhl², C. Jagadish³, T. Pertsch², D. N. Neshev¹, and Yu. S. Kivshar¹

1. Nonlinear Physics Centre and Centre for Ultrahigh-bandwidth Devices for Optical Systems (CUDOS), Research School of Physics and Engineering, The Australian National University, Canberra, ACT 0200, Australia

2. Institute of Applied Physics, Abbe Center of Photonics, Friedrich-Schiller-Universität Jena, 07743 Jena, Germany

3. Department of Electronic Materials and Engineering, Research School of Physics and Engineering, The Australian National University, Canberra, ACT 0200, Australia
sergey.kruk@anu.edu.au

Abstract: We introduce a novel class of metamaterials with quasicrystalline meta-atom arrangements and study their properties in comparison with periodic and disordered metamaterials. We show that quasicrystalline metamaterials exhibit isotropic optical properties while preserving pronounced resonances.

OCIS codes: (160.3918) Metamaterials; (260.5430) Polarization; (310.6628) Subwavelength structures, nanostructures.

1. Introduction

The concept of metamaterials offers exceptional opportunities for creating artificial materials with virtually unlimited range of macroscopic properties, including such that are remarkably different from natural materials [1]. Optical metamaterials rely on the ability to fabricate nanoscale metal-dielectric particles of various shapes (*meta-atoms*) arranged in a specific pattern. This approach allows us to create at will composite metamaterials optimized for a desired operation and functionality. In recent years, it became evident that interactions between the single meta-atoms in the array play an important role for the metamaterial response [2]. Thus, the inherent arrangement of identical metal-dielectric nanoparticles affects the macroscopic optical properties of metamaterials. However, up to date most of the studies of various properties of metamaterials are based on a silent assumption that, similar to most solids in nature, the meta-atoms are composed in a *periodic lattice*. One of the main disadvantages of such an arrangement is the anisotropic response of the metamaterial for the case of oblique incidence of light. In order to obtain isotropic optical response, metamaterials with disordered arrangement of elements have been proposed [3, 4]. However, disorder increases scattering of the light dramatically, which reduces the resonant power of the structure.

In this letter we introduce a novel class of metamaterials with a quasicrystalline meta-atom arrangement. Such an arrangement has long-range positional *order*, but *no periodicity*. Therefore quasicrystalline metamaterials exhibit isotropic optical response in contrast to periodic metamaterials while preserving same level of scattering. The effect of the meta-atom interactions is measured by examining the extrinsic optical activity [5, 6] of the different metamaterials at the oblique incidence, which allow us to be only sensitive to the optical properties induced by the symmetry characteristics of the underlying lattice. As such, we reveal that qualitatively different optical properties of metamaterials can be achieved by controlling the geometry of their nanoparticle constituents and predict a novel type of metamaterials, *quasicrystalline metamaterials*.

2. Symmetry-dependent optical properties of metamaterials

In our experiments we utilize a magnetic optical metamaterial composed of meta-atoms consisting of two Au disks each 25 nm thin, separated by a 30 nm MgF₂ layer (Fig. 1a). The meta-atom has a circular symmetry with bottom diameter of 180 nm and weak tapering of 10°. The identical meta-atoms are placed on a glass substrate and arranged into three types of symmetries: periodic (and consequently ordered) [Fig. 1(b)], quasicrystalline (ordered, but non-periodic) [Fig. 1(c)], and disordered non-periodic array [Fig. 1(d)]. By comparing the properties of those three samples we can independently study the impact of both order and periodicity and emphasize the influence of the unique quasicrystalline arrangement.

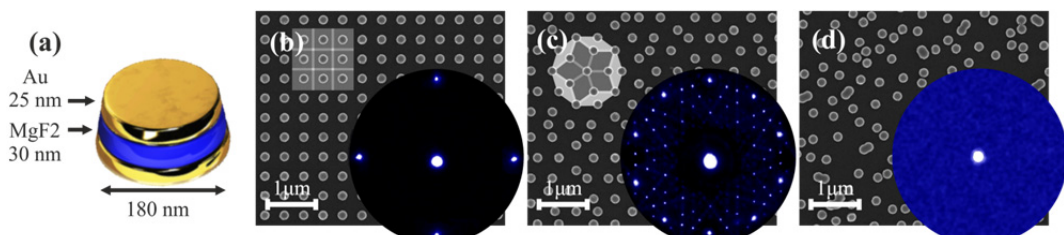


Fig. 1. (a) A single metamaterial magnetic atom; and scanning electron micrographs of (b) periodic, (c) quasicrystalline, and (d) disordered metamaterials. Inserts show the far-field diffraction patterns of the metamaterials obtained with a laser beam of 0.4 μm wavelength. The diffraction pattern of the quasicrystalline metamaterial shows the lack of long-range positional order, while the microscopic image of the elements show the absence of periodicity.

The impact of the *order* of meta-atom arrangement can be directly observed by comparing the strength of the resonances of our metamaterials. To precisely measure the impact of *periodicity* of meta-atoms arrangements we study the extrinsic optical chirality of the metamaterials. The extrinsic chirality of internally non-chiral object appears when the direction of propagation of light isn't parallel to any of the mirror planes of the object. In our case the single meta-atom is a disk, i.e. it has infinite number of mirror planes, therefore it cannot exhibit chirality by itself. However, the arrangement of the meta-atoms may still have a finite number of mirror planes. Therefore, by measuring chirality of our metamaterial, we observe the impact of the meta-atom arrangement only, regardless the impact of a single meta-atom.

To characterize chirality of the metamaterials we study the transmission of circular-polarized light at oblique incidence onto the sample. Fig. 2 shows the experimental setup and an example of mutual orientation of the light wave and the metamaterial, which gives rise to extrinsic chirality.

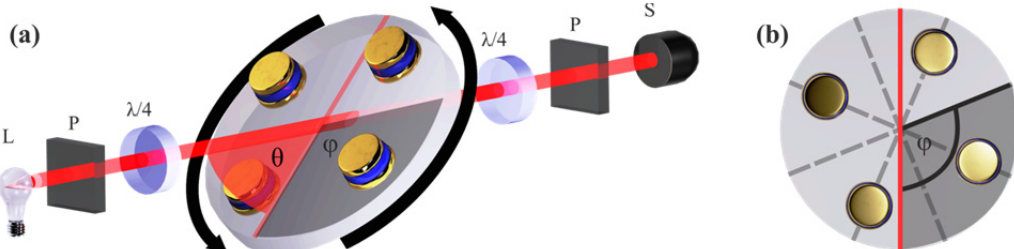


Fig. 2. (a) Experimental setup: white light source L, polarizers P, achromatic quarter-wave plates $\lambda/4$, and spectrometer S. Angle θ is measured in the plane of incidence of light, angle ϕ is measured in the sample plane. (b) Top view on the mirroring planes of the periodic metamaterial (dashed gray) with respect to the plane of incidence of light (red).

Top plots in Fig. 3 shows the transmission spectra of left-circularly polarized light for $\theta = 45^\circ$. Radial coordinates of each polar plot correspond to different wavelengths in the range 0.5-1.0 μm ; angular coordinates correspond to different ϕ angles. Next we examine chirality by calculating circular dichroism as the difference of amplitudes of transmitted left- and right-circularly polarized light: $[LCP_{amp} - RCP_{amp}] / [LCP_{amp} + RCP_{amp}]$, as shown in the bottom plots of Fig. 3. We observe that all three transmission spectra have two resonant lines: near 0.7 μm (electric dipole resonance) and near 0.95 μm (magnetic dipole resonance). We notice that the spectra of the metamaterials with ordered lattices are much sharper in comparison with the disordered metamaterial. We also observe that periodic metamaterial exhibits strong circular dichroism and therefore chirality for angles $\phi \neq \pi/4$, which is a result of interaction induced anisotropy. As one could expect, the disordered metamaterials shows no chirality. Most importantly, the quasicrystalline metamaterial shows no chirality and therefore strong isotropy.

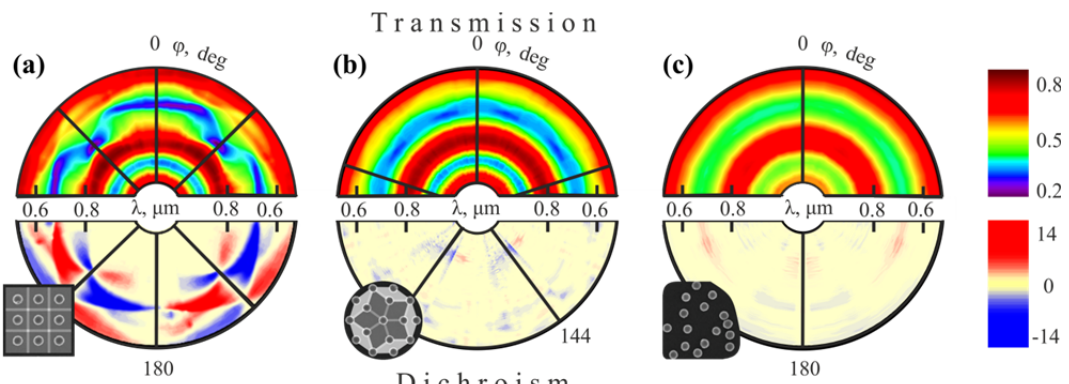


Fig. 3. Transmission of left-circularly polarized light (top plots) and circular dichroism (bottom plots) of (a) periodic metamaterial, (b) quasicrystalline metamaterial and (c) disordered metamaterial. Radial coordinates of each polar plot correspond to different wavelengths, angular coordinates correspond to different ϕ angles.

In conclusion, we have introduced the concept of quasicrystalline metamaterials and revealed that their unique symmetry leads to optical isotropy while preserving the resonance strength of the metamaterial.

References

1. C. M. Soukoulis and M. Wegener, "Past achievements and future challenges in the development of three-dimensional photonic metamaterials," *Nat. Photon.* **5**, 523-530 (2011).
2. M. Decker, S. Linden, and M. Wegener, "Coupling effects in low-symmetry planar split-ring resonator arrays," *Opt. Lett.* **34**, 1579 (2009).
3. C. Helgert, C. Rockstuhl, C. Etrich, C. Menzel, E. B. Kley, A. Tünnermann, F. Lederer, and T. Pertsch, "Effective properties of amorphous metamaterials," *Phys. Rev. B* **79**, 233107 (2009).
4. N. Papasimakis, et. al "Coherent and incoherent metamaterials and order-disorder transitions," *Phys. Rev. B* **80**, 041102 (2009).
5. M. Born and W. E., *Principles of Optics* (Pergamon Press, 1959).
6. E. Plum, V. A. Fedotov, and N. I. Zheludev, "Optical activity in extrinsically chiral metamaterial," *Appl. Phys. Lett.* **93**, 191911 (2008).

Gold nanoparticles embedded in flexible materials: new frontiers in Plasmonics

R. Caputo¹, U. Cataldi², Alastair Cunningham², L. De Sio¹, Thomas Bürgi² and C. Umeton¹

¹LICRYL (*Liquid Crystals Laboratory, IPCF-CNR*),
and
Center of Excellence CEMIF-CAL and Department of Physics
University of Calabria, 87036 Arcavacata di Rende (CS), Italy

²Département de Chimie Physique, Université de Genève, Quai Ernest-Ansermet 30, 1211 Genève, Switzerland.

roberto.caputo@fis.unical.it

Abstract: Fabrication of samples showing plasmonic properties is fundamental for the realization of devices that can exhibit peculiar electromagnetic properties. Here we illustrate results of experiments performed on systems with Au nanoparticles embedded in flexible substrates.

OCIS codes: (250.4503) Plasmonics; (310.6845) Thin film devices and applications; (250.0040) Detectors.

1. Introduction

Wide interest is actually devoted to the realization of materials showing Plasmonic properties. These materials are of great interest for many applications such as integrated optics [1], plasmonic circuits [2], biosensing [3] and quantum information processing [4]. Their unique properties derive from the collective oscillation of the free conduction electrons induced by the interaction with an external electromagnetic field, the so called Localized Surface Plasmon (LSP). The plasmonic behaviour of a system of metal nanoparticles (NPs) is usually shown by a very intense color, which is absent in the bulk material as well as in individual atoms. The control of plasmonic resonances is a hot-topic and can be enabled by changing size and shape of NPs or their distribution. In order to fabricate these materials, a possible choice is a top-down approach (e-beam or photo-lithography) but, due to the long processing times, the resulting useful area is way too small. A bottom-up approach is then preferable: NPs can be combined with host materials that have the ability to induce the self-organization of particles through chemical or physical mechanisms. In this case, the major effort is spent to design host materials that can exercise such an influence on NPs. In this paper, we report on our attempts to realize a system made of Au NPs embedded in an elastomeric support. There are several reasons why we chose such an approach. A first one is that an eventual device, being stretchable, should show tunable plasmonic features. Indeed, a stretching of the NP doped elastomer matrix should modify the relative distance between NPs and hence their electromagnetic coupling. Moreover, in case such prototype devices were successfully realized, its mass production should be straightforward: a master structure with the desired features would be easily replicated in the elastomer support. When elastomers are considered, polydimethylsiloxane (PDMS) is one of the most suitable. Indeed, it is widely used in optofluidic [5], photonic [6,7] and biomedical applications [8]. In the following, we will illustrate our attempts to fabricate a PDMS substrate doped with Au nanoparticles that can eventually be shaped as needed for obtaining a device with tunable plasmonic properties.

2. Samples preparation

In order to obtain samples showing reproducible properties, we tried to develop a fabrication protocol. The starting point for obtaining a PDMS material is a bi-component mixture made of a base pre-polymer and a curing agent. Depending on the relative concentration of these components, the elastomer can vary from a gel-like to an almost plastic hard consistency. The polymerised structure is obtained by baking the bi-component syrup in oven for some time. Both baking time and temperature influence the mechanical properties of the final structure. Combination of this material with gold or silver NPs is not trivial: indeed, when dealing with NPs, the hardest job is to prevent their clustering. Indeed, the plasmonic resonance frequency of metal particles strongly depends on their size and on the dielectric features of the host material containing them [9]. For this reason, we first diluted Au NPs (from Harima Chemicals) in chloroform, stirred them for about one hour and then verified their good dispersion by scanning

electron microscopy (SEM). Next step is to mix Au NPs diluted in chloroform with PDMS. There are, at least, three possible ways to proceed: they can be directly combined with the base pre-polymer, with the curing agent or with the two components previously mixed together. At first we thought that the very low viscosity of the curing agent should improve its miscibility with Au NPs. Unfortunately, this hypothesis was not correct: after a short time (about 1 hour), NPs phase separated from the curing agent. First of all, we combined NPs with the base pre-polymer. Then the curing agent has been added to the base pre-polymer doped with NPs. The samples used for experiments have been prepared by following the steps depicted in Fig. 1. Instead of preparing a homogenous substrate made of PDMS doped with NPs, we preferred to limit the presence of this material just to a thin volume. In order to obtain such a result, we glued a glass substrate (1x2cm², 1.1mm thick) to the bottom of a petri dish (Fig. 1a) and then we poured a pure PDMS mixture (curing agent/base pre-polymer in 1/10 weight ratio) in it (Fig. 1b,c). Afterwards, the petri dish has been baked in the oven (previously warmed up at 100°C, Fig. 1d) for about one hour. After the baking step, the hardened PDMS substrate can be just peeled off from the petri dish (Fig. 1e). The obtained sample contains a hollow volume corresponding to that occupied by the glass substrate glued in the Petri dish. We filled in this volume with a second mixture made of PDMS (same ratio between the two components) and Harima at 1wt%, prepared as explained above. It is worth noting that the commercial product from Harima (NPG-J) that we used for our experiments contains an effective 56wt% concentration of Au nanoparticles. As such, the real concentration of Au NPs in our samples corresponds to 0.56wt%. The PDMS sample, including now Au NPs, has been additionally baked at 200°C for about one hour. At the end of the process, we obtained ~2mm of thickness PDMS layer that contains a thin layer (about 100μm thick) of PDMS doped with Au NPs (Fig. 1f). The choice of limiting the presence of NPs to a small volume of the sample is due to the fact that, by fabricating a thick layer of PDMS homogeneously doped with NPs, even with low gold concentrations, the extinction coefficient of the sample would be way too high, making difficult a reliable study of the plasmonic response of the system.

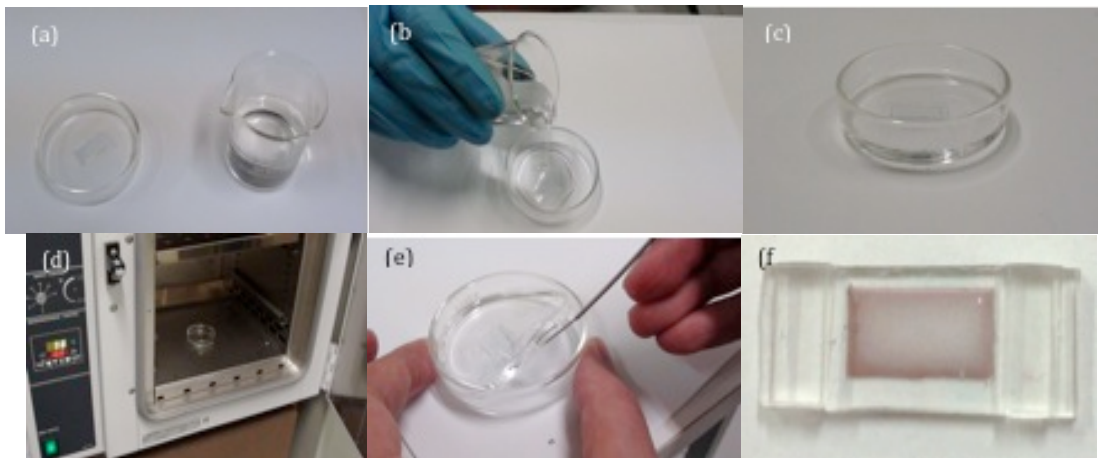


Figure 1. (a) PDMS preparation, (b) Air degassing, (c) Master covering, (d) baking process, (e) peeling off, (f) PDMS template filled with Au nanoparticles.

3. Experimental characterization

The prepared sample has been experimentally characterized by studying its spectroscopic response for different stretching conditions of the PDMS substrate. In order to apply a mechanical strain to the sample, we placed it between two tweezers that could be moved apart by two micrometre mobile actuators. The set-up has been mounted between the light source and the detector of an Agilent 8453E spectro-photometer (Fig. 2a). For each elongation of the sample, the corresponding transmission spectrum has been acquired. Obtained normalized spectra are reported in Fig. 2a. From the graph, it can be observed that an increase of the applied strain corresponds to a red shift of the plasmon resonance wavelength of about $\Delta\lambda=12$ nm (from $\lambda=551$ nm, no applied strain, to $\lambda=563$ nm, 20,4% applied strain). This result confirms the hypothesis made above that, by using a PDMS matrix doped with Au NPs, it is possible to obtain a system showing tunable plasmonic properties. Indeed, Kinnan and Chumanov have also demonstrated that, by changing the inter-distance between NPs, their electromagnetic coupling is correspondingly modified [10]. In their case, a spectroscopic analysis performed on substrates coated with Ag NPs of the same size

but with different surface density also showed a red shift of the plasmon resonance wavelength when the particle density is decreased.

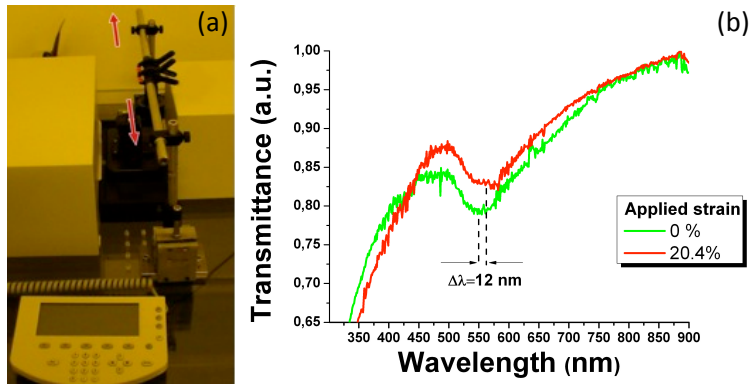


Figure 2. (a) UV-VIS spectro-photometer and stretching setup; (b) wavelength of the plasmon resonances versus the applied strain; the dashed lines indicate the points of minimum of the surface plasmon resonances.

Under an applicative point of view, we can envision several possibilities for the obtained result. By reproducing the system in thin layers ($100\mu\text{m}$) it could be possible to realize very precise pressure control sensors. A more sophisticated employment would instead result in advanced solar applications due to the ability of Au nanoparticles to harvest the electromagnetic radiation [11].

4. Conclusions

In this paper, we have reported on our first attempts to fabricate template structures made of PDMS and comprising Au nanoparticles. A spectroscopic characterization of the obtained samples has shown that it is possible to tune their plasmon resonance wavelength through the application of a mechanical strain. In particular, it has been observed that a red-shift of this resonance wavelength corresponds to a longitudinal elongation of the sample. This behaviour is probably due to an increase of the particle interdistance occurred because of the applied strain. These preliminary results represent, in our opinion, the first steps towards the realization of a new class of plasmonic devices with tunable properties.

References

- [1] V. M. Shalaev, S. Kawata, Nanophotonics with Surface Plasmons (Advances in Nano-Optics and Nano-Photonics). Elsevier, 2007.
- [2] T.W. Ebbesen, C. Genet, S.I. Bozhevolnyi, Phys. Today 2008, 61, 44.
- [3] J.N. Anker, W.P. Hall, O. Lyandres, N.C. Shah, J. Zhao, R.P. Van Duyne, Nat. Mater. 2008, 7, 442.
- [4] L. Childress, J. M Taylor, A. S. Sorenson, M. D. Lukin, Phys. Rev. A 2005, 72, 052330.
- [5] Y. Fainman, L.P. Lee, D. Psaltis, C. Yang, "Optofluidics: fundamental, devices, and application", McGraw-Hill (2010).
- [6] F Merola, M. Paturzo, S. Coppola, V. Vespi and P. Ferraro, "Self-patterning of a polydimethylsiloxane microlens array on functionalized substrates and characterization by digital holography", J. Micromech. Microeng. 19, 125006 (2009).
- [7] J. G. Cuennet, A.E. Vasdekis, L. De Sio and D. Psaltis, "Optofluidic modulator based on peristaltic nematogen microflows", 5, 234 (2011).
- [8] Mata, A.J. Fleischman and S. Roy "Characterization of polydimethylsiloxane (PDMS) properties for biomedical micro/nanosystems", Biomed. Microdev. 7, 4, 281 (2005).
- [9] U. Kreibig and M. Vollmer, "Optical Properties of Metal Clusters", Springer: Berlin, New York (1995).
- [10] Mark K. Kinnan and George Chumanov, "Plasmon coupling in two-dimensional array of silver nanoparticles: II effect of the particle size and interparticle distance", J.Phys. Chem. C 114, 7496 (2010).
- [11] He, Sailing, Cui, Yanxia, Ye, Yuqian, Zhang, Pu, Jin, Yi, "Enhance transmission and harvest light with nano-antennas and metamaterials," Materials Today, 12, 12, 16-24 (2009).